Study of the Rheology of Thin Liquid Films - Novel Flexible Molds for Nanoimprinting

David R. Barbero

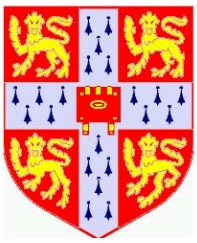

A dissertation submitted in partial fulfilment of the requirements for the degree of Doctor of Philosophy

Darwin College

Cavendish Laboratory

University of Cambridge

September 2009

Declaration

This dissertation is the result of my own work and includes nothing which is the outcome of work done in collaboration, except where specifically indicated in the text. No part of this thesis has been submitted for a degree or other qualification at this or any other University. This dissertation does not exceed the limit of 60,000 words.

Acknowledgements

Coming to Cambridge and working at the Cavendish Laboratory has been a fantastic adventure. During my time in Cambridge, I had the opportunity to interact with many exceptional people who helped me along the path. I would like to thank all of them, and in particuliar my supervisor Professor Steiner for giving me the opportunity to work in his group and for teaching me how to think like a physicist. Other members of the Biological and Soft Systems group, and of the Nanoscience Center have shown a keen interest in my research, and contributed to interesting discussions and ideas. I would like to thank, among others and in no particular order: the whole Steiner group, Dr. Guck, Dr. Blumenfeld, Dr. Andrew, Professor Terentjev, Professor Huck, Professor Sir Sam Edwards, Dr. Chalut, Professor Welland, Dr. Saifullah, William Winter. Special thanks go to Dr. Federle who introduced me to the fascinating world of insects, as well as Dr. Clemente and Jan-Henning Dirk for an enjoyable interdisciplinary collaboration. I extent my thanks to the people outside Cambridge whose help was precious, and in particular Dr. Schäffer for useful comments on parts of my thesis. My appreciation goes to the Department of Physics for awarding me the Abdus Salam runner-up prize in Physics during my PhD. I also would like to thank all the people who contributed to keep me out of the lab when I needed it. I would like to thank especially Jamie Blundell, Rafi Blumenfeld, and all the members of the Cocks and Hens tennis team for the fun I had practicing and playing league matches, and for introducing me to real grass. Thank you all for this! The Cavendish cricket club also gave me the opportunity to discover, and actually enjoy, cricket. Several members of Darwin College also played an important role in keeping me happy and sane during the difficult times. I would like to thank all of them, and especially Paul Franklin for his friendship throughout my PhD, and for making me discover South Africa. Least but not last, my gratitude and love goes to my close ones, Madeleine for always being there and supporting me, my family and especially my parents who helped me the best they could.

Abstract

This thesis is composed of two parts: the first one is devoted to the rheology of thin liquid polymer films, the second one deals with the development of novel flexible stamps for imprinting of micro- and nano-structures. Thin films are ubiquitous, and they are used in a large number of technological applications. An understanding of their properties, and of the factors influencing their stability is therefore important. In particular, the rheological properties of thin liquid films, and the role played by interactions at the solid/liquid interface have been subject to much debate in recent years. In this thesis, a new experimental set-up was built to study the destabilization process of a thin liquid polymer film subject to an electric field. The measurement of the characteristic time of destabilization of thin liquid films of polystyrene on a solid substrate provides a way to measure the viscosity of the liquid layer. I also extended the use of multiple beam interferometry to the measure of thickness fluctuations in the thin film due to an electrohydrodynamic instability only a few microns wide. This method allows the measurement of the growth rate of an instability with sub-nanometer resolution, and gives complementary information about the hydrodynamics of the liquid film. The results of this work lead us to propose a model for the disentanglement of large macromolecules during the formation of the thin film by spin-coating. The low density of entanglements in spin-cast films provides an explanation for the higher mobility observed in thin liquid layers.

The last part of the thesis deals with the development of a new type of flexible organic molds for nanoimprinting. I show that patterning of polymer surfaces can be performed with high resolution ($\sim$10 nm) and at relatively low cost using these new molds. They also solve a number a problems often encountered with conventional inorganic materials which makes them easier to use and better suited to pattern large areas. I finally demonstrate applications of these molds to build a stretchable laser, and to manufacture thin transparent microstructured surfaces to study insect adhesion.

List of published work

The following publications originated from the work presented in this thesis:

1. **Non-Equilibrium Polymer Rheology in Spin-Cast Films**,
   D. R. Barbero and U. Steiner, *Physical Review Letters* **2009**, 102 (24), 248303, Editor's Suggestion. (This paper was also featured as a highlight of the online APS journal *Physics*: Spinning out plastics, **June 2009**.)

2. **A sensitive interferometric method to study the growth of thin film surface instabilities**, D. R. Barbero, P. Andrew and U. Steiner, in preparation **2009**.

3. **High resolution nanoimprinting with a robust and reusable polymer mold**, D. R. Barbero, M. S. M. Saifullah, P.Hoffmann, H. J. Mathieu, D. Anderson, G. A. C. Jones, M. E. Welland, and U. Steiner, *Advanced Functional Materials* **2007**, 17, 2419.

4. **Friction ridges in cockroach climbing pads: anisotropy of shear stress measured on a transparent, microstructured substrates**,
   C. J. Clemente, J-H. Dirks, D. R. Barbero, U. Steiner, W. Federle, *Journal of Comparative Physiology A* **2009**, 195 (9), 805.

5. **Mechanically Tunable Conjugated Polymer Distributed Feedback Lasers**,
   B. Wenger, N. Tétreault, D. R. Barbero, M. E. Welland, U. Steiner, R. H. Friend, in final revision before submission, **2009**.

6. **Easy release fluoropolymer molds for micro- and nano-pattern replication**, D. R. Barbero, P. Hoffmann, H. J. Mathieu, *European Patent* (05005105.1.), **2006**.

7. **Biomimetics of insect adhesion on rough surfaces**,
   W. Federle, U. Steiner, S. Hofmann, D. R. Barbero, *EPSRC grant proposal*, submitted, **2009**.

Contents

Chapter 1

Introduction

This thesis is composed of two distinct parts. The first one deals with the self-assembly of thin liquid polymer films using electric fields, and the study of their rheological properties. The second part is concerned with the micro- and nano-structuring of bulk and thin polymer films by nanoimprint lithography (NIL), and the development of a new type of molds for NIL. Applications of this method are shown in the fields of optoelectronics and biology.

1.1 Motivation

1.1.1 Thin Liquid Films

Thin organic films are ubiquitous. Although we are often unaware of their existence, they constitute an essential part of everyday life. They can be found in a large number of natural environments, as well as in many technological applications. Thin films are often used to change the properties of a surface or to protect it from wear (e.g. paints and lubricants). For most technological applications, it is desired that the film remains stable and covers homogeneously the entire surface of the underlying solid substrate. For instance, a thin layer of

lubricant is used in hard disc drives to reduce the wear between the head and the disc during operation. This thin anti-adhesive film also prevents adhesion of the head to the fast spinning disc during reading and recording of the data, thereby preventing crashing of the head into the disk and the irreversible loss of the recorded information. The wetting properties of thin liquid films on a substrate are also very important in many technologies. For instance, a layer of paint must completely wet the wall or the surface it covers and form a uniform film free of bulges or disturbances. Another example is in the field of ink-jet printing, where the definition of letters and other shapes critically depends on the wetting of small drops of ink only a few microns in diameter which impinge on a sheet of paper at high velocity. The drops should neither bounce, nor splash, and they should stay stable over long periods of time (years) without changing shape (e.g. caused by dewetting). A clear understanding of the physical, chemical and rheological properties which influence of the stability of a thin liquid layer is therefore critical. Another familiar example is the liquid tear film of the eye which protects and nourishes the cornea. This thin layer of lubricant must indeed cover uniformly the whole surface of the eye and it has to stay stable for a short amount of time (roughly the time needed between two blinks of the eye).

However, under certain circumstances films break up (or dewet) to form droplets leaving patches of the underlying surface uncovered, as in the case of water on a hydrophobic surface. The leaves of the Lotus flower provide a well-known example of a super-hydrophobic surface onto which water doesn't spread. In fact, the surface properties of most plants, as well as the skin and fur of most animals, are often designed to prevent the formation of a continuous film of liquid (such as water). While the biological reasons for this behaviour are interesting in themselves, we'll remain concerned with the physical aspect of dewetting which has to do with the role of intermolecular forces between the

liquid film and the underlying substrate, and the rheological properties of the film which control the time scale of dewetting. Control of the physical properties of thin films during processing is therefore of the utmost importance to achieve the desired goal. An understanding of all these parameters is indeed necessary to predict the evolution in time, and the final shape, or morphology, of the thin film.

1.1.2 Micro- and Nano-Patterning of Thin Films

For many industrial applications, thin polymer films are used as a medium to form regular arrays of micro- and nano-structures by lithographic methods. The formation of these patterns usually changes the physical and energetic properties of the film. For example, a water repellent material can be made even more water repellent by the creation of micro-patterns with a well defined geometry on its surface. Anti-reflection coatings can also be produced by structuring a film with sub-micron features. Another application is in the semi-conductors industry, where lithography is routinely used to pattern polymer films with well defined features to create transistors and lines to process and transport information in a computer chip. The thin polymer film is then used as a template to transfer nano-patterns (currently as small as $\sim$35 nm) into the underlying silicon substrate to form a "permanent image" by etching. A final application is in the emerging area of micro- and nano-fluidics where small channels are formed in a polymer film to manipulate tiny amounts of liquids and form chemical reactions for medical tests purposes.

Thin films are characterized by the small ratio of their thickness to their lateral dimensions. Because, they have a relatively large surface area compared to a bulk material, the properties of a thin film are often different from that of

a thicker sample of the same material. Another aspect which is important for understanding the properties of a thin film is the way it has been processed. For industrial purposes, films ∼100-1000 nm thick are usually deposited onto a solid substrate by the process of spin-coating (also called spin-casting). Understanding how the processing of the thin film influences its physical properties is therefore crucial. This can have drastic implications for many applications. As we demonstrate in Chapter 7, a little known aspect of spin-coating is that it can change the rheology of the deposited polymer film, and lead to a kinetically enhanced destabilization of the film under an applied potential.

1.2 Outline of the Thesis

1.2.1 Electrohydrodynamic (EHD) Instabilities

Although dewetting is often unwanted, a striking feature of an unstable thin film is that it often breaks-up into a semi-regular array of beautiful micro- and nano-sized patterns. Besides their aesthetic appeal, instabilities in thin films can also be used to measure interfacial forces. In turn, these forces can be tuned to destabilize a thin film and create structures with various sizes and shapes. When the dewetting of a thin film is controlled with a spatially modulated force such as an electric field, it can be used to form a regular array of well defined patterns. For this reason, electric field driven instabilities have been used as a lithographic tool to form a large number of features with various shapes and sizes [1, 2].

The measurement of surface forces also provides a means to quantify the role played by the friction at the solid/liquid interface. These forces can then be used to extract several important rheological and hydrodynamic properties

of liquids in confinement such as for example the viscosity or the slip length. To do so, we use the method developed by E. Schäffer and U. Steiner to trigger instabilities in thin polymer melt films using electric fields [1]. When subjected to an electric field, dielectric materials respond by creating polarization charges at their surface. Because of the imbalance of charges at the air/liquid interface, the free surface is destabilized and patterns are formed in the polymer melt. The formation of the patterns and their lateral periodicity has been documented and explained [3]. However, the growth rate of these patterns and the influence of the boundary conditions at the solid/liquid interface remain unclear. Experiments have shown discrepancies between calculated values and the experimentally observed growth of these instabilities [4, 5]. The origin of this difference remains unexplained. The hydrodynamics of the film directly influence the time constant at the onset of the instability and the evolution of the patterns with time. Here, we are concerned with the time scale on which these features form.

The aim of the first part of this thesis is therefore to gain insight into the hydrodynamics of a thin liquid layer which is destabilized by an electric field. Chapters 2 and 3 introduce the theory of electrohydrodynamic instabilities (EHD) in thin liquid films. Chapters 4 and 6 deal with the experimental part of the work, and describe techniques used, and the methods developed to prepare and analyze samples. Chapter 5 talks about the measurement of small thickness fluctuations in the films, and Chapter 8 introduces an experimental method to detect the formation of EHD instabilities, and measure their time evolution with sub-nanometer resolution. Measurements of growth rates are also presented. Chapter 7 deals with results concerning the rheology of thin liquid films using electric fields. The results show that the processing conditions of the sample are critical in determining the rheological properties of the films and their chain conformation.

1.2.2 Nanoimprint Lithography

Nanoimprint lithography (NIL) is a powerful tool to create well-defined arrays of micro- and nano-structures in a polymer substrate [6, 7]. Despite its achievements in reproducing sub-10 nm features and a large amount of research in the last 10 years, a number of problems remain which limit the efficiency of NIL. High temperature nanoimprinting of viscous polymers which are glassy at room temperature is usually performed using brittle and expensive molds made of inorganic materials. These molds have mechanical rigidity and a high definition of features, but they are very expensive to produce (especially nanostructures molds), and they are brittle. As a replacement, soft molds made of plastics or elastomers have been used because of their low cost and ease of fabrication. However, the deformation of these polymer molds under pressure remains a major issue which limits their resolution in high temperature nanoimprinting.

Chapter 9 introduces the development a new type of flexible, anti-adhesive and mechanically and chemically resistance plastic molds for imprinting techniques [8]. It is demonstrated that these molds can be used in a wide range of pressures and temperatures to form micro- and nano-patterns with dimensions close to 10 nm by nanoimprint lithography. Applications are shown to build a stretchable laser and to study insect adhesion on transparent surfaces with a well defined roughness.

Chapter 2

Hydrodynamics of Thin Liquid Films

Building on Erik Shäffer's original work [9], we introduce the equations of motion that describe the motion of fluid, and derive the *Navier–Stokes equation* for a thin liquid film geometry. The effect of the boundary conditions (BC) at the solid/liquid interface (slip *vs.* no slip) is examined. From this, the derivation of the equation of motion for both cases (slip and no-slip) is given. Finally, a linear stability analysis is performed to determine the characteristic growth rate and wavevector in the thin film. These equations lay the foundations for all other equations that describe the formation of the electrohydrodynamic instabilities described in this thesis.

2.1 The Equations of Motion for a Fluid

The flow of an infinitesimal volume of liquid $\mathrm{d}V$ in a thin film is determined by two equations: the equation of continuity, and the equation of motion. The first one states that the mass of a volume V of fluid can increase only if there is a net influx of fluid across its bounding surface S (conservation of mass). It is expressed in differential form by the following expression known as the equation

of continuity:

$$\partial_t \rho + \boldsymbol{\nabla} \cdot (\rho \boldsymbol{v}) = 0 \tag{2.1}$$

where ρ is the fluid's density, $\boldsymbol{v}$ its velocity across the surface, and $\partial_t X$ is the time derivative of the variable X [1]. For an incompressible fluid ($\partial_t \rho = 0$), and $\boldsymbol{\nabla} \cdot (\rho \boldsymbol{v}) = 0$.

The second equation necessary for the flow of a fluid through a small volume $\mathrm{d}V$, is the equation of motion which gives the rate of momentum change $\partial_t (\rho \boldsymbol{v})$ across the surface $\mathrm{d}S$ delimiting the volume $\mathrm{d}V$. The equation of motion states that the acceleration of an infinitesimal volume $\mathrm{d}V$ of fluid of mass m is due to the sum of all the forces, or stress tensors, acting on it. These forces are due to pressure gradients, viscosity, gravitation, etc..., and in its most general form the equation of motion is expressed by:

$$\rho \partial_t \boldsymbol{v} = -\rho(\boldsymbol{v} \cdot \boldsymbol{\nabla})\boldsymbol{v} - (\boldsymbol{\nabla} \cdot \boldsymbol{\Pi}) + \rho \boldsymbol{g}. \tag{2.2}$$

This expression equates the rate of momentum change in $\mathrm{d}V$ (left part of the equation) to the sum of the change in momentum due to bulk flow (convective flow $\rho \cdot \boldsymbol{v}(\boldsymbol{v} \cdot \boldsymbol{n})$ through $\mathrm{d}S$ (1st term on the right), the divergence of the momentum stress tensor $\boldsymbol{\Pi}$ (second term on the right side) and the gravitational force due to $\boldsymbol{g}$.

2.1.1 The Stress Tensor

The stress tensor $\boldsymbol{\Pi} = p\boldsymbol{\delta} + \boldsymbol{\tau}$ is the sum of the pressure p within the fluid in thermal equilibrium and the stress tensor $\boldsymbol{\tau}$ is related to the viscosity of the fluid. For an incompressible and Newtonian fluid (viscosity independent of the

[1] $\boldsymbol{\nabla} \cdot \boldsymbol{F}$ is the divergence of the vector $\boldsymbol{F}$, whereas $\boldsymbol{\nabla} G$ is the gradient of the scalar quantity G.

shear rate), the constitutive equation of the stress tensor $\mathbf{\Pi}$ is

$$\mathbf{\Pi} = p\boldsymbol{\delta} - \eta\boldsymbol{\gamma} \tag{2.3}$$

where p is the hydrostatic pressure, η is the shear viscosity and $\boldsymbol{\gamma}$ is the shear rate.

2.1.2 The Equation of Motion for a Newtonian Fluid

The general form of the equation of motion for an incompressible and Newtonian fluid is the *Navier–Stokes equation*:

$$\rho\left(\partial_t \boldsymbol{v}\right) = -\rho(\boldsymbol{v}\cdot\boldsymbol{\nabla})\boldsymbol{v} - \boldsymbol{\nabla}p + \eta\Delta\boldsymbol{v} + \rho\boldsymbol{g}. \tag{2.4}$$

In the case of Newtonian polymeric liquid films, a number of approximations can be made which reduce the *Navier–Stokes equation* to a simpler form. First, the flow of the thin polymer film (at least in the early stages of destabilization) is very slow and can be considered in a quasi-steady state ($\partial_t = 0$). Moreover, we can make the assumption that the velocities are very small due to the large viscosity of the polymer melts that we use. For thin films, we can also safely neglect the effect of gravity, as will be demonstrated later in this chapter. Equation 2.4 therefore reduces to

$$\boldsymbol{\nabla}p = \eta\Delta\boldsymbol{v}. \tag{2.5}$$

Due to the geometry of the problem, we consider a two-dimensional film with the flow of liquid in the x direction and the velocity gradient which varies only

along the z axis. This gives along the x and z coordinates:

$$x : (\partial_x p) = \eta \partial_{zz} \upsilon.$$
$$z : \partial_z p = 0. \tag{2.6}$$

Since the pressure is constant within the depth of the film (along z), the pressure gradient is a function of x only and this means that the pressure gradient $(\partial_x p)$ along x is a constant. We can therefore find the velocity profile in the film by integrating twice with respect to z:

$$\upsilon = \frac{1}{2\eta}(\partial_x p)z^2 + c_1 z + c_2. \tag{2.7}$$

The constants c_1 and c_2 depend on the boundary conditions at the free surface, and at the solid/liquid interface respectively. For a no-slip boundary condition, the velocity vanishes at the substrate ($z = 0$), whereas if we include slip the fluid has a finite velocity ($\upsilon \neq 0$) at this interface. At the free liquid–air surface ($z = h$), there are no stresses ($\sigma_{xz} = \eta \cdot \partial_z \upsilon = 0$).

2.2 Influence of Slip at the Substrate

2.2.1 The Slip and No-Slip Conditions

The way a liquid flow interacts with atoms or molecules at the interface with a solid wall is a complex phenomenon which is currently the subject of much research in the field of thin polymer films and in microfluidics. In his "Lectures on Physics", Feynman writes that the frictional drag exerted on an object moving slowly through a viscous liquid is proportional to its velocity υ [10]. However, if the motion through the liquid is fast enough, the drag force varies approximately

with the square of the velocity v: $F_d \sim kv^2$, where k is the friction coefficient. If the velocity continues to increase, then this relation is no longer valid. This example shows that friction at the interface between two materials is a complex phenomenon and that the laws used to describe it are only approximations which break down when the conditions are changed. The friction of two materials in contact is the result of several processes that can interact or couple resulting in a non-trivial behaviour. One common assumption in fluid dynamics is that the velocity of a liquid at a solid interface reduces to zero: this is the so-called no-slip boundary condition (NSBC). This assumption is mainly based on macroscopic observations, but in recent years detailed experiments and simulations of fluid flow at the microscopic scale have revealed that slip (or non-zero velocity) can occur at the interface between a solid wall and a liquid flow [11–16]. There are also situations where a NSBC cannot be expected and leads to a stress singularity at a moving contact line, like in the case of a liquid spreading on a solid surface [16, 17]. The break-down of the continuum (macroscopic) approach to slip reveals the complex interaction of molecules and atoms at small length scales. Many factors can contribute to slip: the strength of the interatomic bonds between a solid and a fluid, the surface roughness and the flow rate have been identified as being the main ones. A clear understanding of the detailed interaction of all these parameters is therefore necessary, and highly sensitive experimental methods need to be applied to decouple the effect of inhomogeneities at the atomic length scale. A better understanding of the flow properties of liquids into micro- and nano-channels is also necessary for many technological applications (e.g. microfluidics) as well as for medicine. As an example, the flow of blood in arteries is commonly modeled using Poiseuille's equation for laminar flow with a NSBC. However, the inclusion of a slip BC can lead to a 30% change in flow rates in arteries [18]. In the remainder of this

chapter, we will mainly be concerned with the flow of a liquid (either simple or complex) on a solid surface.

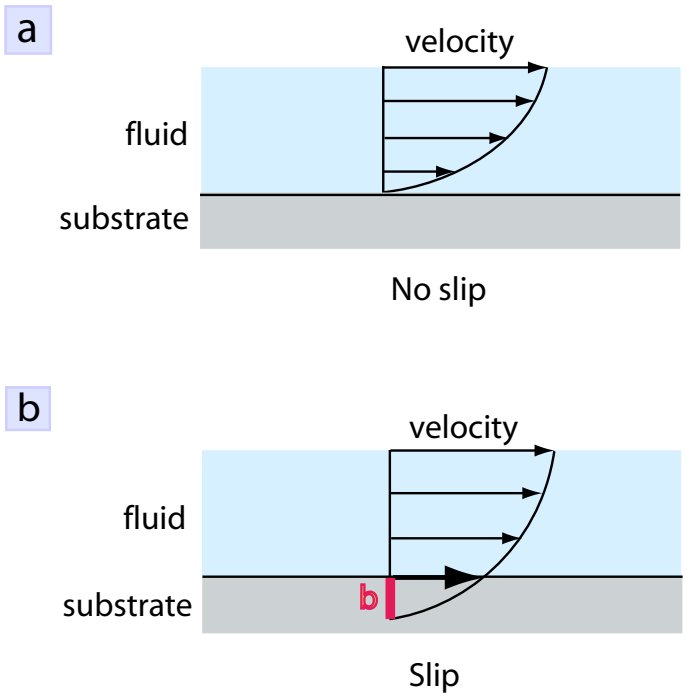

Figure 2.1: Slip vs. no slip at the interface between a fluid and a solid substrate. In the no slip case (a), the velocity of the fluid is zero at the interface with the substrate. The slip boundary condition (b), however, introduces a finite velocity at the substrate. The velocity profile reduces to zero inside the substrate at a depth b (also called the "slip length").

Solid/Fluid Interactions

The strength of the interaction between the solid substrate and the liquid is an important factor in determining slip. It has long been assumed that slip can only occur on non-wetting surfaces, and that the degree of slip depends on the equilibrium contact angle between the solid and the liquid [19,20]. Large contact angles are often assumed to be a necessary condition for slip, whereas liquids which have a strong affinity for the solid will result in a NSBC. However, this view has been strongly revised in recent years with reports that slip can also

occur when the interaction between the solid and the liquid is attractive [21]. Experiments have shown that slip can even occur on a completely wetting system (Newtonian sucrose solutions on silicon wafers) [22]. Clearly, although weak liquid/wall interactions often results in larger slip lengths, the measurement of macroscopic contact angles alone is not a good indicator of slip. A study by Cho *et al.* reported that contact angle measurements can be related to slip only for non-polar n-alkane liquids [23].

Shear Rate

Because the flow of a liquid on a solid is an hydrodynamic process, the shear rate produced by the flowing liquid at the solid interface needs to be taken into consideration as well. If the force exerted by the flow is stronger than the interaction of the liquid molecules with the solid wall, then interfacial slip can be expected [24]. Both experiments and simulations seem to agree that slip is a shear rate dependant process. The NSBC seem to apply at low shear rates [25], whereas slip kicks off above a critical shear rate which depends on the interactions of the solid with the liquid [26]. However, at high shear rates other complications occur, such as shear thinning which causes the formation of a boundary layer of lower viscosity and results in apparent slip [13]. True slip at the molecular scale may be zero at the interface but a sharp increase in the velocity field away from the interface gives the appearance that slip occurs at this interface (see Fig. 2.2). In this picture, slip actually occurs at a liquid/liquid layer close to the solid interface.

Surface Roughness

Another important parameter which determines slip is surface roughness. Here again, the details of the system under investigation will influence the effect

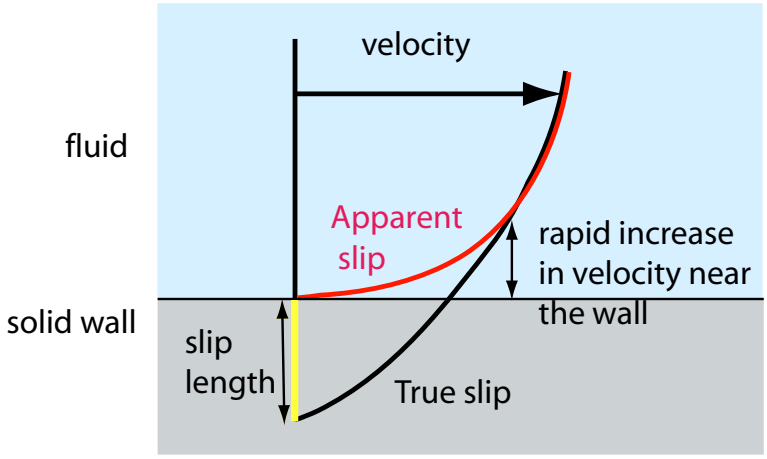

Figure 2.2: True slip vs. apparent slip (shear thinning) at the interface between a fluid and a solid substrate (wall). In the true slip case, the velocity of the fluid is finite and non zero at the solid wall. On the other hand, apparent slip gives the impression that slip occurs at the solid wall whereas the velocity at the solid/liquid interface is in fact zero. Apparent slip may occur when there is shear thinning of the fluid near the wall.

that roughness has on slip. It is commonly thought that roughness will inhibit slip because the corrugations at the wall slow down the liquid flow by viscous dissipation of its energy and result in a NSBC [27]. It was indeed experimentally demonstrated that a RMS roughness as small as 6 nm can suppress slip of both polar and non-polar simple Newtonian liquids on a poorly wetted surface [14,28]. The same system produced slip when the solid was atomically smooth. Slip was also strongly reduced on surfaces that were partially (inhomogeneously) covered by a SAM layer, and which resulted in an increase in roughness [21]. However, a slight increase in RMS roughness (from 0.7 nm to 12.2 nm) was also shown to enhance slip significantly in a completely wetting system [22]. For non-wetting systems, large slip was also measured when the substrate was patterned with grooves [29]. Simulations have also showed that nanometer patterning of the solid wall suppresses slip when the liquid is wetting, but strongly increases slip in the non-wetting case due to the creation of a composite air/solid interface which reduces the friction between the fluid and the wall [30]. Other works seem to indicate a more complex dependence of slip on the roughness of the wall: the NSBC is valid only when the size of the wall corrugations is similar to that of the liquid molecules [31]. In this case, the molecules are trapped inside the wall roughness, and slip is not observed. When the wall roughness is either increased or decreased, slip may occur.

Substrate Deformation

The mechanical deformation of the solid interface also plays a critical role. A surface onto which chains have been chemically attached will interact differently with a flowing liquid of polymer chains than a surface with no thetered chains. Depending on the shear rate different regimes were predicted by Brochart and de Gennes [32], and experimentally observed by Leger and co-workers using Near

Field Laser Velocimetry (NFLV) [33]. For shear rates below a critical value J_c, the chains are spheroidal of size R_0 and the viscous friction at the surface is large. In this case, slip is strongly suppressed. If the shear rate is increased, a regime is reached where the chains undergo a coil stretch transition and elongate to a constant length L_c. This regime is called the marginal state and occurs when the velocity of the melt is greater than a critical velocity v_c. In this case, the slip length increases linearly with the shear rate. Finally, for even higher shear rates, a third state is reached where the chains disentangle and are strongly elongated to a length $L > L_c$. In this regime, strong slip occurs, which is independent of the shear rate. It was also demonstrated that in polymer melts the degree of slip is proportional to the length of the chains [34]. It is important to note that slip can also occur at the interface between a SAM and the solid substrate. The degree of slip in this case depends on the rigidity and strength of the bonds between the film (which can be considered visccoelastic) and the wall (which is elastic) [24].

Nanobubbles

A final point concerns the existance of nanobubbles at the interface between the liquid and the wall. AFM studies have shown the existence of such bubbles on both hydrophobic and hydrophilic surfaces [35, 36], and some authors have suggested that they may increase slip and flow rates. de Gennes derived an expression for the slip length in presence of a gas film at the solid/liquid interface [37], and found that large slip of several microns can occur. While the presence of these bubbles still remain somewhat mysterious, recent reports seem to indicate that they may result from outgassing of gas that was dissolved in the liquid and which preferentially nucleates at the solid interface [36].

2.3 Flux in the Film

2.3.1 The No-Slip Case

For the no-slip case, the parabolic velocity profile becomes

$$v = \frac{1}{2\eta}(\partial_x p)(z - 2h)z \tag{2.8}$$

and the mean velocity in the film

$$\begin{aligned} \bar{v} &= \frac{1}{h}\int_0^h v \; dz \\ &= \frac{h^2}{3\eta}(-\partial_x p). \end{aligned} \tag{2.9}$$

For our 2-dimensional case, the flux along the x axis is $j = h \cdot \bar{v}$, and using the expression of the mean velocity derived in Eq. 2.9, we obtain the equation for the flux going through a plane perpendicular to $x - z$:

$$j = \frac{h^3}{3\eta}(-\partial_x p). \tag{2.10}$$

2.3.2 The Slip Case

If we consider that the fluid has a non-zero velocity (v_s) at the solid/liquid interface, we expect that the flow of liquid in the film will be faster than in the no-slip case. The finite velocity of fluid at the substrate is determined from the shear stress induced by the fluid motion at the solid/liquid interface. The stress at the solid surface $\sigma_s = k \cdot v_s$ must be equal to the viscous shear stress produced

by the liquid at this interface:

$$\sigma_{\mathrm{s}} = k \cdot \upsilon_{\mathrm{s}} = \eta \cdot |\partial_z \upsilon(z)|_{z=0} \tag{2.11}$$

where k is a friction coefficient that depends on the properties of the solid substrate and the interactions between the solid and the liquid. The velocity at the substrate, or the slip velocity, becomes

$$\begin{aligned} \upsilon_s &= \frac{\eta}{k} \cdot |\partial_z \upsilon(z)|_{z=0} \\ &= b \cdot |\partial_z \upsilon(z)|_{z=0} \,. \end{aligned} \tag{2.12}$$

The slip length b is the length at which the velocity extrapolates to zero in the direction perpendicular to the solid wall. Depending on the interactions between the fluid and the solid, the slip length can either be positive (weak solid/liquid interactions), or negative (stronger solid/liquid interactions).

Solving Eq. 2.7 for c_1 and c_2 gives the velocity profile in the film in the presence of slip:

$$\upsilon = \frac{1}{\eta}(\partial_x p)(\frac{z^2}{\eta} - (z-b)h) \tag{2.13}$$

and the mean velocity $\bar{\upsilon}_s$ in the film is

$$\bar{\upsilon}_s = \frac{h(h+3b)}{3\eta}(-\partial_x p). \tag{2.14}$$

Multiplying $\bar{\upsilon}_s$ by h gives the flux of fluid in a film with interfacial slip at the substrate:

$$j_s = \frac{h^2(h+3b)}{3\eta}(-\partial_x p). \tag{2.15}$$

2.3.3 Equation of Motion for a Thin Film

To derive the equation of motion for the flow of liquid through the thickness h of the film, we write that the rate of increase of thickness h in the film is simply due to an influx of liquid (j) in the x direction.

$$\partial_t h = \partial_x j. \tag{2.16}$$

This expression relates the fluid motion due to the pressure gradient in the film to a change in thickness h of the film.

In the no-slip case, inserting Eq. 2.10 into Eq. 2.16 we find:

$$\partial_t h = \partial_x [\frac{h^3}{3\eta}(-\partial_x p)]. \tag{2.17}$$

In the slip case, the equation of motion becomes:

$$\partial_t h = \partial_x [\frac{h^2(h+3b)}{3\eta}(-\partial_x p)]. \tag{2.18}$$

2.3.4 Contributions to the Pressure in the Film

Electrostatic Contribution and Surface Tension

In equations 2.10 and 2.15, the pressure term p that is exerted on the surface of the film is the sum of all pressures contributing to the motion of the fluid. The stronger effect is due to the electrostatic pressure p_{elect} produced by the large electric field applied between the two electrodes to deform the surface of the film. The electric field couples with the capillary surface fluctuations caused by the thermal motion of molecules to give an electrohydrodynamic (EHD) instability. The growth of these instabilities is opposed by the restoring Laplace pressure p_L, which is the second largest contribution to the pressure term of Eq. 2.10. This is

due to the fact that interfaces between two immiscible liquids or between a liquid and the air are mobile and can be deformed to minimize their energy. Stable liquids have smooth surfaces and the fluctuation of their thickness due to thermal motion is usually on the order of a few Ångströms. Due to the stabilizing effect of the surface tension γ the free surface is like a stretched membrane opposing any fluctuations.

In thin-films, surface fluctuations are dampened by the surface tension through the restoring effect of the Laplace pressure. The Laplace pressure is directly proportional to the surface tension and the curvature of the liquid/air interface $(1/R)$, and therefore varies with x. It expresses the difference in pressure across a curved interface, and in two dimensions (one curvature) it is expressed by:

$$p_L = \frac{\gamma}{R}. \tag{2.19}$$

The curvature of the interface can also be written as a function of x since it is the second derivative of the thickness profile: $1/R = -\partial_{xx}h$. The Laplace pressure now becomes

$$p_L = -\gamma \partial_{xx} h. \tag{2.20}$$

van der Waals Forces and Other Contributions

In our experiments the two main contributions to the EHD instability are the electrostatic pressure and the Laplace pressure. Other minor contributions to the pressure are due to van der Waals interactions (p_{vdW}), acoustic fluctuations (p_{ac}), temperature gradients across the film (p_T), gravity and atmospheric pressure. This list is, however, by no means extensive and other effects may contribute to p in specific circumstances. In the context of the experiments presented here, we can already eliminate the effects of gravity since we deal with films much

thinner ($\sim 100\,\mathrm{nm}$) than the capillary length (C_p). C_p is defined as the length at which the hydrostatic pressure ($\rho \cdot g \cdot C_p$) equals the Laplace pressure ($\frac{\gamma}{C_p}$):

$$C_p = (\frac{\gamma}{\rho g})^{(\frac{1}{2})}. \tag{2.21}$$

Temperature gradients across the film are also negligible as will be shown in the experimental section, and p_T can be neglected as well. Although they do not contribute significantly to the growth of the EHD instability, van der Waals interactions are still one main driving force for the dewetting of very thin liquid films in the absence of electric fields. van der Waals forces, also called dispersion forces, are due to electron density fluctuations which exist at any moment in molecules and atoms and which lead to the creation of an "instantaneous" dipole [38]. The field generated by this dipole induces dipolar moments in adjacent molecules and creates an attractive force between them. The energy of interaction of van der Waals forces varies as ($-d^{-6}$) for a short separation distance d between close by atoms. If this distance becomes greater than $\sim 10\,\mathrm{nm}$, there is a slight delay in the response of the polarized atom which weakens the energy of interaction because of the time taken by the electric field to travel the distance between them. During this short time the original dipole, which fluctuates continuously, may have shifted its orientation and the interaction now varies in $-d^{-7}$. This type of interaction is called "retarded" and is effective on distances up to $\sim 100\,\mathrm{nm}$. The strength of the van der Waals forces depends on the polarizability of the molecules, and they can be either attractive or repulsive depending on the materials in contact at the interface. This property is reflected in the sign of the Hamaker constant A used in the calculation of the van der Waals force. The microscopic energy between two molecules separated by a distance d (with $d \leq 100\,\mathrm{nm}$) varies as $-d^{-6}$. For two

planar surfaces, the non- retarded interaction gives an energy per unit area equal to [38]:

$$W(d) = -\frac{A}{12\pi d^2}. \tag{2.22}$$

Therefore the sum of all the contributions to the pressure which are responsible for the deformation of the liquid surface:

$$p(x,h) = p_L + p_{elect} + p_T + p_{ac} + p_0 + \cdots \tag{2.23}$$

can be approximated in the EHD experiments to:

$$p(x,h) \simeq p_L + p_{elect} \tag{2.24}$$

where p_0 is the contribution of terms which are independent of x and h, like for instance atmospheric pressure. The other terms depend on either x, h or both variables.

2.4 Linear Stability Analysis

By analyzing the effect of a small perturbation applied to the surface of the liquid film, one can determine the conditions for the stability of the film. In the following, a linear stability analysis of the equation of motion allows us to determine the maximum growth rate for an initially small sinusoidal surface instability triggered by an external electric field. We first derive Eq. 2.18, where $\partial_{xx}h$, $\partial_{xxx}h$ and $\partial_{xxxx}h$ are respectively the second, third and fourth derivatives of h with respect x:

$$\partial_t h \;=\; \frac{(2b+h)h}{\eta}(\partial_x h)\left[\partial_x p\right] + \frac{(3b+h)h^2}{3\eta}\left[\partial_{xx} p\right]. \tag{2.25}$$

Next we replace p by the expression of the surface pressure in the film (Eq. 2.24):

$$\begin{aligned}\partial_t h &= \frac{2bh}{\eta}(\partial_x h)\left[(\partial_h p_{elect})(\partial_x h) - \gamma(\partial_{xxx} h)\right] \\ &+ \frac{h^2}{\eta}\left[-b\gamma(\partial_{xxxx} h) + (\partial_h p_{elect} + b\partial_{hh} p_{elect})(\partial_x h)^2\right] \\ &+ \frac{h^2}{\eta}\left[b(\partial_h p_{elect})(\partial_{xx} h) - \gamma(\partial_{xxx} h)(\partial_x h)\right] \\ &+ \frac{h^3}{3\eta}\left[-\gamma(\partial_{xxxx} h) + (\partial_{hh} p_{elect})(\partial_x h)^2 + (\partial_h p_{elect})(\partial_{xx} h)\right]. \quad (2.26)\end{aligned}$$

Because the perturbation of the film's surface is weak at the early stages ($t \sim 0$) of the instability, we approximate the variation of the surface profile with a sinusoidally time varying function:

$$h(x,t) = h_o + \zeta e^{iqx + \frac{t}{\tau}}. \quad (2.27)$$

The initial thickness of the film is h_o, and the sinusoidal lateral thickness variation at t=0 is given by the term ζe^{iqx}, where ζ is the amplitude of the surface fluctuation due to capillary waves.

2.4.1 Linear Part of the Equation of Motion

In deriving Eq. 2.26 with expression 2.27 for h, we express the linear part of the equation of motion by keeping only the terms which are linear in ζ: all higher order terms are negligible since $\zeta \ll h_o$. Therefore the linear equation of motion including a slip b becomes:

$$\partial_t h_{lin} = \frac{h_o^2(h_o + 3b)}{3\eta}\left[-\gamma(\partial_{xxxx} h) + (\partial_h p_{elect})(\partial_{xx} h)\right] + O(\zeta^2). \quad (2.28)$$

2.4.2 Nonlinear Part of the Equation of Motion

The non-linear part of the equation of motion, which includes all non-linear terms, is:

$$\begin{aligned}\partial_t h_{non-lin} &= \frac{2bh_o}{\eta}(\partial_x h)\left[(\partial_h p_{elect})(\partial_x h) - \gamma(\partial_{xxx} h)\right] \\ &+ \frac{h_o^2}{\eta}\left[(\partial_h p_{elect} + b\partial_{hh} p_{elect})(\partial_x h)^2 - \gamma(\partial_{xxx} h)(\partial_x h)\right] \\ &+ \frac{h_o^3}{3\eta}\left[(\partial_{hh} p_{elect})(\partial_x h)^2\right]. \end{aligned} \tag{2.29}$$

For a fluctuation satisfying $\Delta h \ll h_o$, non-linear terms do not contribute significantly to the growth rate of the instability, and the equation of motion can be approximated to Eq. 2.31.

2.4.3 The Dispersion Relation

The next step is to solve Eq. 2.31 with the expression of $h(x,t)$ taken from Eq. 2.27, and divide both sides by $\zeta e^{iqx+\frac{t}{\tau}}$. This leads to the linear *dispersion relation* for a film destabilized by an electric field:

$$\frac{1}{\tau} = -\frac{h_0^2(h_o + 3b)}{3\eta}\left[\gamma q^4 + \partial_h p_{elect} q^2\right]. \tag{2.30}$$

Similarly, the can derive the equation of motion and the linear dispersion relation for a film without slip at the solid wall by taking $b = 0$:

$$\partial_t h = \frac{h_o^3}{3\eta}\left[-\gamma(\partial_{xxxx} h) + (\partial_h p_{elect})(\partial_{xx} h)\right] + O(\zeta^2). \tag{2.31}$$

The dispersion relation without slip reads:

$$\frac{1}{\tau} = -\frac{h_o^3}{3\eta}\left[\gamma q^4 + \partial_h p_{elect} q^2\right]. \tag{2.32}$$

Equations 2.30 and 2.32 give the growth rate $1/\tau$ of an instability of wavevector $q = 2\pi/\lambda$ that develops in a film of initial thickness h_o. It expresses the growth rate of the emergent instability when the external electrostatic pressure overcomes the stabilizing Laplace pressure. Since γ is always positive, the sign of τ depends on the sign of the gradient of the excess surface pressure ($\partial_h p_{elect}$) with respect to the film thickness h. This is also the second derivative of the potential energy of interaction $\Delta\phi = \partial_{hh}\phi$ for the system considered. When plotted as a function of q as shown in Fig. 2.3[2] ($\Delta\phi = \partial_h p_{elect} < 0$), the *dispersion relation* predicts:

- the growth rate is negative for large q, and therefore damping (instead of growth) of surface instabilities occur.
- in the limit of very small q (large wavelengths) the growth rate vanishes.
- the growth rate has a maximum for a characteristic wavevector q_{max}.

The maximum growth rate determines the selection of the characteristic wavevector that grows the fastest at the surface the film, other wavevectors grow more slowly and therefore are not observable. If the potential gradient is ≥ 0, the time constant $\tau < 0$ for all q, and the film remains stable since all wavevectors are damped.

[2]For practical purposes, we plot the scaled growth rate $1/\tau^* = \tau_o/\tau(q)$ where τ_o is a scalar quantity which corresponds to the wavector q_o.

2.4.4 Characteristic Wavevector

Solving Eq. 2.30 gives q_{max} which corresponds to the maximum growth rate $(1/\tau_{max})$:

$$q_{max}^2 = -\frac{\partial_h p_{elect}}{2\gamma}. \tag{2.33}$$

For a given surface tension γ, the characteristic wavevector q_{max} is entirely determined by $\partial_h p_{elect}$. Therefore by varying the strength of the electrostatic pressure, one can select the value of q_{max} (see Fig. 2.4) . For larger electrostatic pressures, the Laplace pressure can be overcome more easily and smaller instabilities can be formed. It is also noteworthy to realize that changing the solid/liquid boundary conditions by including slip does not change the value of q_{max}. As will be shown in subsequent chapters, the lateral dimensions that can be achieved within technologically accessible times in polymer thin films with the EHD instability typically range from $\sim$10 μm down to $\sim$10 nm.

It is important to note that the wavevector q_{max} of a surface instability is determined entirely by the balance of forces at the liquid/air interface (the term in brackets in Eq. 2.32). The hydrodynamics of the film do not come into consideration in the selection of the characteristic wavelength. This can be easily seen from Fig. 2.5 which shows the dispersion relation for the case of the no slip BC at the solid/liquid interface (solid line), and for the case of the slip BC (dashed line). On the other hand, the time constant τ, or characteristic time for destabilization, is directly proportional to the shear viscosity of the film η, and inversely proportional to the surface tension γ. This means that, in addition to its strong dependance on the pressure gradient, the time for destabilization is also influenced by the rheology of the film. This aspect will be discussed in more detail in the next chapters.

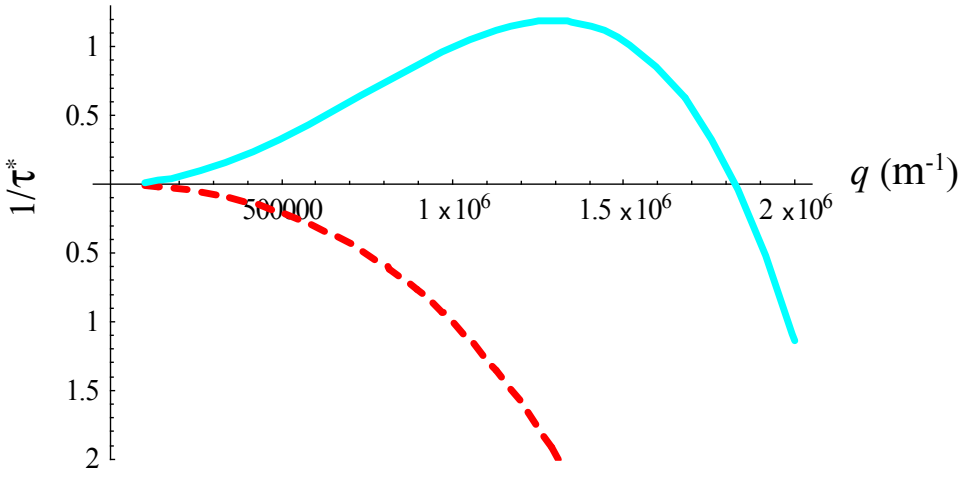

Figure 2.3: Dispersion relation derived by a linear stability analysis of a thin film. The reduced growth rate $1/\tau^*$ is negative for all wavevectors q in the case of a positive potential $\partial_h p_{elect}$ (dashed line). However, $1/\tau^*$ has a positive maximum for a wavevector q_{max} when the potential $\partial_h p_{elect}$ is negative, or destabilizing, (solid line).

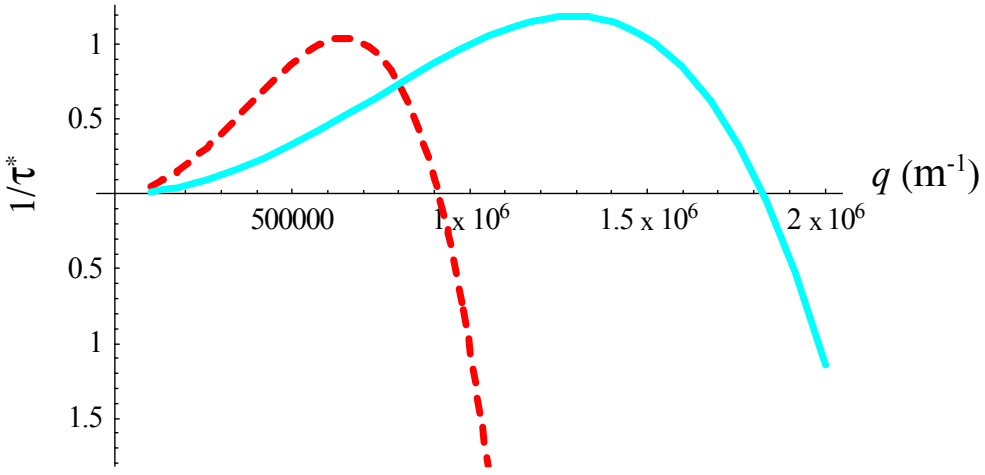

Figure 2.4: Dispersion relation in the case of a negative potential $\partial_h p_{elect}$. The dashed line corresponds to a smaller potential (weaker electric field), whereas the solid line represents a stronger potential. The maximum wavevector q_{max} is shifted to higher values when the applied potential is stronger.

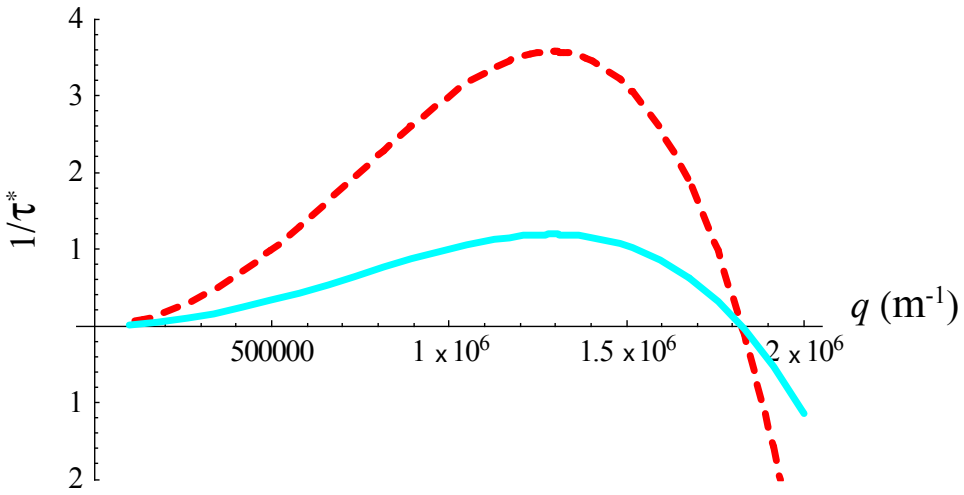

Figure 2.5: Dispersion relation for a negative potential $\partial_h p_{elect}$, and for two different boundary conditions at the solid/liquid interface. The solid line corresponds to the case where no slip is present. When slip is introduced into the dispersion relation (Eq. 2.30), the growth rate is increased (dashed line) and is maximum at the same wavevector q_{max} as in the no slip case.

Chapter 3

Thin Film Stability and Electrohydrodynamics

3.1 Thin Film Stability

The stability of a film depends on its free energy. The variation of the free energy of a film as a function of its thickness is represented in Figure 3.1. Starting with a film of initial thickness h_0 two common cases can be distinguished:

- in (a) the film is stable and a change in the film thickness is not favoured, since moving away from point A means increasing the energy of the film.

- in example (b) the film can lower its energy by changing its thickness, and it is therefore unstable. The final metastable state is the coexistence of two films of thicknesses h' and h''. This case happens when the second derivative of the free energy $\partial_{hh}\Phi(h) < 0$, i.e. h is within the unstable region defined by the dashed lines. This is often referred to as *spinodal dewetting*, in analogy to the spinodal decomposition of binary mixtures due to concentration fluctuations [39].

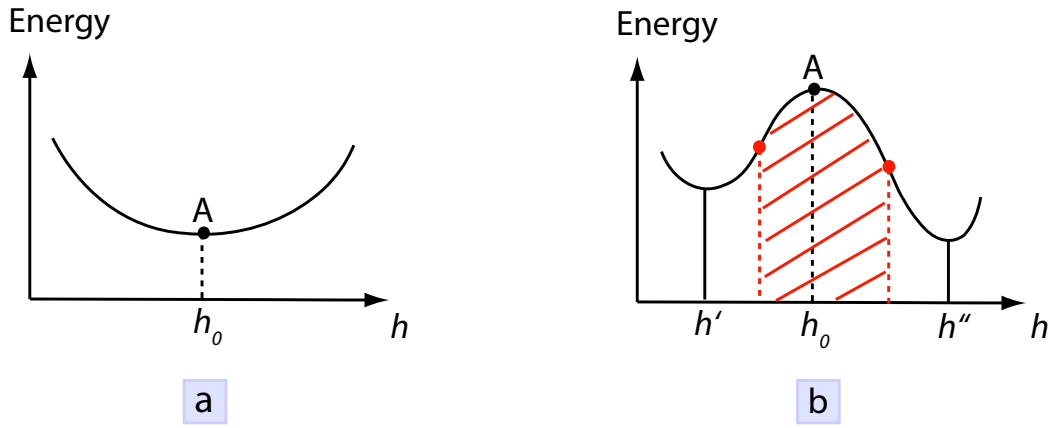

Figure 3.1: Diagram representing the stability of a thin film as a function of its thickness. (a) The film of initial thickness h_0 is stable. (b) The film is unstable and can reduce its energy by breaking into two films of thicknesses h' and h''. The shaded region represents the *spinodal* domain where $\partial_{hh}\Phi(h) < 0$.

Thin films can therefore be destabilized and change their thickness depending on the forces acting on them. For instance, films which are not stabilized by gravity (*e.g.* films thinner than the capillary length) may be subject to dewetting caused by weak intermolecular (van der Waals) forces [40].

We saw in the previous chapter that the *dispersion relation* for a film destabilized by an electric field is:

$$\frac{1}{\tau} = -\frac{h_o^2(h_o + 3b)}{3\eta}\left[\gamma q^4 + \partial_h p_{\text{elect}} q^2\right]. \tag{3.1}$$

More generally, the excess surface pressure p_{elect} can be written in terms of the surface potential Φ (free energy per surface area) which represents all the different contributions to the pressure $p(x, h)$. The term $\partial_h p_{\text{elect}}$ in Eq. 3.1 can therefore be replaced by the Laplacian of the potential $\Delta\Phi$, and a more general

expression for the *dispersion relation* becomes:

$$\frac{1}{\tau} = -\frac{h_o^2(h_o + 3b)}{3\eta}\left[\gamma q^4 + \Delta\Phi q^2\right]. \tag{3.2}$$

3.1.1 Dewetting Due to van der Waals Forces

If no electric potential is present, the thin film may still be destabilized if the pressure gradient overcomes the stabilizing effect of the surface tension γ. The most ubiquitous contribution to Φ is due to van der Waals forces. These intermolecular forces are composed of three contributions, which depend on permanent dipolar moments in nearby atoms. One contribution, due to dispersion (London) forces between two neutral atoms, is always present. The additional potential Φ_{vdW} depends on the film thickness h, and its gradient with respect to h is the disjoining pressure p_{vdW}. It is called disjoining pressure [38] because it is the pressure that needs to be imposed on a film to prevent it from thickening. In the opposite case, if the film can reduce its energy by thinning (leading to dewetting), p_{vdW} is called the conjoining pressure because it is the pressure needed to prevent thinning and to keep the two interfaces of the film at a distance equal to its original thickness h_0. In this case, the excess surface pressure is composed of a term due to van der Waals interactions and the Laplace pressure p_{L}:

$$p(x, h) = p_{\mathrm{L}} + p_{\mathrm{vdW}}. \tag{3.3}$$

The strength of the van der Waals forces depends on the polarizability of the molecules which are in contact in the vicinity of the substrate/film interface, and they can be either attractive or repulsive depending on the sign of the Hamaker constant A. The microscopic energy between two molecules separated by a distance d (with $d < 100\,\mathrm{nm}$) varies as d^{-6}. For a thin-film of thickness h, the

non- retarded interaction gives an energy per unit area, or interfacial potential Φ_{vdW}, equal to [38]:

$$\Phi_{\mathrm{vdW}} = -\frac{A}{(12\pi h^2)} \tag{3.4}$$

In the case of a thin liquid film on a solid surface, A is proportional to the difference of polarizability between the solid, α_{s}, and the liquid, α_{l}:

$$A \propto \pi^2 \alpha_{\mathrm{l}} (\alpha_{\mathrm{s}} - \alpha_{\mathrm{l}}) \tag{3.5}$$

The Hamaker constant is usually on the order of 5–50 kT at room temperature. Depending on the sign of A, two cases are possible.

- If $A < 0$, the potential in equation 3.4 is positive and its value increases for smaller values of the thickness h. In order to decrease its free energy the system can therefore increase the film thickness, thereby leading to a situation where the film remains stable on top of the substrate (Fig. 3.1 a).
- In the opposite case ($A > 0$), the free energy of the film can be reduced by decreasing h. The film is therefore in a metastable state and dewets (Fig. 3.1 b).

3.1.2 Spinodal vs. Nucleated Dewetting

The process of dewetting can be either heterogeneous due to nucleation, or spinodal due to van der Waals forces. Nucleated dewetting happens when the film is metastable and the second derivative of the free energy $\partial_{hh}\Phi(h)$ is positive. It is a random process which does not show any type of spatial correlation or periodicity. Nucleation provides a way for the film to overcome the energy barrier that prevents it from reaching a more stable state. Two types of nucleations can occur:

- 1) nucleation due to small particles or dust present in the film;

- 2) thermally activated nucleation when the height of the film is close to the sign reversal of $\partial_{hh}\Phi(h)$. Spinodal dewetting, on the other hand, is a spontaneous process which happens only if $\partial_{hh}\Phi(h)$ is negative and which is characterized by an instability developing uniformly on the sample with a characteristic wavelength λ.

In the case of a thin polystyrene film deposited onto a substrate and which is not subject to any applied external field, the stability of the film can be determined by the sign of the Hamaker constant for the system *(substrate/film/air)* or *(1/3/2)*:

$$A_{132} = (\sqrt{A_{11}} - \sqrt{A_{33}}) \cdot (\sqrt{A_{22}} - \sqrt{A_{33}}) \tag{3.6}$$

When the Hamaker constant of the film (intermediate medium 3) has a value between those of the surrounding media 1 and 2, then $A_{132} < 0$ and the film is stable. We can draw an analogy with the spreading coefficient of the liquid 3 on top of the substrate 1, which also depends on the polarizabilities of the two media. It is positive when the substrate is more polarizable than the liquid, therefore leading to wetting of the film on the substrate. In this case the van der Waals force is repulsive and disjoins the layers 1 and 2 by increasing the thickness of the film, thereby reducing the free energy of the system.

3.1.3 Effect of an Intermediate Layer on Dewetting of a Film

For the *Si/PS/air* system, $A_{132} \sim -6 \cdot 10^{-20}\,\mathrm{J}$, which means that a PS layer is stable on top of a silicon substrate. Experimentally, however, silicon is typically covered by a thin native oxide layer ($\sim$1–2 nm) which can change the sign of the

Hamaker constant of the system $Si/SiO_x/PS/air$ leading to spinodal dewetting of polystyrene [41, 42]. The potential energy (i.e. the free energy per surface area) of the PS film on top on a silicon oxide layer due to the van der Waals interactions can be written by adding the contributions of each layer to the overall energy [41, 43]:

$$\Phi'_{vdW} = -\frac{A_{\mathrm{SiO}}}{12\pi h^2} + \frac{A_{\mathrm{SiO}} - A_{\mathrm{Si}}}{12\pi(h + h_{\mathrm{SiO}})^2} \tag{3.7}$$

where h and h_{SiO} represent the thickness of the PS film and of the oxide layer respectively. Although van der Waals forces are not exactly additive, this approach allows the calculation of interaction energies for stratified systems. The stability of a PS film on silicon can be predicted from the interface potential (free energy) of the system when the thickness of the oxide layer is varied. It was shown experimentally that polystyrene films spin-cast on a Si substrate covered by a native oxide layer only dewet spinodally ($\partial_{hh}\Phi'_{\mathrm{vdW}} < 0$) if they are thinner than about 4.1 nm [41]. Thicker films may dewet due to heterogeneous nucleation. Thicker oxide layers however can change the sign of the Hamaker constant from negative to positive, and lead to spontaneous dewetting even for relatively thick non-polar polymer films.

3.2 Electrohydrodynamic Instabilities

Wavelike fluctuations that form on the surface of a liquid film upon application of an external electric field are called *electrohydrodynamic* (EHD) instabilities. The excess pressure of the electric field destabilizes the liquid surface and leads to the formation of surface waves with a characteristic lateral periodicity or wavelength. In this section we first briefly review some of the earlier studies of

EHD instabilities in liquids. In the remainder of the section, we then focus on instabilities produced in a thin polymer film with unpatterned electrodes and we determine the characteristic wavelength associated with these instabilities.

3.2.1 Introduction

Instabilities produced at the surface of a liquid by electrification have stimulated the interest of scientists for more than a century. Some of the earlier experiments performed by Swan [44] showed the formation of figures in a resin maintained between two electrodes. The complexity of the patterns formed could be varied by changing the size and shape of the electrodes. In the 1930s, a theoretical model was proposed to explain the deformation of a fluid interface under a perpendicular electric field [45]. Later, Melcher and coworkers studied in detail the destabilization of fluids under an externally applied electric field, and the influence of the accumulation of free charges at the liquid/air interface in poorly conducting liquids [46,47]. More recently, EHD instabilities have generated a strong interest in the scientific community with the almost simultaneous discovery by Schaeffer *et al.* [48] and by Chou *et al.* [49, 50] that the regular patterns created by these instabilities could be used for lithographic purposes in thin polymer films. Since then, several experimental studies as well as theoretical simulations of EHD instabilities in thin polymer films have been performed [51–56]. Two fundamentally different cases should be distinguished: in the first case, the thin film is "sandwiched" between two unpatterned, smooth electrodes, whereas in the second case one of the electrodes is patterned. The latter case gives rise to instabilities which have the same lateral dimensions and spacing as that of the patterned electrode, and it can be used to create regular arrays of fine features for lithographic purposes. However, when the electrodes are unpatterned, a char-

acteristic wavelength develops in the film whose dimensions depend on the field strength, film thickness, surface tension and dielectric contrast at the destabilized interface [48, 57]. Although the formation of instabilities with unpatterned masks has a limited interest for lithographic purposes, it is scientifically more interesting since the periodicity of the patterns directly reflect the balance of forces at the liquid/air interface. The characteristic wavelength λ_m of the instability gives an accurate measure of the electrostatic potential and can be used to probe the forces acting on the interface. In the remaining of this thesis we will apply the theory of EHD instabilities to perfectly insulating polymer films.

3.2.2 Characteristic Wavelength and Electrostatic Pressure

Although the surface of a liquid at rest may look static to the naked eye, it is in fact in constant motion due to the Brownian agitation of its molecules which give rise to a spectrum of capillary waves at the surface of the liquid polymer. At the early stages of the destabilization process, these capillary fluctuations couple with the applied field and create an instability with a characteristic wavelength λ_m. The wavelength is determined by the force balance between the electrostatic pressure p_{elect} and the Laplace pressure p_L at the liquid/air interface. Therefore, for a liquid film of dielectric constant ϵ and surface tension γ, λ_m is determined by controlling the strength of the applied electric field. If the field is increased, λ_m becomes smaller because there is more electrostatic energy available to deform the interface and smaller capillary fluctuations are then favored. In the case of a perfectly insulating liquid film, polarization charges at the surfaces of the film arise from the dielectric contrast at the liquid/air interface (or more generally liquid/fluid interface), which is responsible for the destabilization of

the interface. The method used here consists of destabilizing a non-conducting thin liquid polymer film "sandwiched" between two conductive electrodes across which a potential difference is applied (Fig. 3.2) [48].

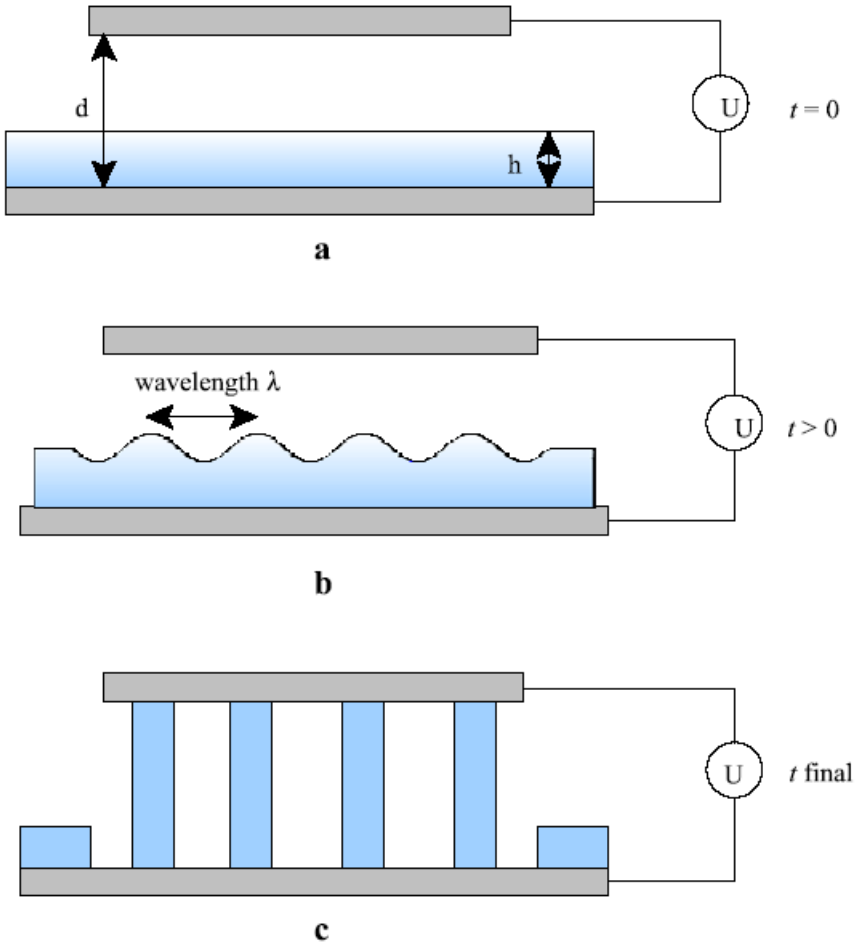

Figure 3.2: (a) A thin polymer film is sandwiched between two conducting plates. There is an applied voltage difference U between the two electrodes, d is the electrode spacing and h is the film thickness. (b) After some time t, instabilities with a characteristic wavelength λ start to form at the surface of the film. (c) After a given time t_{final}, the initially small instabilities have grown into full columns of height d.

Electrostatic Pressure

If a small enough spacing can be obtained between the two electrodes, a strong electric field ($\sim 10^7$ V/m) is generated inside the capacitor inducing an instability with μm-sized wavelengths at the surface of the film. For high electric fields, the influence of all forces except the electrostatic pressure and the Laplace pressure are orders of magnitude weaker and can be considered negligible. The expression for the electrostatic pressure exerted on the free surface of the liquid by an electric field of magnitude E_p in the polymer film was originally derived by Landau and Lifshitz [58]. It follows from the derivation of the free energy contained in the capacitor, and ignores tangential fields. It is expressed as:

$$p_\mathrm{elect} = -\frac{1}{2}\epsilon_0\epsilon_\mathrm{p}(\epsilon_\mathrm{p}-1)E_\mathrm{p}^2 \tag{3.8}$$

where ϵ_0 and ϵ_p are the permittivities of free space and of the polymer respectively.

Characteristic Wavelength

From equation 3.8, we can derive the characteristic wavelength λ_m which develops in the film by solving the *dispersion relation* (Eq. 3.1):

$$\begin{aligned}\lambda_\mathrm{m} &= 2\pi\sqrt{\frac{2\gamma[\epsilon_\mathrm{p}d-(\epsilon_\mathrm{p}-1)h]^3}{\epsilon_0\epsilon_\mathrm{p}(\epsilon_\mathrm{p}-1)^2U^2}} \\ &= 2\pi\sqrt{\frac{2\gamma U}{\epsilon_0\epsilon_\mathrm{p}(\epsilon_\mathrm{p}-1)^2}}E_\mathrm{p}^{-\frac{3}{2}}\end{aligned} \tag{3.9}$$

with d the plate spacing, γ and ε_p the surface tension and dielectric constant of the polymer, respectively, and ε_0 the vacuum permittivity.

3.2.3 Characteristic Time Constant

From the *dispersion relation* (Eq. 3.2) we can express the growth rate of the fastest growing mode q_{m} in a film of thickness h_0 as:

$$\frac{1}{\tau_{\mathrm{m}}} = \frac{\gamma h_0^2 (h_0 + 3b)}{3\eta} q_{\mathrm{m}}^4 \tag{3.10}$$

or as a function of the excess gradient of pressure in the film $\partial_h p_{\mathrm{elect}}$:

$$\frac{1}{\tau_{\mathrm{m}}} = \frac{h_0^2 (h_0 + 3b)}{12\eta\gamma} \partial_h p_{\mathrm{elect}}^2. \tag{3.11}$$

The characteristic time that corresponds to the formation of an instability of wavevector q_{m} is:

$$\begin{aligned} \tau_{\mathrm{m}} &= \frac{3\eta}{\gamma h_0^2 (h_0 + 3b) q_{\mathrm{m}}^4} \\ &= \frac{3\eta}{\gamma h_0^2 (h_0 + 3b)} \left(\frac{\lambda_{\mathrm{m}}}{2\pi} \right)^4 . \end{aligned} \tag{3.12}$$

From these relations we see that the time dependance of the EHD instability varies strongly with the thickness of the film and the pressure gradient, and to a lesser extent with the viscosity and the surface tension. In the remainder of this thesis we'll use λ instead of λ_{m}, and τ instead of τ_{m}, to designate the characteristic wavelength, and time, of an instability. Of particular importance is the variation of τ as a function of the characteristic wavelength λ because we have experimental access to these two variables with our electro-optic set-up as will be explained in the next chapters.

3.2.4 Energetic Considerations in a Capacitor

The capacitor shown in Fig. 3.2 initially consists of a thin dielectric polymer film and an air layer sandwiched between two conducting plates of surface area A_0. This configuration is equivalent to a capacitor in series with a capacitance C_p for the polymer film and C_air for the air layer. The total capacitance is given by:

$$\begin{aligned} \frac{1}{C} &= \frac{1}{C_\mathrm{p}} + \frac{1}{C_\mathrm{air}} \\ &= \frac{h}{\epsilon_0 \epsilon_\mathrm{p} A_0} + \frac{d-h}{\epsilon_0 \epsilon_\mathrm{air} A_0} \\ &= \frac{\epsilon_\mathrm{p} d - (\epsilon_\mathrm{p} - 1)h}{\epsilon_0 \epsilon_\mathrm{p} A_0}. \end{aligned} \tag{3.13}$$

Electric Field in the Film

The electric field induced in the thin film by the applied field can be written in terms of the applied potential difference U and the dielectric properties of the layers inside the capacitor. The total applied voltage U is the sum of the voltages across each layer: $U = E_\mathrm{p} h + E_\mathrm{air}(d-h)$. By rewriting the electric fields generated in the film, E_p, and in the air layer, E_air, as a function of the dielectric displacement $D = \epsilon_0 \epsilon_\mathrm{p} E_\mathrm{p} = \epsilon_0 \epsilon_\mathrm{air} E_\mathrm{air}$, one obtains:

$$\begin{aligned} U &= \frac{D}{\epsilon_0} \left(\frac{h}{\epsilon_\mathrm{p}} + \frac{d-h}{\epsilon_\mathrm{air}} \right) \\ &= \epsilon_\mathrm{p} E_\mathrm{p} \left(\frac{h}{\epsilon_\mathrm{p}} + \frac{d-h}{\epsilon_\mathrm{air}} \right). \end{aligned} \tag{3.14}$$

The electric field in the film is now expressed by (taking $\epsilon_\mathrm{air} = 1$):

$$E_\mathrm{p} = \frac{U}{\epsilon_\mathrm{p} d - (\epsilon_\mathrm{p} - 1)h}. \tag{3.15}$$

We see that the electric field E_{p} is proportional to the capacitance C, and that increasing the capacitance also increases the field in the film.

Free Energy

At constant temperature and density, the free energy of the dielectric film can be expressed by [58]:

$$F = F_0 - \frac{1}{2}\int \boldsymbol{E}_{\mathrm{ext}} \cdot \boldsymbol{P}\, dV \tag{3.16}$$

where $\boldsymbol{P}$ is the dipole moment of the dielectric, F_0 the free energy of the dielectric without any applied field, and $\boldsymbol{E}_{\mathrm{ext}}$ is the field which would be present in the capacitor without any dielectric. If a linear relationship holds between $\boldsymbol{D}$ and $\boldsymbol{E}_{\mathrm{p}}$, then the dipole moment is also linear with respect to $\boldsymbol{E}_{\mathrm{p}}$: $\boldsymbol{P} = k\boldsymbol{E}_{\mathrm{p}}$, where k is the dielectric susceptibility $(\epsilon_{\mathrm{p}} - 1)/4\pi$.

In the parallel plate capacitor configuration, the relationship between a uniform external field E_{ext} and the field in the dielectric film E_{p} is found by writing $U = E_{\mathrm{ext}}d$ and replacing this expression in Eq. 3.15. The free energy in Eq. 3.16 is now expressed by:

$$\begin{aligned} F &= F_0 - \frac{1}{2}\int k\boldsymbol{E}_{\mathrm{ext}} \cdot \boldsymbol{E}_{\mathrm{p}} dV \\ &= F_0 - \frac{1}{2}\left(\frac{\epsilon_{\mathrm{p}} - 1}{4\pi}\right)\int \boldsymbol{E}_{\mathrm{ext}} \cdot \boldsymbol{E}_{\mathrm{p}} dV \\ &= F_0 - \frac{1}{2}\left(\frac{\epsilon_{\mathrm{p}} - 1}{4\pi}\right)\left(\frac{d}{\epsilon_{\mathrm{p}} d - (\epsilon_{\mathrm{p}} - 1)h}\right)\int \boldsymbol{E}_{\mathrm{ext}} \cdot \boldsymbol{E}_{\mathrm{ext}} dV. \end{aligned} \tag{3.17}$$

The last step in Eq. 3.17 is obtained by realizing that the fields $\boldsymbol{E}_{\mathrm{ext}}$ and $\boldsymbol{E}_{\mathrm{p}}$ are parallel to each other. If the field is uniform, we obtain the expression of the free energy in a dielectric of volume V in the presence of an external electric

field:

$$F = F_0 - (\frac{\epsilon_\mathrm{p} - 1}{8\pi})(\frac{d}{\epsilon_\mathrm{p} d - (\epsilon_\mathrm{p} - 1)h})\boldsymbol{E}_\mathrm{ext}^2 V \tag{3.18}$$

or similarly, the free energy per unit volume Γ:

$$\begin{aligned}\Gamma &= \Gamma_0 - (\frac{\epsilon_\mathrm{p} - 1}{8\pi})(\frac{d}{\epsilon_\mathrm{p} d - (\epsilon_\mathrm{p} - 1)h})\boldsymbol{E}_\mathrm{ext}^2 \\ &= \Gamma_0 - (\frac{\epsilon_\mathrm{p} - 1}{8\pi})(\frac{\epsilon_\mathrm{p} d - (\epsilon_\mathrm{p} - 1)h}{d})\boldsymbol{E}_\mathrm{ext}^2\end{aligned} \tag{3.19}$$

where Γ_0 is the free energy per unit volume of the dielectric in the absence of the external field.

From this last expression, we see that the free energy of a dielectric is decreased in the presence of an electric field. If the thin film can change shape, it will move in the direction of increasing E_p to reduce its energy further. This is indeed what we observe experimentally: the initially horizontal liquid thin film (Fig. 3.3a) is destabilized and form liquid columns which move towards the opposite charged conductor, and eventually bridge the gap d between the two plates of the capacitor (Fig. 3.3b). The final distance between the columns is the period λ_m that was chosen at the onset of the instability formation.

Change in the Capacitance During Formation of the Instabilities

The formation of the columns can also be understood in terms of a change in capacitance of the dielectric/air system. Since we impose a constant voltage on the plates of the capacitor, the only way for the system to decrease its free energy is to increase its capacitance C. There are several ways to do that. The first one is to reduce the air gap $(d-h)$ inside the capacitor. The attractive force between the two oppositely charged plates would tend to do just this, however

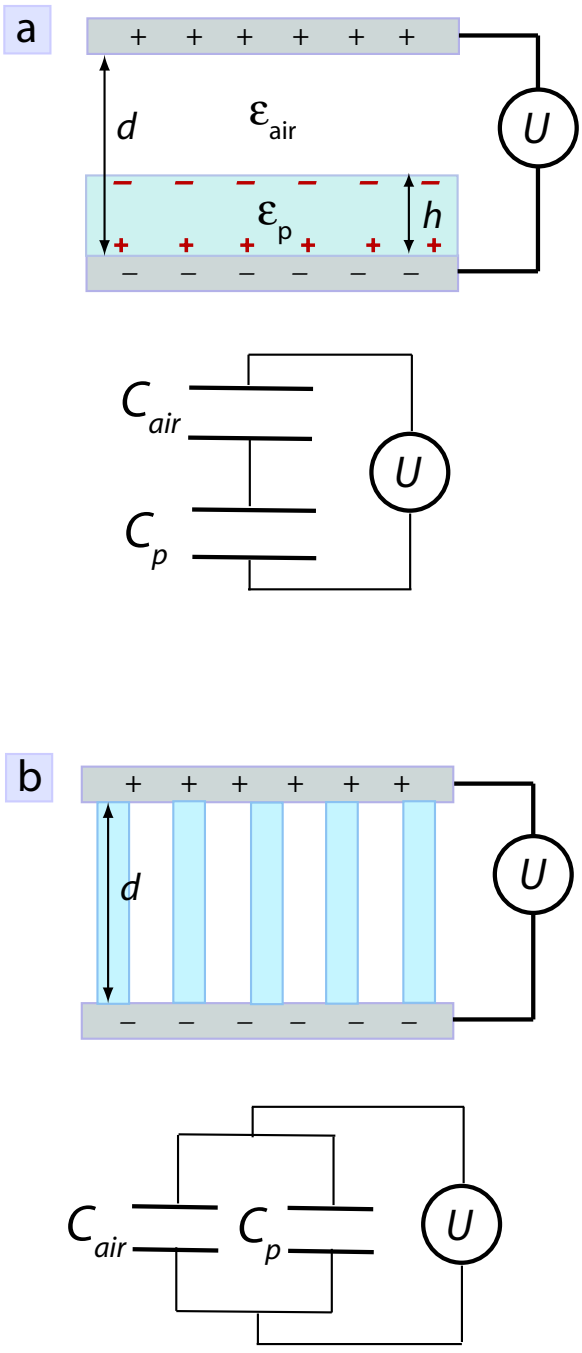

Figure 3.3: (a) Initial configuration of the thin film and the intermediate (air) layer, leading to capacitances in serie. The polarization charges induced in the dielectric layer drive the destabilization of the free interface and eventually will form columns as shown in b. (b) Fully grown columns spanning the gap between the two electrodes. The capacitance is now representative of a parallel configuration.

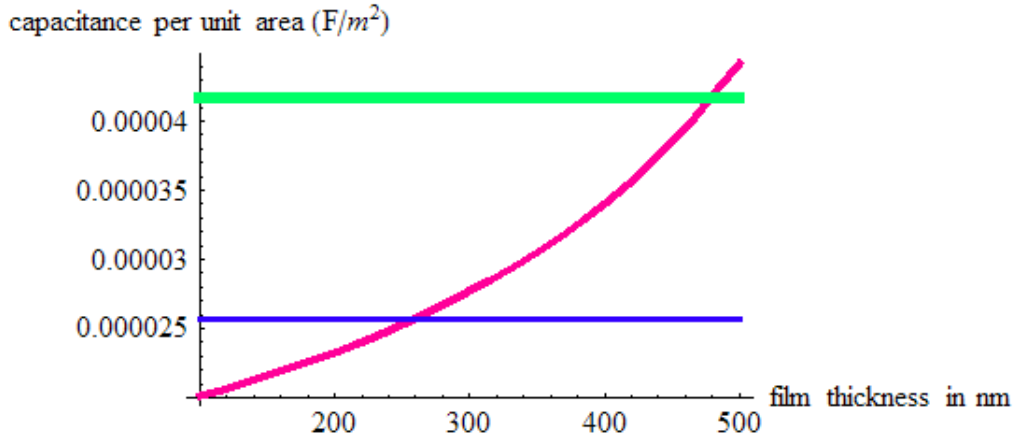

Figure 3.4: Calculation of the capacitance of the dielectric/air system for three different cases. The total capacitor gap is 500 nm and the initial film thickness is 100 nm. The blue (thinner) horizontal line represents the capacitance with fully grown columns covering 30% in surface area. The thicker green horizontal line represents the case where 90% of the surface area is covered by columns. The remaining curve shows the increase in capacitance with the dielectric film thickness for a horizontal (series) film configuration.

practically the distance d is fixed so the plates cannot move toward each other. The other way for the capacitor to increase its capacitance is by changing the configuration of the liquid dielectric from a thin horizontal film to an array of columns which completely fill the gap d. The expression for the capacitance of the columnar dielectric/air system is:

$$\begin{aligned} C &= C_p + C_{air} \\ &= \frac{\epsilon_0 \epsilon_{\mathrm{p}} A_{\mathrm{p}}}{d} + \frac{\epsilon_0 \epsilon_{\mathrm{air}} A_{\mathrm{air}}}{d} \\ &= \frac{\epsilon_0}{d}(\epsilon_{\mathrm{p}} A_{\mathrm{p}} + \epsilon_{\mathrm{air}} A_{\mathrm{air}}) \end{aligned} \tag{3.20}$$

where A_{p} and A_{air} are the surface areas occupied by the dielectric and by the air respectively.

Figure 3.4 shows the variation of the capacitance C for a fixed distance $d = 500\,\mathrm{nm}$ as a function of the initial liquid film thickness h. For a thicker film, the capacitance is higher (curve in Fig. 3.4). However, the capacitance can be further increased if the film changes its configuration from horizontal (Fig. 3.3a) to vertical (columns, see Fig. 3.3b). Starting from a film of 100 nm in Fig. 3.4, the system increases its capacitance by forming columns (thin horizontal line) which span the gap between the electrodes. If the surface area covered by the columns of dielectric, A_p, is larger, the capacitance is further increased (thick horizontal line in Fig. 3.4). This corresponds to the case of an initially thicker horizontal film, or to a smaller gap between the electrodes.

Chapter 4

Techniques and Instrumentation

This chapter introduces a number of experimental methods that have been used during the course of this work. Some of the more specific methods that I used (e.g. multiple beam interferometry, or electric field induced instabilities) are not dealt with here, since they are introduced in detail in other chapters.

4.1 Imaging and Scattering Methods

4.1.1 Electron Microscopy

The Rayleigh criterion indicates that the maximal resolution achievable for an electromagnetic radiation of wavelength λ is $\sim 0.61\,\lambda$ [59]. In the best case, for a $\sim 400\,\text{nm}$ blue-violet light, the smallest distance that can be resolved is therefore $\sim 244\,\text{nm}$ (assuming a perfect system of lenses). Decreasing the wavelength of the electromagnetic wave can be achieved by using high energy beams, like for example an electron beam.

This is the basic idea upon which electron microscopy instruments rely on, such as scanning electron microscopes (SEM) and transmission electron microscopes (TEM). Although both techniques use electron beams to provide a much

increased resolution compared to optical imaging with light, their working principle and the type of information obtained by each microscope is different. In this thesis, we are concerned exclusively with SEM, and therefore TEM will be omitted from the remaining of this section.

SEM

When a focused electron beam enters the surface of a specimen, it interacts in several ways with it. The depth of penetration depends mainly on the energy of the primary electrons and the density of the material which is being analysed. The interaction of the electron beam with the sample produces quasi-elastic (e.g. backscattered electrons) and inelastic events (Auger and secondary electrons, X-Rays). The SEM can be used in different operating modes, which depend on the type of electrons that are being detected. The most common mode of operation is based on the detection of the secondary electrons (SE) which are ejected from the surface of the sample by inelastic scattering of the primary beam. Because of their low energy ($<$50 eV), secondary electrons are emitted only from the top few nanometers of the surface, and they therefore render excellent definition of the topography of the sample.

Inelastically scattered electrons are detected by a SE detector which measures the number of electrons emitted by a portion of the sample that is scanned by the electron beam. The electrons emitted from each subsequent volume of the sample during scanning are attracted to a scintillator-photomultiplier by a small voltage bias, and the electron count is translated into an intensity level. This results in a greyscale image which is readily interpretable by the human brain (see Fig. 4.1). The more SE electrons detected, the brighter the image. Density variations in a sample can also be assessed qualitatively by detecting backscattered electrons (BE). The lateral resolution of the SEM is

on the order of a few nanometers depending on the energy and spot size of the e-beam, the quality of the vacuum, and the sample to detector distance. Typical acceleration voltages are from ∼1 kV to ∼30 kV. High voltages provide better contrast and resolution but sometimes low voltages (1 kV to 5 kV) are advantageous to faithfully image the very top surface of a sample or to delineate fine nanostructures. Insulating samples (like polymers) can also be scanned at a low voltage without prior coating with a conducting material because charging effects are minimized.

ESEM

Another method which is often used to image non-conducting samples without any modification is environmental scanning electron microscopy (ESEM). The ESEM is a modified SEM which can work at higher pressures (up to ∼20 Torr) thanks to a differential pumping system which divides the vacuum system of the ESEM into zones of different pressures. A low pressure is maintained in the electron gun chamber (10^{-7} Torr), whereas a higher pressure is set in the observation chamber where a gas (e.g water vapor) can be introduced. This allows observation of wet and/or biological samples which require a moist atmosphere. Another advantage of the ESEM is that insulating materials (e.g. polymers) can be observed even without having to deposit a conductive layer onto their surface. This is made possible because some of the gas molecules introduced in the chamber become ionized by the SE electrons, thereby preventing negative charge build-up on the surface of the sample. An example of a picture taken with an ESEM is shown in Fig. 4.1 b.

In samples made of materials with different atomic numbers or which contain different phases, compositional contrast can be obtained in the backscattering mode. Backscattered electrons (BE) originate from quasi-elastic scattering of the

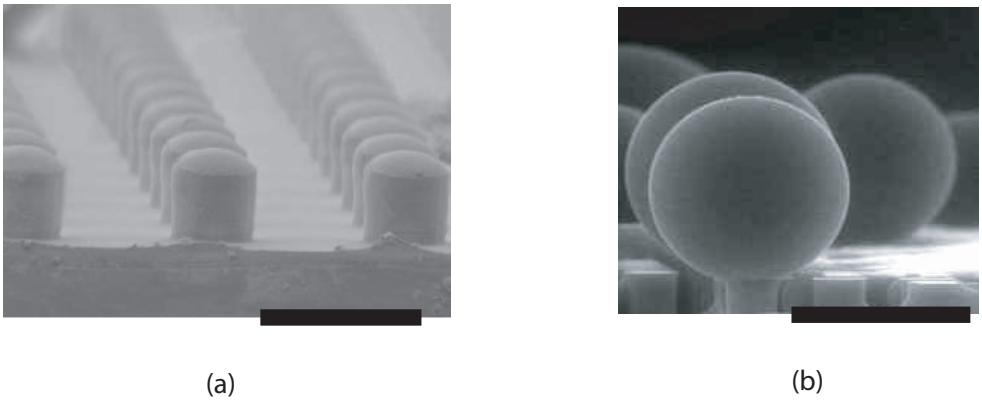

Figure 4.1: (a) Picture of micron-size structures imagined by SEM, and (b) formation of a micro-drop of water on top of microstructured pillars in an ESEM (right). Scale bars are 20 μm.

primary e-beam with the atoms of the sample. Typically, more electrons bounce back when colliding with heavier atoms than with lighter ones. These BE electrons are captured by a semi-conductor detector placed just below the lens and which counts the number of electron-hole pairs created. Often times, the detector is split into different parts which collect electrons at different backscattering angles. Depending on the position of the detector, the backscattered electrons give details of either the composition of the sample, or of the topography. Images obtained in backscattered mode can therefore better represent variations in composition than images taken with SE detectors only. the side collect electrons scattered as a

One drawback of electron beam techniques however is that the measure of the vertical height is not very accurate. For this reason, scanning probe techniques which use a stylus (scanning profilometer) or a cantilever tip (scanning tunneling microscope, atomic force microscope) are better suited to give detailed topographical information of the surface of a sample.

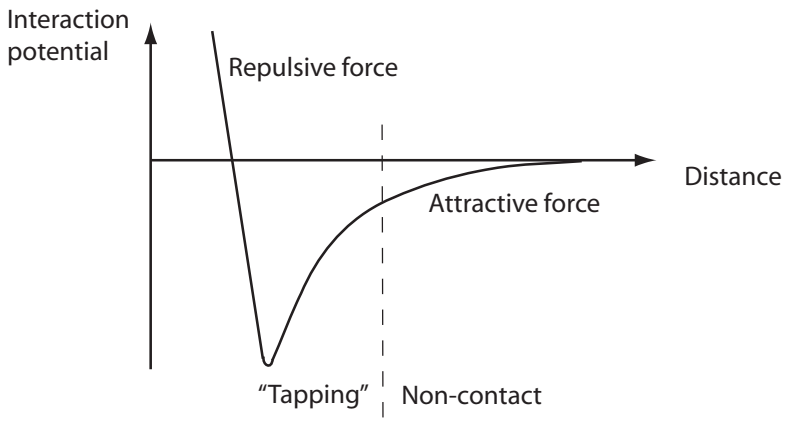

Figure 4.2: Interaction potential as a function of the distance between atoms, showing the attractive and repulsive forces sensed by the AFM tip during a scan.

4.1.2 Atomic Force Microscopy

The Atomic Force Microscope (AFM) allows a lateral resolution of ~ 30 Åand a vertical resolution of less than 1 Åenabling topographic imaging on an atomic scale [60]. The AFM was developed to provide the equivalent of the scanning tunneling microscope (STM) for non-conducting samples. The principle of the AFM relies on the measurement of the force needed to deform a cantilever which is scanned across the sample surface. During scanning, a sharp tip which protudes from one end of the cantilever probes the surface and "senses" forces from the underlying atoms. The main forces acting between the tip and the substrate are due to attractive van der Waals forces, capillary forces, Coulomb electrostatic forces and steric repulsion at very short distances (Fig. 4.2).

When brought in proximity to the surface ($\sim$10–20 nm) the cantilever, which effectively acts as a sensor, is elastically deflected by these forces. This deflection is commonly measured by a laser diode detector or by an optical interferometer and can be used to determine the force of the interaction between the tip and the substrate. Several methods can be used to measure this force. In the first

method, the displacement of the tip normal to the surface is measured and used to calculate the force using Hooke's law, $F = -k \cdot z$, where k is the spring constant of the cantilever and z its displacement. Another way to determine the force F is by measuring the change in the resonance frequency ω_0 (Eq. 4.1) of an oscillating cantilever driven at ω_0. The resonance frequency of the cantilever is given by:

$$\omega_0 = \frac{1}{2\pi}(\frac{k}{m})^{\frac{1}{2}} \tag{4.1}$$

where ω_0 is the resonance frequency of the cantilever, k is the spring constant and m is the effective mass of the tip. When a force deflects the beam, it effectively stiffens or softens the beam, and results in a shift in ω_0 to higher (repulsive force) or lower (attractive force) frequencies according to:

$$\omega_0' = c\sqrt{k - \partial_z F} \tag{4.2}$$

where $\partial_z F$ is the force gradient (second derivative of the interaction potential). The force gradient effectively stiffens or softens the cantilever by changing its spring constant. Because the AFM needs to be able to measure intermolecular forces which are in some cases in the nN range, external sources of noise must be eliminated. This is achieved by oscillating the cantilever at high frequencies ($\sim 100 - 500\,\mathrm{kHz}$) during a scan in order to filter out low frequency components from the environment. To achieve high resonant frequencies, the ratio k/m must be kept large (Eq. 4.1). Typical k values are 1–20 N/m, which means that a force of 1–20 nN is needed to deflect the tip by 1 nm. The mass m is on the order of 10^{-10} kg, which gives resonance frequencies of $\sim 100\,\mathrm{kHz}$. The force resolution achieved is better than 1 nN. AFM cantilevers are often made from silicon or silicon nitride by conventional clean room photolithography and etching techniques, which makes it possible to manufacture sharp tips with relatively high

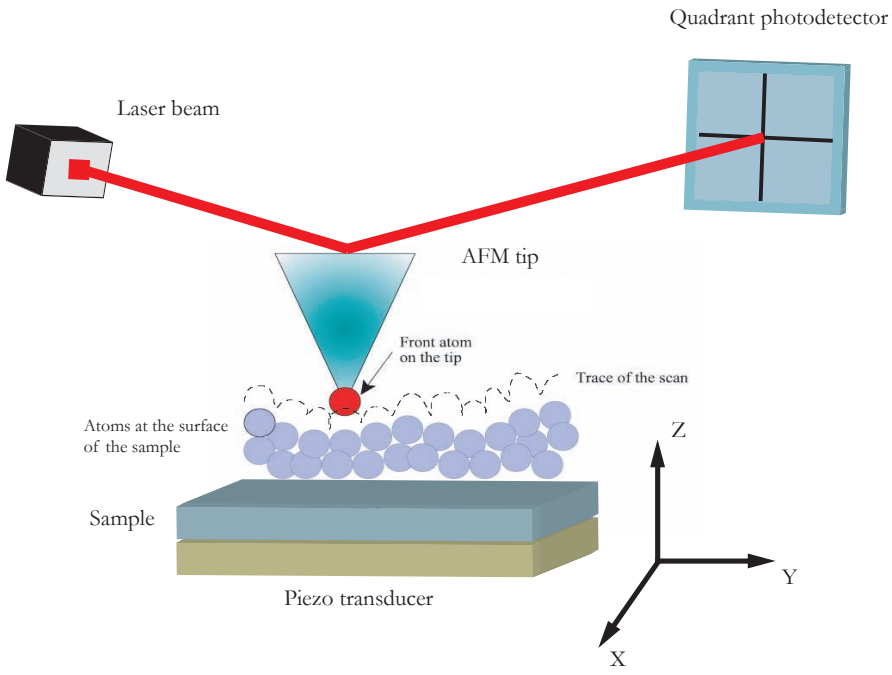

Figure 4.3: Principle of operation of an AFM.

aspect ratios. As illustrated in Figure 4.3, the tip is scanned across the surface in a constant force mode, and the tip-sample distance is varied to follow the contour of the surface. A laser beam which is reflected off the cantilever onto a 4 quadrant photo diode allows to record the tip displacement by measuring the beam deflection which is proportional to the difference of voltage between the upper and lower quadrants. In constant force mode, the cantilever's deflection is kept constant by controlling the tip-sample distance by the fine adjustment of a piezo which moves the sample and the tip relative to one another in the vertical direction.

Several modes of operation are possible. In contact mode, the tip exerts a strong force on the surface of the sample which can damage polymers and biological tissues. Matter can even be displaced over short distances, and the topography of the sample is therefore destroyed. In tapping mode, the cantilever is driven to oscillate close to its resonant frequency, and the tip comes into

contact with the surface only intermittently. Tapping is therefore preferred for scanning soft materials and deterioration is low since the contact between the tip and the surface is minimized. The phase signal can also give important information about the properties of the surface. The phase signal is the phase lag between the response signal and the drive signal, and it is related to the amount of dampening from the material during the scan. It can therefore be used to reveal contrast between materials with different mechanical properties in addition to topography. Since most of the materials we use are polymers, we performed AFM scans of all samples in tapping mode.

4.1.3 Contact Angle Measurements

Spreading of a liquid on a solid surface is a complex phenomenon which is determined by the nature of the intermolecular interactions between the vapor, the liquid and the solid phases in contact. It is expressed by the spreading coefficient S:

$$S = (\gamma_{\mathrm{SV}}) - (\gamma_{\mathrm{SL}} + \gamma_{\mathrm{LV}}) \tag{4.3}$$

where the three interfacial tensions are between the solid and the vapor (γ_{SV}), the solid and the liquid (γ_{SL}) and the liquid and the vapor respectively (γ_{LV}). Spreading occurs if the solid/liquid system has a lower energy than the bare solid surface, i.e. $S > 0$. In this case, the liquid is strongly attracted to the substrate and it spreads completely on the surface. If $S < 0$, the liquid only partially wets the surface and the angle between the surface of the substrate and the tangent to the curved liquid/air interface at the point of contact is defined as the contact angle θ.

Characterization of the surface energy of a solid material is commonly performed by the sessile drop technique using a contact angle goniometer. By de-

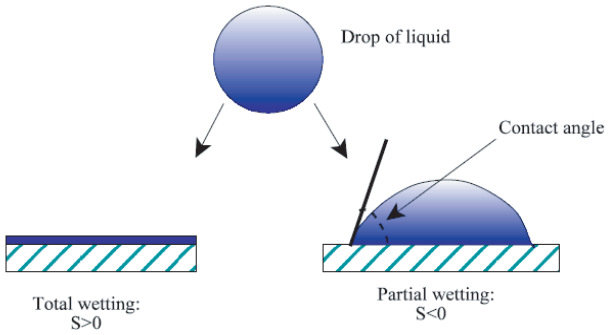

Figure 4.4: Wetting (left) and non-wetting (right) cases.

positing a small drop (usually below the capillary length to avoid deformation of the drop due to gravity effects) of liquid on the surface of a clean solid substrate, the contact angle θ can be measured with an appropriate optical system. This later is usually composed of a high resolution camera and a software to capture a cross-sectional image of the drop and analyze its contact angle. From a picture of a drop lying on a horizontal substrate like the one shown in Fig. 4.4, the contact angle is measured between the solid/liquid contact line and the tangential to the liquid/vapour interface. More advanced methods measure the profile of the drop to determine its contact angle. In static mode or at equilibrium, when all interfacial forces are balanced, this angle is called the equilibrium contact angle θ_e. If the drop is moving, the angle in front of the drop is called the advancing angle θ_a, whereas the angle at the back of the drop is the receding angle θ_r. These angles are usually not the same, and the advancing angle is always larger than the receding one. The equilibrium contact angle θ_e is always found in between these two extremes. The difference between the advancing and receding angle is the contact angle hysteresis.

The contact angle varies between the two "theoretical" limits 0° and 180°, which respectively correspond to total or complete wetting, and no wetting at

Figure 4.5: Photograph showing beads of water on the surface of the strongly water repellent Lotus leaf.

all. Such "extreme" contact angles are difficult to observe since defects and impurities prevent surfaces from being perfectly clean. A liquid drop on a highly non-wettable surface (also called super-hydrophobic surface) can reach large angles close to 180° due to the formation of air pockets onto which the drop is partially supported. In this case the drop assumes a nearly perfect spherical shape. Many examples of strong water repellency are provided by the plumes and fur of animals as well as by the surface of plants (Fig. 4.5). A regain of interest in super-hydrophobic surfaces has occurred in the past 10 years with the discovery that the superhydrophobicity of the Lotus leaf was enhanced by the micro- and nano-structures that cover its surface [61]. Strong liquid repellency (with contact angles approaching 180°) can be obtained by roughening the surface of a hydrophobic material on a micro- and nano-meter scale [62, 63].

The equilibrium contact angle θ_e made by a liquid on a chemically homogeneous, non-reactive and perfectly smooth solid surface is determined by Young's equation (1805) which expresses the balance of forces acting on the triple line where liquid, solid and vapor meet:

$$\gamma_{\mathrm{LV}} \cdot \cos\theta_e = (\gamma_{\mathrm{SV}} - \gamma_{\mathrm{SL}}) \tag{4.4}$$

Young's equation, however, doesn't take into account the effect of roughness and only holds for perfectly smooth surfaces. Wenzel [64] proposed a relation in which the contact angle θ_w is modified by a factor r which accounts for the roughness of the surface, and in which r is defined as the ratio of the real surface area (for a rough surface) to the projected area (as if the surface were smooth):

$$\cos\theta_w = r\cos\theta_e. \tag{4.5}$$

Cassie and Baxter [65] introduced another equation which takes into account the effective surface area of liquid in contact with the solid $f_{S/L}$ when part of the liquid is in contact with "pockets of vapour" on a rough solid surface:

$$\cos\theta_{CB} = f_{S/L}(\cos\theta_e + 1) - 1. \tag{4.6}$$

4.2 Deposition of Thin Films

Evaporation techniques rely on the fact that materials which are heated above their boiling point will start to evaporate. Controlled deposition of thin films was done by one of the two main evaporation methods performed in vacuum: thermal evaporation and electron beam evaporation. Thin polymer films, on the other hand, were obtained by spin-coating the polymer from a dilute solution.

4.2.1 Thermal Evaporation

The deposition of metallic thin layers was performed by thermal evaporation in the BOC Edwards evaporator (Auto 306). Owing to its simplicity, this method is widely used for coating surfaces with a large number of metals. Typically, a small amount of pure metal ($> 99.99\%$) is deposited in a boat made of a temperature

resistant metal (e.g. molybdenum), and is evaporated by resistive heating in a vacuum chamber. The sample, which is placed a few centimeters away from the boat, is then progressively coated by a thin film which condenses on its surface from the vapor phase. During deposition, the sample was rotated at constant speed in order to homogenize the thickness of the deposited film. All metal coatings (Au, Ag, Cr) were produced this way at low deposition rates between 0.01 and 0.03 $\mathrm{nm\,s^{-1}}$ to ensure a homogeneous and smooth film. Deposition was started once the pressure in the chamber was below 10^{-6} mbar. A thin layer of Chromium ($\sim$3 nm) was first deposited on the bare substrate to enhance adhesion of the metallic coating. The deposition rates and the thicknesses of the layers was monitored with a water-cooled crystal quartz placed inside the chamber.

4.2.2 Electron Beam Evaporation

Electron-beam evaporation uses an intense electron beam to heat a target material and cause evaporation in a high vacuum chamber. A thermoionic source or a tungsten filament are often used as the source of electrons. Unlike thermal evaporation, materials with a high melting temperature or with a low thermal conductivity such as silicon dioxide can be processed by electron beam evaporation. The intense vapor flux produced by this method also enables much higher evaporation rates than by thermal evaporation, thus it is useful for situations where a thick layer needs to be deposited. E-beam evaporation was used in this work to deposit protective silicon dioxide layers on thermally evaporated silver thin films. The deposition was performed at low rates (between 0.01 and 0.03 $\mathrm{nm\,s^{-1}}$) to ensure uniform and smooth films.

4.2.3 Spin-Coating of Polymer Films

Thin polymer films were produced by drop casting a solution of polymer onto a clean substrate, and spinning the sample at high velocity to evaporate the solvent. This created a flat, smooth and uniform polymer film. This process is the most widely used in research and industry nowadays to deposit thin and uniform organic films. Therefore, it is highly desirable to understand and control the properties of the spun film in an accurate manner. Very good film uniformity can be obtained over relatively large areas (10s of cm^2), and the thickness can be controlled within a few percent by varying the solution concentration, the viscosity and the spinning rate. Typical spinning rates are in the range 1000-10000 rpm, and for high vapor pressure solvents an homogeneous thin film is normally obtained in less than 30 s. If the film needs to be thicker (in the micron range), or if the solution is relatively viscous the evaporation of the solvent may take longer. It should nevertheless be emphasized that, because of the fast solvent evaporation during spinning, the physical properties of the cast film may be different than that of the bulk material because of non-equilibrium chain conformations. The consequence of this could be a film which has modified mechanical properties, or a film that becomes unstable with time or when heated close to, or above, T_g. We shall show in Chapter 7 that these out of equilibrium effects can be studied by using electric fields, and that the properties of the films can be changed by post processing them.

4.3 Lithographic Techniques

4.3.1 Photolithography

Optical lithography is a well established method by which regular arrays of patterns with micron-size features can be reproduced accurately into a light sensitive polymer resist (Fig. 4.7). First, a resist layer is spin-coated onto the surface of a silicon wafer and is exposed to a UV beam through a patterned mask to locally cross-link (negative resist) or degrade (positive resist) the resist. The exposed resist is then developed in a solvent to reveal the patterns which can next be transferred into an inorganic, permanent, substrate (e.g. silicon) by either chemical or physical etching. Two commonly used photo-resists are the positive AZ polymethylmethacrylate (PMMA) based series, and the negative-tone epoxy-based SU-8. Each resist comes into different grades which differ in viscosity and which allow the deposition of layers of different thicknesses. An interesting property of SU-8 is that it was specifically designed for applications where thick, chemically and thermally stable images of templates with micrometer-sized tall features are required. SU-8 can also be used to produce templates with permanent features by hardening the resist with a final high temperature annealing step.

For patterns smaller than approximately one micron, optical lithography cannot be used anymore because of its diffraction limited nature. Instead, electron beam lithography uses a focused electron beam to produce submicron features into an electron sensitive resist. The substrate with the patterned resist can be processed in a similar way as with optical lithography to produce a permanent master. This method has the advantage that very fine structures ($\sim 10\,\mathrm{nm}$) can be designed with a high accuracy, which is impossible to perform by optical lithography.

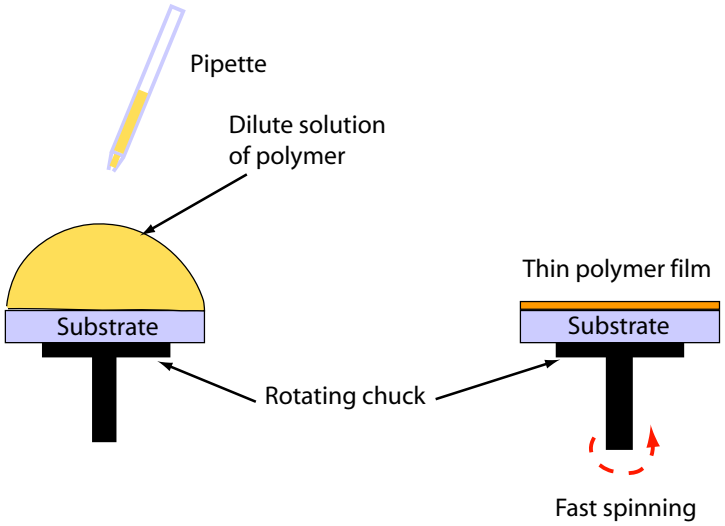

Figure 4.6: Schematic of the spin-coating process.

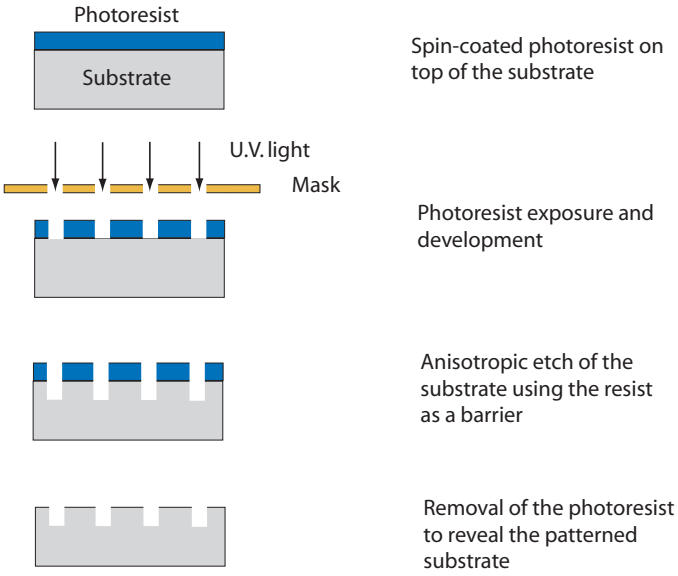

Figure 4.7: Schematic of the lithographic process used to pattern polymer photoresists and inorganic substrates.

4.3.2 Nanoimprinting

Nanoimprint lithography is a method by which micro- and nano-structures are reproduced into a plastic material by heating it above its glass transition temperature (T_g) and applying a force to imprint, or emboss, patterns from a structured mold (Fig. 4.8). The pressure is usually applied for a few minutes at the embossing temperature to ensure the plastic has time to flow into the features of the mask and completely fill them. Next, the polymer is cooled down below T_g and the force is removed. Finally, the mold is separated from the embossed material to reveal the imprinted patterns in the polymer substrate. The mold is an essential part of the NIL process since the imprinted patterns are an accurate reproduction of its features. Structured molds are typically produced by photolithography and e-beam lithography of silicon wafers.

As we'll show in Chapter 9, stiff inorganic silicon molds can be advantageously replaced by more economical and more durable plastic masks made of ethylene-tetrafluoroethylene (ETFE) which were developed by the author of this thesis.

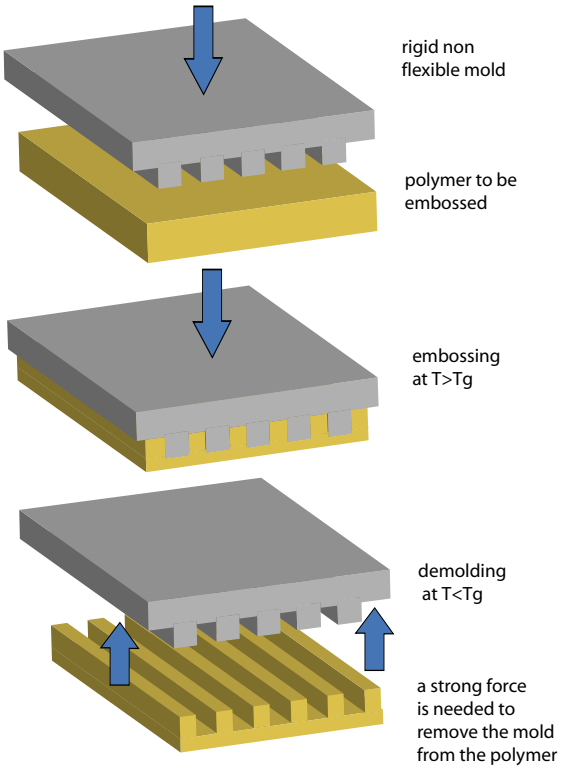

Figure 4.8: Schematic of the nanoimprinting process with a stiff inorganic mold.

Chapter 5

Optical Method to Measure Thin Film Surface Fluctuations

5.1 Introduction

Using a simple optical microscope, one can clearly observe thickness variations at the surface of a polymer film. Figure 5.1 shows white light images of EHD instabilities, along with the corresponding AFM images. In order to measure the characteristic time τ (Eq. 3.12) accurately we need to be able to measure the height of fluctuations as they develop on the surface of the film. Scanning probe techniques cannot be used in our set-up, and we therefore need to use another method which allow real-time measurements, a high accuracy of height determination and which doesn't perturb the formation of the instabilities.

A number of techniques are commonly used to measure height variations on surfaces or film thicknesses with a sub-nanometer resolution (e.g. ellipsometry, SFA, Fabry-Perot interferometry). The choice of one technique over another usually depends on the details of the surfaces to be analyzed and the type of measurements to be done. In our case, we can take advantage of the geometry

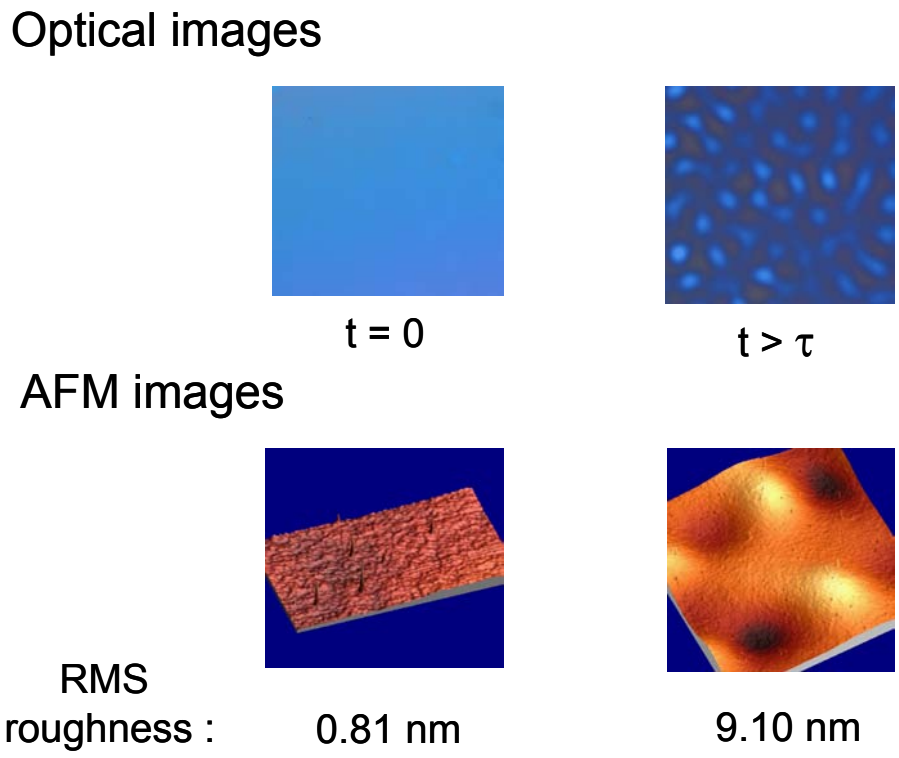

Figure 5.1: Thickness fluctuations in a polystyrene film due to an electric field. The top images were taken by optical microscopy in white light (image width is 80 μm). The bottom images are AFM scans showing the topography of the surface (image width is 20 μm). The images on the left (t=0) are for a flat and smooth film (no electric field), whereas the images on the right show EHD fluctuations at the surface of the film.

of our plate capacitor which can essentially be used as an optical cavity with a submicron gap. For this reason we decided to use an approach based on the interference of light beams inside a cavity (Fizeau fringes) to detect and measure small surface variations in thin polymer films which are destabilized by an electric field.

5.2 Interference of Electromagnetic Waves

5.2.1 Thickness Variation in a Thin Film

Thickness fluctuations in a thin polymer film can be observed, with a surprising amount of detail, using a simple optical microscope. Colors in the film are produced by the interference of white light at the film/substrate interface and at the polymer/air surface. This is illustrated in Fig. 5.2 which shows a succession of stripes of various colors on the surface of a nonuniform polystyrene film. The phenomenon of interference is one of historical importance in science (it served to demonstrate the wave nature of light), but it is also one of great technological interest. Nowadays, interferometry has become a standard in spectroscopy and in metrology, whereas interferometric lithography is commonly used for the micro- and nano-patterning of photoresist for microelectronics applications.

When two uncorrelated beams of light of superposed, the intensity of the resulting wave is just the sum of the two separate intensities. However, in the special case where the beams are either completely, or partially coherent, a more complex and elegant phenomenon occurs: light intensity modulation. As shown in Fig. 5.3 the intensity of the light resulting from the superposition of coherent beams is a succession of maxima and minima (bright and dark fringes). Coherent, or quasi coherent, beams can be produced by dividing an incoming

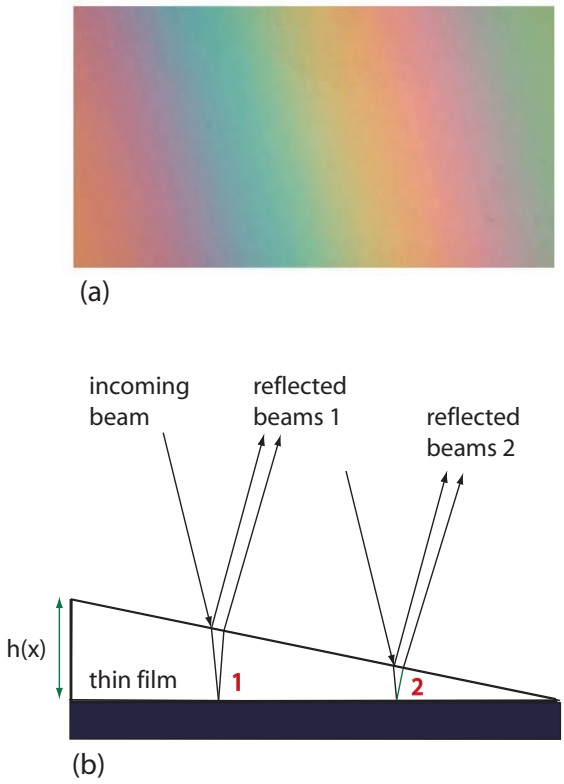

Figure 5.2: (a) Gradual variation of colors in a thin polystyrene film forming a "rainbow" pattern in white light. (b) Schematic showing the change in optical path inside the film at two different locations 1 and 2.

coherent, or quasi coherent, beam with small apertures, or slits, as in the famous experiment by Thomas Young (1802), and is called division of wave-front. Alternatively, the same beam of light can be split by using semi-transparent mirrors which transmit one part of the light and reflect another part (division of amplitude).

5.2.2 The Interference Term and the Irradiance

If we consider the superposition of the electric fields of two plane linearly polarized waves of frequency ω traveling in the directions $\mathbf{k}_1$ and $\mathbf{k}_2$, of the form:

$$\mathbf{E}_1(\mathbf{r},t) = \mathbf{E}_{01}\,\cos(\mathbf{k}_1\cdot\mathbf{r}-\omega t+\phi_1), \tag{5.1}$$

and

$$\mathbf{E}_2(\mathbf{r},t) = \mathbf{E}_{02}\,\cos(\mathbf{k}_2\cdot\mathbf{r}-\omega t+\phi_2), \tag{5.2}$$

the resulting intensity vector at a point in space is simply the vectorial sum of $\mathbf{E}_1$ and $\mathbf{E}_2$:

$$\mathbf{E}_t(\mathbf{r},t) = \mathbf{E}_1+\mathbf{E}_2. \tag{5.3}$$

If more than two beams are added, the same linear superposition principle holds. The typical frequency of the electric field is $\sim 10^{14}\,\mathrm{Hz}$ and because of this extremely fast oscillation, our eyes only detect a time averaged value of the radiant energy that emanates from an electromagnetic (EM) wave. This average quantity is called the irradiance I:

$$I = \epsilon\,\mathrm{v}\langle{\mathbf{E}_\mathrm{t}}^2\rangle \tag{5.4}$$

where v is the velocity of light in an homogeneous and isotropic dielectric

medium and ϵ its relative permittivity (or dielectric constant). In vacuum, v is replaced by c, and ϵ by ϵ_0, the permittivity of free space. I corresponds to the amount of energy carried by a wave, and it is what we measure with our eyes or any other light detector. When we talk about the interference created by two light beams, we therefore talk about the space modulation of the irradiance of the superposed beams. Omitting the prefactor, the irradiance I is expressed by:

$$\begin{aligned} I &= \langle \mathbf{E}_\mathrm{t} \cdot \mathbf{E}_\mathrm{t} \rangle \\ &= \langle {\mathbf{E}_1}^2 + {\mathbf{E}_2}^2 + 2\,\mathbf{E}_1 \cdot \mathbf{E}_2 \rangle \\ &= \langle {\mathbf{E}_1}^2 \rangle + \langle {\mathbf{E}_2}^2 \rangle + 2\,\langle \mathbf{E}_1 \cdot \mathbf{E}_2 \rangle \\ &= I_1 + I_2 + 2\,\langle \mathbf{E}_1 \cdot \mathbf{E}_2 \rangle. \end{aligned} \tag{5.5}$$

Therefore, the total irradiance is the sum of the irradiance of each wave, I_1 and I_2, plus an interference term whose amplitude varies with the difference in optical path, $(\mathbf{k}_1 \cdot \mathbf{r} - \mathbf{k}_2 \cdot \mathbf{r})$, between the two beams. After derivation, simplification and averaging, this interference term can be rewritten as:

$$2\,\langle \mathbf{E}_1 \cdot \mathbf{E}_2 \rangle = \mathbf{E}_{01} \cdot \mathbf{E}_{02}\, \cos(\mathbf{k}_1 \cdot \mathbf{r} + \phi_1 - \mathbf{k}_2 \cdot \mathbf{r} - \phi_2). \tag{5.6}$$

The final expression for the irradiance of two interfering EM waves is:

$$I = I_1 + I_2 + \mathbf{E}_{01} \cdot \mathbf{E}_{02}\, \cos\theta \tag{5.7}$$

where $\theta = \mathbf{k}_1 \cdot \mathbf{r} - \mathbf{k}_2 \cdot \mathbf{r} + \phi_1 - \phi_2$.

The interference term (Eq. 5.6) is what creates the modulation of the irradiance, or intensity as shown in Fig. 5.3. In the case of two beams with the same amplitude $E_{01} = E_{02}$, the irradiance varies between 0 and $4\,E_{01}$. In the reminder

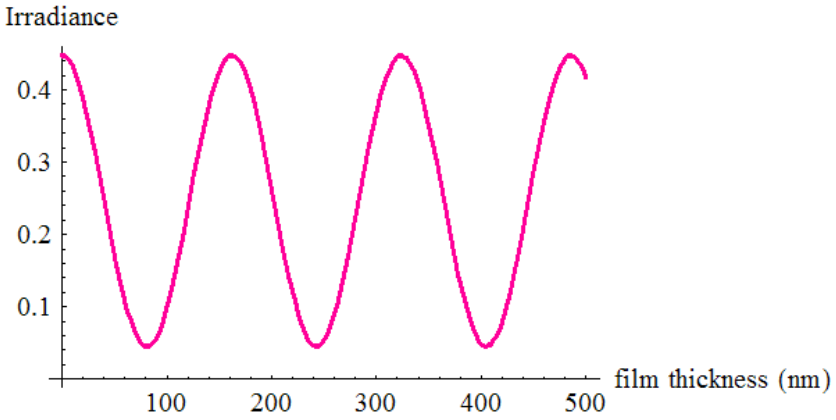

Figure 5.3: Interferences between the surface of a thin polystyrene film in air and a silicon/polystyrene interface forming a modulation of the reflected light intensity. The calculation is performed with λ_{light}=515 nm.

of this thesis, we'll also use the term "intensity" instead of "irradiance" when referring to light beams.

In a thin film, an incoming beam of light is split at the air/film interface, one part of the beam being reflected while the other part is transmitted in the film (Fig. 5.2 a). The transmitted beam undergoes reflection at the substrate/film interface and emerges from the top surface of the film in the same direction as the first reflected beam at the air interface. Because these beams are coherent they interfere with each other and produce a uniform color or light intensity if the film is uniform in thickness. However, if the thickness of the film $h(x)$ varies across its surface, the optical path of the recombinant beams will change and fringes of high and low intensity will be formed in monochromatic light. If white light is used, a gradual variation in color will be observed across the film (Fig. 5.2 b).

5.3 Interferences of Two and Three Beams

5.3.1 Reflection from Weakly Reflective Interfaces

Quantitative measurements of nanometric thickness variations in thin films can be achieved with a sub-nanometer resolution by measuring the reflected intensity of two interfering beams between weakly reflective interfaces [66, 67]. In our experimental set-up, the thin liquid film is separated from the top electrode by a thin air layer. This means that we do not have two interfaces reflecting light, as in the case of interferences occurring between the liquid/air interface and the underlying substrate, but we have three interfaces of similar reflectivity which contribute to the interference pattern (Fig. 5.4 a). We see from Fig. 5.4 b that the fringes have nearly the same intensity for the two beams (reflecting off interfaces 1 and 3 in Fig. 5.4), or for the three beams case. The evolution of the intensity with the film thickness for three beams is illustrated in Fig. 5.5 b.

- 1: SU-8/air, which has a reflectivity of ∼5.2%. The weak (∼1%) reflectivities of the ITO/glass and SU8/ITO interfaces are ignored in the calculation.
- 2: air/PS, which has a reflectivity of ∼5.2%.
- 3: PS/Si, which has a reflectivity of ∼20.5%.

The reflectivities are calculated using Fresnel equations using the values of indices of refraction given in table 5.1:

5.3.2 Thickness Measurement in a Thin Film

The change in intensity for a thin PS film of 120 nm is shown in Fig. 5.5 b, where it can be seen that a thickness variation in the film leads to a rapid change in

Material	n	k
SiO_2 (amorphous)	1.46	0.00
ITO	2.02	0.01
Si	4.27	0.01
Ag	0.13	3.05
SU-8	1.59	0.00
PS	1.59	0.01

Table 5.1: Optical properties of the materials used. The index of refraction (n) and the extinction coefficient (k) are given at 515 nm. The data is taken from refs. [68–76].

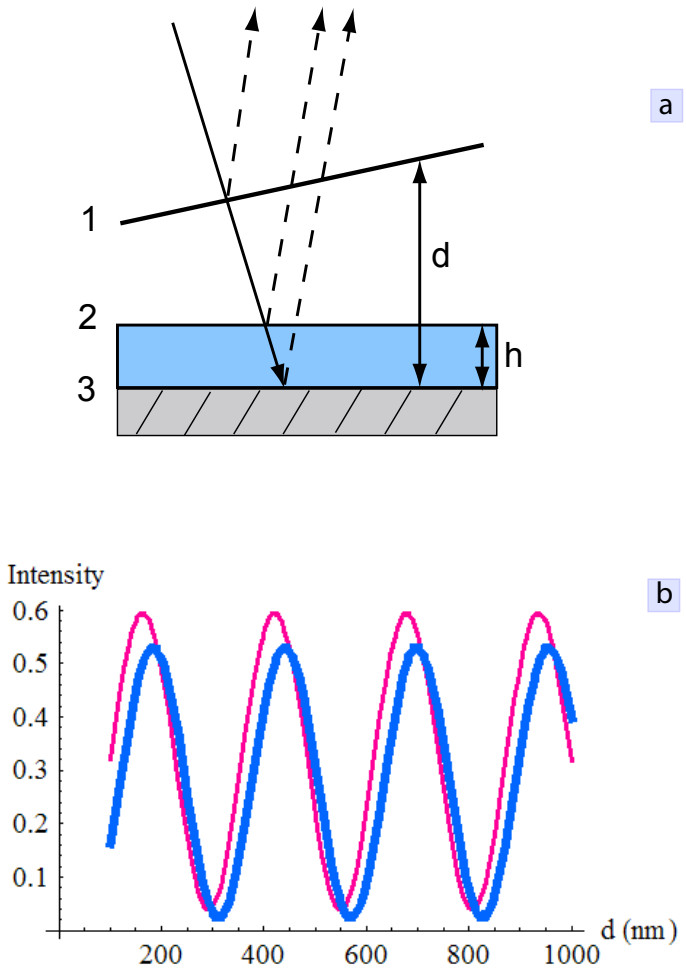

Figure 5.4: a) Schematic of light interferometry with 3 interfaces of low reflectivity. Reflection occurs at each interface and the recombination of each reflected beam creates a modulation of the irradiance which varies with the gap d. b) Intensity modulation of 2 (thick blue line) and 3 (thinner red line) interfering beams, giving rise to fringes as the gap d is varied. The calculation is done for $\lambda_0 = 515\,\mathrm{nm}$.

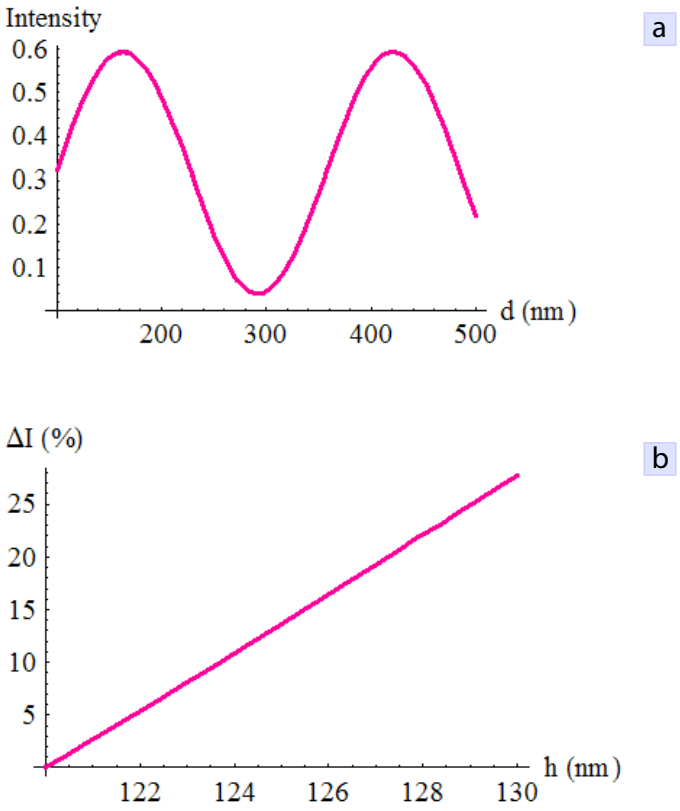

Figure 5.5: a) Intensity modulation of three interfering beams as a function of the gap d in a film of uniform thickness h. b) Intensity variation in % occurring in a film whose thickness increases up to 10 nm. The calculation is done for $\lambda_0 = 515\,\text{nm}$, $d = 250\,\text{nm}$ and for $h = 120\,\text{nm}$.

the intensity of the reflected interference pattern. Depending on the location of the instability with respect to the interference fringes, the reflected intensity from a 3 nm high fluctuation increases from ~ 7 to $\sim 20\%$. We calculated that a PS film thickness change from 120 to 123 nm at a local mimina (dark fringe) leads to an intensity increase of $\sim 20\%$.

For such small thickness variations, there is a corresponding recessed rim which forms around the peak and whose intensity varies in the opposite direction by roughly the same amount for small heights. This explains why small EHD fluctuations are so easily observed experimentally under an optical microscope. By monitoring the change in intensity of thin PS film destabilized by an electric field, one can therefore measure the time it takes for the instability to increase by just a few nanometers. We validated this analysis by comparing the thickness variation of a PS film by measuring the change in intensity of small surface instabilities with measures by AFM. We found a good agreement between the two methods with a typical error of $\sim 20\,\%$, which is approximately 1 nm for a 5 nm high fluctuation. This method was applied to the measure of the time constant τ for instabilities which are in the linear regime (see Chapter 7). Height fluctuations just a few nanometers high can easily be resolved and measured using the optical method we just described.

Chapter 6

Materials and Methods

6.1 Polymers

The thin polymer films were prepared by spin-coating a dilute solution of atactic polystyrene (PS) in toluene ($\sim 2-6\,\%$ by weight) onto clean silicon substrates at a speed of $\sim$6000 rpm. The solutions were filtered using a Teflon membrane with 100 nm pores (Whatman). The surface of the spin-coated films was free of defects and smooth when viewed with an optical microscope at a magnification of x100. Their thickness was measured by AFM, as well as the RMS roughness which was less than 0.5 nm. Polystyrene of four different molecular weights (M_w) were chosen to test the influence of chain length and entanglements on the mobility of the films: 10 kg/mol (PS_{10}), 27.5 kg/mol ($PS_{27.5}$), 113 kg/mol (PS_{113}), and 655 kg/mol (PS_{655}). The PS_{10} and PS_{113} were received from Polymer Labs (UK), and the $PS_{27.5}$ was ordered from Sigma-Aldrich (Switzerland). The polymers had a polydispersity of 1.02–1.04.

To study the influence of chain relaxation and reentanglement, annealing of some of the polystyrene films was performed in a vacuum oven at $\sim$0.1 mbar, and at temperatures ranging from $\sim$120 to 145°C. The samples were kept at

constant temperature and pressure for extended periods of times (hours to days depending of their M_w) before being cooled to room temperature. The detailed annealing times and temperatures are indicated in Chapter 7. All samples were kept in a clean glass container in the clean room before further use.

6.1.1 Other Polymers Used

Besides polystyrene, a number of other polymers were used for various purposes during the course of this work. For example, photosensitive polymers were used to create well defined micro-structures by photolithography. The commercial negative-tone epoxy-based photoresists SU-8 (MicroChem), as well as the positive polymethylmetacrylate (PMMA) based AZ resists (5204E) were used to prepare patterned substrates. SU-8 is designed for applications where thick, chemically and thermally stable images of templates with micrometer-sized features are required. It also served as a protective and insulating coating that was spin-cast onto the ITO electrode during the EHD experiments to prevent shorts when the electric field was applied between the two electrodes.

6.1.2 Substrate Preparation

It is noteworthy to emphasize the importance of working with clean, dust-free samples for the EHD experiments presented in this thesis. Since we are dealing with highly dust sensitive experiments, where very small air gaps are needed in order to create high electric fields, a lot of time and effort was devoted to sample cleaning, and extreme care in sample handling.

6.1.3 Silicon Substrates

The silicon substrates used in these experiments were P doped, one side polished, with a <100> orientation, and had a thin native oxide layer (∼2 nm) as received from the manufacturer (SI-MAT). Most of the sample preparation and all experiments were performed in a clean room environment (class 1000). The silicon wafers were first back-coated by thermal evaporation with ∼3 nm of chromium to promote adhesion, and ∼50–60 nm of gold to ensure good electrical conductivity. The typical base pressure was $2 \cdot 10^{-5}$ mbar with a typical evaporation rate of ≈0.02 nm/s. These substrates were then cut into squares of ∼ 10 mm in length, and plasma cleaned in an oxygen atmosphere (Diener Electronic, Germany) to remove organic contaminants. Just before spin-coating, the silicon substrates were cleaned again with a highly pressurized carbon dioxide snowjet to remove sub-micron particles [77]. The root-mean square, average and maximum peak to peak roughnesses of the silicon substrates after cleaning were characterized by AFM, and had the following typical values: RMS = 0.20–0.25 nm, R_a = 0.15–0.20 nm and R_{max} = 2–3 nm. The average static water contact angle on clean wafers was less than 10°, indicating a high surface energy.

In order to reduce the surface energy of the silicon substrates for some of the experiments, surface functionalization was performed by exposing the substrates to a vapor of HMDS molecules evaporated at ∼80–90°C from a solution in a closed glass container at atmospheric pressure. The substrates were exposed to the HMDS vapor for at least 5 hours, and then cooled down to room temperature and cleaned in isopropanol. After functionalization, the average static and dynamic water contact angles increased significantly, reaching values >90°, indicating a low surface energy.

6.1.4 Glass and ITO Substrates

Glass slides covered with a transparent layer of indium tin oxide (ITO) were cleaned using the following procedure. The slides were first wiped with acetone and isopropanol with a clean and dust free clean room paper, and then sonicated in acetone at 40-45°C for at least 45 min. The sonication procedure was repeated in the same conditions with isopropanol for another 45 min. Next, the substrates were blown dried in a nitrogen atmosphere, and further cleaned with a highly pressurized carbon dioxide snowjet at ∼200°C to remove any dust and small particles that could have adhered onto the surface of the slides. After cleaning, all samples were kept in a clean glass container in the clean room before spin-coating.

Because any irregularity on the surface of the electrode will create fluctuations in the electric field, it is important to make sure that the surfaces are homogeneous and smooth. For a typical experiment with a thin PS film of 100 nm, a spacing of 500 nm between the electrodes, and an applied voltage of 40 V, the average roughness of the ITO layer (∼1.1 nm) creates local fluctuations in the electric field of less than 1%.

6.2 Electric Field Experiments

6.2.1 Spacers

To perform the electric field experiments, the silicon/PS sample (first electrode) was placed on top of a second electrode made of glass covered with ITO to ensure electrical conductivity and optical transparency. A small air gap (∼0.2–1 μm) was created between the 2 electrodes with spacers made of silicon oxide colloids (Duke Scientific, Palo Alto, CA). The colloids were gently deposited

at the corners and edges of the polystyrene film with a soft stamp made of polydimethylsiloxane (PDMS, Sylgard 184, Dow Corning, USA).

6.2.2 Microscope

The electrodes were placed on a home-made heating stage mounted onto an inverted optical microscope (Zeiss MAT200, Germany) to allow observation of the film during the experiment (Fig. 6.1). White light from an halogen source was passed through an interference filter with a narrow bandwidth (∼1 nm) to create a beam of quasi-monochromatic light. The coherence length of the beam was much greater than the depth of the optical cavity (∼200–1000 nm), thereby ensuring the production of interferences when two or more beams were recombined upon reflection inside the cavity. Interference filters with a mean wavelength of 515 nm and 532 nm were used. Instead of using a filter, we also tried to replace the lamp with a laser beam going through the same optical path as the white light inside the microscope. However, it was found that reflections of the beam on the multiple lenses inside the microscope created a complex pattern of interferences difficult to interpret. The high coherence length of the laser is in this case problematic. Due to the confined geometry of our set-up, it was not possible to use the laser as an independent source without drastically changing the design of the experiment, which was opted against.

6.2.3 Heating Stage

The home made heating sample holder was made of two parts. The first part consisted of a heating element, and the second part was an insulating plastic cover, enveloping the whole heating device. This latter was made of either copper or brass with four tubular heating cartridges of 60 W, placed at equal distances

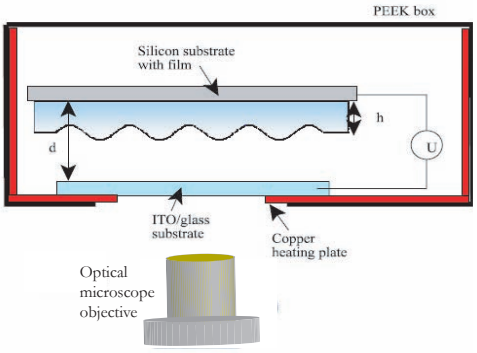

Figure 6.1: (a) Schematic of setup used to heat the samples and perform the electric field experiments.

from the center of the sample on each side of a square. A small (∼15 mm) opening was made at the bottom of the sample holder to allow observation of the polymer film with the inverted microscope. The insulating cover was made of polyaryletheretherketone (PEEK) [78], which is a rigid (elastic modulus ∼3.9 GPa) and highly heat resistant polymer (melting ∼343°C), to ensure structural integrity as well as good thermal and electrical insulation during the experiment. The ITO electrode was secured to the bottom part of the heating device with ceramic clips to ensure good thermal transfer from the heater and to prevent any motion during the experiment. The backside of the silicon/PS sample was "glued" with silver paste to a small and conductive copper block which was electrically connected to the power generator. The PS film was then placed facing the ITO side of the second electrode. A difference of voltage was applied between the backside of the silicon/PS sample and the ITO electrode. The electrical connections and the voltages applied to the electrodes were checked before each experiment.

6.2.4 Control of the Temperature

During the experiment, the thin film was heated above the bulk T_g of PS until a steady temperature was reached. The temperature was set with a steady and accurate temperature controller (Eurotherm 3500), and measured with a highly sensitive chromel-alumel (K) thermocouple located close to the back surface of the silicon substrate. The choice of the thermocouple was dictated by the accuracy of the probe in the temperature range of the experiments, but also by the necessity to use highly flexible and temperature resistant wires. Thin K thermocouples coated with a polytetrafluoroethylene (PTFE) layer were found to be the best candidates. The thermocouples were temperature calibrated with a platinum PT100 sensor (Labfacility, UK; 1/10 class B , tolerance of 0.10°C at 150°C) before the experiment. Because silicon has a relatively good thermal conductivity ($\sim$100 $\mathrm{W\,m^{-1}\,°C^{-1}}$ at 150°C for single crystals) [79, 80], we don't expect much difference in temperature between the top surface and the back side of the wafer. Polystyrene has a much lower conductivity ($\sim$0.17 $\mathrm{W\,m^{-1}\,°C^{-1}}$) [81, 82], but because the film is so thin, the difference in temperature across the polystyrene film is expected to be negligeable. We measured the heat flux away from the glass surface in the temperature range 135-160 °C and found a value of $\sim 2.3 \cdot 10^3\,\mathrm{W\,m^{-2}}$. Assuming the same flux across the air/PS/silicon multilayer, the drop in temperature is $\sim$0.05 °C across the air gap due to conduction through the 150 nm silica spacers. The temperature differences across the PS film and the silicon slab are negligeable in comparison ($\sim 1.4 \cdot 10^{-3}$ °C and $\sim 1.1 \cdot 10^{-2}$ °C respectively). [1]

[1] Fourier's law equates the heat flux Q to the gradient of temperature $\partial T/\partial z$ multiplied by the thermal conductivity κ:

$$Q = -\kappa \frac{\partial T}{\partial z}. \tag{6.1}$$

Assuming Q$\sim$ $2.3 \cdot 10^3\,\mathrm{W\,m^{-2}}$, and $\kappa_{silica}\sim$1 $\mathrm{W\,m^{-1}\,°C^{-1}}$, the temperature difference across a silica thickness of 150 nm is less than 0.05 °C. The conductivity of PS is κ_{PS}

Test experiments using sensitive K thermocouples placed at three locations near the surface of the film and near the surface of the ITO/glass slide showed that the temperature at the surface of the film was approximately 0.2 °C higher than the temperature measured by the thermocouple at the back of the substrate in the range of temperatures considered in these experiments (135–160 °C). This is in good agreement with the calculation above, and within the resolution of our setup. The temperature measured by the thermocouple was therefore corrected by this amount to reflect the actual temperature at the surface of the film.

6.2.5 Measurement of the Characteristic Wavelength

Accurate determination of the characteristic wavelength λ_m is necessary in order to get quantitative information regarding the evolution of the instabilities with time. The measurements of λ were therefore performed by sampling a large enough number of points within a relatively narrow spatial window corresponding to a nearly identical electrostatic pressure. Since the pressure in the film varies along the direction of the wedge, the wavelengths need to be selected in the direction perpendicular to the steepest gradient in the plate spacing. We are helped by the fact that light interference fringes are also parallel to the sharpest increase in air gap. The distance between neighboring instabilities was measured, and λ_m was determined from the mean of the nearest neighbors. Two methods were used to measure nearest neighbours. The preferred method was to use a program that I developed to perform this task and plot the distribution of near neighbours. The program gives the distribution of distances with first, second and third neighbors as shown in Fig. 6.2. The second method was to simply manually measure the distance between the instabilities in a zoomed in image. Both methods yielded very close values, and standard deviations from

$\sim 0.17\,\mathrm{W\,m^{-1}\,°C^{-1}}$.

the mean were usually typically less than 10%.

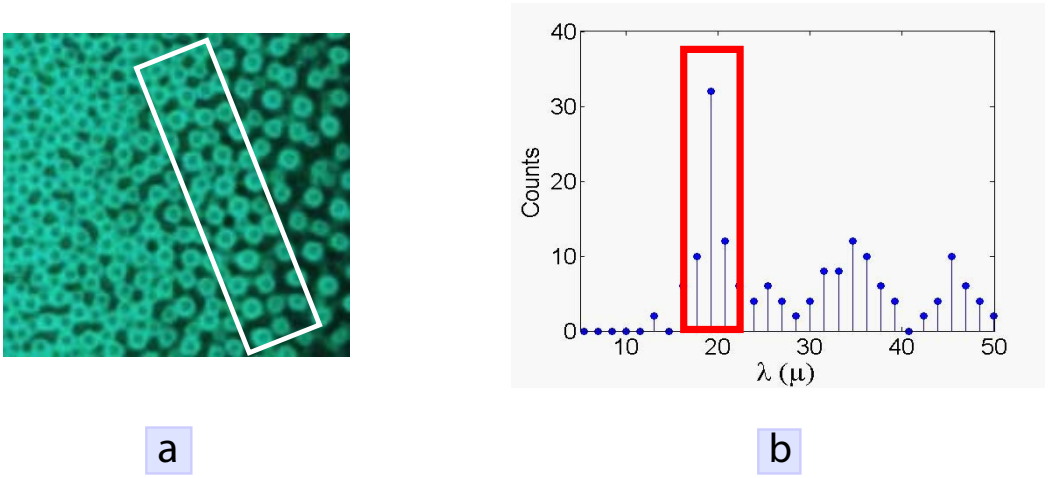

Figure 6.2: Observation of EHD instabilities with relatively large wavelengths on the surface of a polystyrene thin film. The characteristic wavelength λ_m is determined by measuring the distance between instabilities inside the box (a). The distribution of distances between first, second and third nearest neighbors is shown in (b). The nearest neighbors represent λ_m.

6.3 Preparation and Characterization of Reflective Surfaces

Surfaces with a high reflectivity are needed in order to use the capacitor as an optical cavity with sharp Fizeau fringes. This is the method we used to measured the height of surface fluctuations over time (for fluctuations growing up to several hundred nanometers). After evaporation of ∼3 nm of Cr to promote adhesion, a thin layer of silver was deposited onto the substrates by thermal evaporation in vacuum (see the Experimental section). The deposition was performed very slowly at rates of ∼0.1–0.3 $\mathrm{nm.s^{-1}}$ to ensure a smooth and uniform film. The thickness of the silver layer on the semi-transparent (ITO) electrode was ∼18 nm,

which ensured a high enough reflectivity (see table) and a good visibility of the surface of the sample through the electrode. A thicker (90–100 nm) layer of silver was evaporated onto the silicon substrate which needed to be highly reflective. The reflectivities of the two layers were measured with a laser beam at 532 nm at near normal incidence and are indicated in Table 6.1 .

Silver films are subject to tarnishing over time when exposed to air, and this results in a decrease of reflectivity. Moreover, since we perform the EHD experiments at temperatures up to $\sim 170\,^{\circ}\mathrm{C}$, we needed to know how this could affect the stability of the silver layer for periods of time similar to the duration of the experiment. We performed surface characterization of the silver films heated up to 300 °C in an oven and for up to 12 hr. The thick films deposited on silicon did not change appreciably when heated at 300 °C for 12 hr. The films stayed relatively smooth (their RMS roughness increased to 14.5 nm) and highly reflective. In contrast, the thinner films used as a semi-transparent layer, completely changed morphology when heated above $\sim$150 °C. Figure 6.3 shows images of the films surface for as deposited films, and for the annealed thin films. The thinner films dewet and form islands, which increases their roughness and decreases their reflectivity. A simple visual observation was enough to see the strong decrease in reflectivity of these samples. In order to prevent this morphological change, we deposited a protective coating of SiO_2 on top of the silver layer by e-beam evaporation. The reflectivity of the sample after deposition of this oxide layer decreased by 2% compared to the reflectivity of the Ag layer only (see Table 6.3). Visual observation of the samples before and after the EHD experiments showed no loss of reflectivity. Characterization of the surface of the protective layer by AFM also showed no noticeable change in roughness after the experiment.

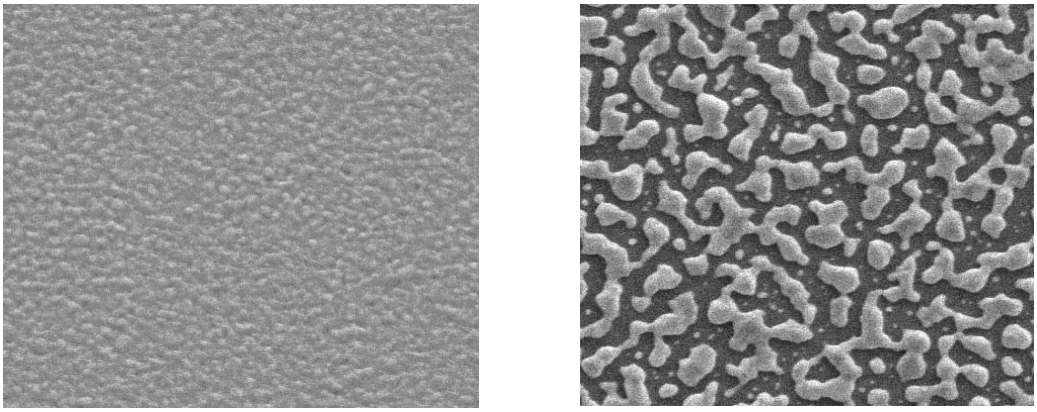

Figure 6.3: Surface of silver films imaged by SEM. a) Typical morphology of a silver film deposited by thermal evaporation. b) Dewetting occuring on a thin silver film of ∼18 nm. Images width is 4 μm.

	ITO	Si
RMS roughness (nm)	2.2	0.2
Thickness of Ag (nm)	18	90
Reflectivity of Ag (%)	66	94
RMS roughness of Ag (nm)	8.0	5.2

Table 6.1: Properties of the thin silver films used in this study. The thin Ag film (18 nm) was evaporated on ITO, whereas the thicker film (90 nm) was evaporated on a silicon substrate. A thin, ∼3 nm Cr layer was first deposited to promote adhesion of the Ag. The reflectivity was measured at 532 nm and 10 ° angle of incidence from the normal to the surface.

Chapter 7

Rheology of Thin Liquid Films

The measure of the characteristic time of destabilization τ (Eq. 7.1) for an EHD instability gives information about the hydrodynamic response of the thin film when subject to an external perturbation. The time constant, τ, is directly proportional to the viscosity of the film η. Electric fields therefore provide a way to probe the rheology of thin liquid films. In this chapter we measured the viscosity of thin PS melts, and we found an increased chain dynamics in spin-coated films. In contrast, films which were previously annealed for long times did not show deviations from the bulk [83].

7.1 Measurement of the Time Constant

7.1.1 Experimental Set-Up

The experimental set-up consisted of two nearly parallel plates (see Fig. 7.1) which were used as a capacitor and as an optical cavity, placed inside a home-made oven mounted onto an inverted microscope (see Chap. 6.2). The instabilities were observed in real time through a semi-transparent electrode made of ITO, and optical images were recorded with a monochromatic light of 515 nm.

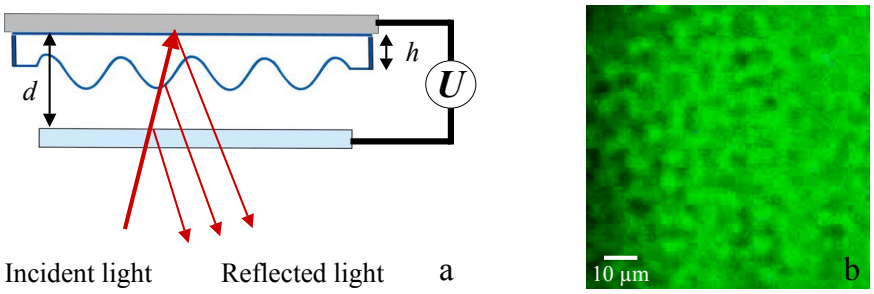

Figure 7.1: Experimental setup and image of an instability. (a) Schematic of the experimental setup for film destabilization in an electric field. The polymer film is sandwiched between two parallel plates, which serve simultaneously as plate capacitor electrodes and as an optical cavity. (b) Example image of the onset of an electric field driven surface instability, showing fluctuations on the surface of the thin film.

The small wedge which is always present between the electrodes allowed us to follow the formation of the instability as a function of the characteristic wavelength λ_m. Since λ_m increases with larger air gaps (lower electric fields), several values of τ and λ_m can be recorded during an experiment. In a typical experiment, the assembly was heated to a temperature $T > T_g$ and a voltage was applied to the two plates, defining the start of the experiment ($t = 0$).

7.1.2 Theory

The applied electric field resulted in the evolution of a surface wave (EHD instability). The onset of the surface wave on the polymer film gave rise to a distortion of the interference pattern of the optical cavity, and the local thickness variation was measured from the change in intensity (see Chap. 5). Local thickness changes as small as 1 nm could be resolved by measuring the phase shift in the interference pattern.

The quantity of interest in this experiment is the characteristic time for the onset of the instability

$$\tau = \frac{3\eta}{\gamma h_0^2 (h_0 + 3b)} \left(\frac{\lambda}{2\pi}\right)^4. \tag{7.1}$$

which scales linearly with the ratio of the viscosity η and the surface tension γ. The characteristic wavelength λ is given by Eq. 7.2.

$$\lambda = 2\pi\sqrt{\frac{2\gamma U}{\epsilon_0\epsilon_p(\epsilon_p-1)^2}}E_{\mathrm{p}}^{-\frac{3}{2}} \tag{7.2}$$

with ε_{p} the dielectric constant of the polymer, ε_0 the vacuum permittivity, U the applied voltage and E_{p} the electric field in the film.

The analysis of fluctuations at the surface of the film is performed by considering the growth of an EHD instability in the linear regime. The electrostatic pressure is the driving force which determines which mode grows against the stabilizing effect of the surface tension (see Chapter 2.4.3). Thermally induced capillary waves whose wavevector correspond to the fastest growing mode in the linear stability analysis are exponentially amplified. In the limit where the surface amplitude ζ is much smaller than the wavelength of the instability λ and the initial film thickness h_0, the perturbation of the film is governed by a linear stability analysis (see Chapter 2.4):

$$h(x,t) = h_0 + \zeta e^{iqx+\frac{t}{\tau}}. \tag{7.3}$$

This equation yields the time dependence of the emerging surface undulation $h(x,t)$ triggered by the applied electric field. We can therefore use Eq. 7.3 to determine τ by measuring the time needed for the instability to grow by a small amount (typically a few nm) in the linear domain using the optical method describe in Chapter 5:

$$\ln\left(\frac{h(x,t)-h_0}{\zeta}\right) = \frac{t}{\tau}. \tag{7.4}$$

The surface roughness of thin liquid PS films due to thermal fluctuations was measured by X-ray scattering and by small angle neutron scattering [84,

85]. The RMS values for PS melts in the range 120-180 °C are typically ∼0.3–0.5 nm, which gives a surface amplitude ζ ∼0.5–0.7 nm in the same range of temperatures. These values are in good agreement with a direct measure of ζ in a thin PS film [86]. The magnitude of λ in equation 7.2 accurately reflects the balance of forces acting on the free interface, irrespective of the film rheology [87]. The value of τ, on the other hand, is directly proportional to the viscosity. The observation of the evolution of an electrohydrodynamic surface wave therefore allows to disentangle the force balance driving the instability from the rheology within the film, providing an effective way to probe the flow in thin liquid layers.

7.1.3 Observation of Fast Dynamics in Spin-Cast Films

Thin films of polystyrene were prepared by spin-coating from a semi-dilute toluene solution (∼3–6% by weight) onto a silicon substrate. The value of τ measured on thin spun-cast films of various molecular weights above M_e (e.g. $PS_{27.5}$ and PS_{113}) (see Chap. 6) were consistently much lower than the prediction of Eq. 7.1. According to the same equation, slip at the interface between the melt and the substrate could fasten the flow of liquid in the film, and could decrease the observed characteristic time. Figure 7.2 shows that the values of τ as a function of λ can be made to fit Eq. 7.1 with the addition of a slip length b (see section 2.3.3). In the case of $PS_{27.5}$ on oxidized silicon shown in Fig. 7.2, a slip length of ∼500 nm would fasten the destabilization of the film and account for the measured values.

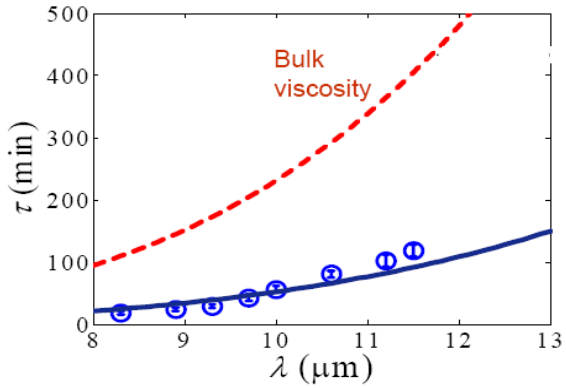

Figure 7.2: Characteristic destabilization time τ as a function of instability wavelength λ for a thin film (135 nm) of $PS_{27.5}$ spun-cast on a oxidized silicon substrate. Temperature of the experiment: 142 °C. The dashed line is the prediction of equation (7.1) using the bulk viscosity, the solid line is a fit of equation (7.1) to the data by addition of a slip length $b \sim$500 nm.

7.2 Influence of the Boundary Condition at the Solid/Liquid Interface

7.2.1 Characterization of the Surfaces

To determine the role played by the chemistry of the solid at the interface with the thin liquid melt, experiments were performed with two types of substrates with different wetting properties for PS. One substrate was a silicon/SiO_2 surface treated by oxygen plasma, whereas the second surface was a functionalised silicon/SiO_2 surface covered with a monolayer of hexamethyldisilazane (HMDS) in vapor phase. The roughness of the surface was identical to that of bare silicon (RMS=0.24–0.25 nm). The contact angles made by two polar liquids (glycerol, water) and one non polar liquid (toluene) on each surface were measured with a goniometer, and the surface energy of both surfaces was estimated using the Young-Good-Girifalco-Fowkes equation [88]. We found that the HMDS treated surface had a much lower surface energy than that of the oxidized silicon surface (see Table 7.1). Next, the contact angle of a melted PS drop was measured on each substrate at $\sim$150 °C and the interfacial energy between the PS melt and each surface was deduced by using the Young-Laplace equation which relates the surface and interfacial energies of the solid, the liquid and the vapor to the contact angle of the liquid on the solid (see Chapter 4, Eq. 4.4). The interfacial tension of PS measured on the HMDS treated surface was substantially lower than on the untreated silicon/SiO_2 substrate.

7.2.2 Measurement of τ on Two Different Substrates

Electric field experiments were performed on both surfaces with $PS_{27.5}$ at 142 °C. Although the functionalised substrate had a substantially lowered interfacial

	SiO_2	SiO_2 + HMDS
RMS roughness (nm)	0.22	0.24
γ_{sv} (mN/m)	71.0	30.9
γ_{sl} (mN/m)	54.8	18.7

Table 7.1: Roughness and wetting properties of the two solid surfaces used to perform the slip experiments. γ_{sl} is the interfacial energy between the solid surface and a PS melt at ∼150 °C.

energy with PS compared to the bare silicon wafer, the characteristic destabilisation times are indistinguishable (Fig. 7.4 a). This indicates that the solid boundary does not play a significant role during the early stage of destabilisation. This is likely due to the fact that the small undulation created at the surface of the film at the onset of the instability (∼1/100th of the film thickness) does not give rise to large enough stresses needed to induce slip at the solid/liquid interface. A calculation of the lateral stress induced by the electric field at the surface of a thin-film shows that the stress is indeed relatively weak (order of magnitude 100 Pa) at the early stages of destabilization for the typical conditions used in our experiments. Figure 8.11 b shows the evolution of the stress in function of the amplitude of the lateral fluctuation induced by the electric field for a given set of experimental parameters. From this calculation, it is shown that the lateral stress increases rapidly with the amplitude of the fluctuation, and can reach significant values on the order of thousands of Pa (which may be large enough to induce slip in the thin-film) when the amplitude of the surface fluctuation reaches ∼20-25 nm.

7.2.3 Possible Explanation for the Reduction in τ

From equations 7.1 and 7.2, the parameters that can be responsible for the change in τ are: the surface tension (γ_{PS}), the dielectric constant of PS (ε_{PS}) or the viscosity (η). The surface tension and dielectric constant of PS are well documented ($\varepsilon_{PS} = 2.5$, and $\gamma_{PS} = 27.5 - 32.7\,\mathrm{mN/m}$ in the range of temperatures considered from ∼130–190 °C). Experimental work has shown that the value of the dielectric constant was unchanged when a strong DC electric field, similar to the one used in our experiments, was applied to polar molecules [89]. The surface tension of thin PS films was also found to be in good agreement with the bulk value. Since the surface tension decreases with temperature, it still needs to be corrected accordingly [90]. This correction is nevertheless small and does not account for the large decrease in τ observed experimentally. The only likely parameter that is able to account for the increased film mobility is therefore the viscosity η. There has been reports of change in viscosity in thin films. Some studies on films $> 100\,\mathrm{nm}$ also showed abnormal rheological behavior and increased mobility [91–93]. Other experimental results report no change in viscosity in thin films both below and above 100 nm [94]. Films annealed on a liquid substrate show a different behaviour [95] compared to similar systems on a solid support. A change in film rheology can also arise from a change in free volume when polymer nanoparticles are added to a chemically identical polymer melt [96]. However usually films thicker than ∼100 nm are considered as having the same properties as the bulk. We nevertheless decided to investigate a possible change in viscosity in spin-cast films.

7.3 Viscosity of Bulk PS Melts

The viscosity of bulk PS was measured using a parallel plate rheometer. Thick layers ($\sim$300 μm) of the same material used for the EHD experiments were layed down on the rheometer stage from a dilute solution and slowly allowed to evaporate for several hours between 60 and 70 °C. Next, the thick films were heated in several stages up to 150 °C and left for $\sim$2–3 hours at 150 °C before performing the measurements. A frequency sweep (0.5 to 5 rad/s at an applied stress of 10 Pa) and a stress sweep (0.1 to 100 Pa at 1 rad/s) were performed at 150 °C to determine the domain of constant viscosity. The viscosity was measured as a function of temperature from 130 to 150 °C (ramp 1 °C/min) for a given applied stress at a frequency of 1 rad/s. Since shear rates are low in the early stages of destabilization of a thin liquid film with electric fields, the bulk viscosity of PS was also measured at low shear rates between 1 and 10 Pa [1]. The data was fitted and the viscosity outside the range 130– 150 °C was inferred from the measured data. The measured viscosity was found to be in good agreement to that reported in the literature for low shear rates [97, 98], as shown in Fig. 7.3. The measurement of the viscosity for the higher M_w polymers (PS_{113} and PS_{655}) was directly taken from the literature [97, 98].

7.4 Measurement of τ on Spun Cast and Annealed Films

The solid lines in Figure 7.4 are fits of equation 7.1 to the data, postulating a viscosity reduction by factors of 5 and 6 for $PS_{27.5}$ and PS_{113}, respectively. Experiments with a much higher molecular weight polymer in Fig. 7.4 e show

[1] Varying the applied stress from 1 to 10 Pa showed no change in viscosity in the temperature range used.

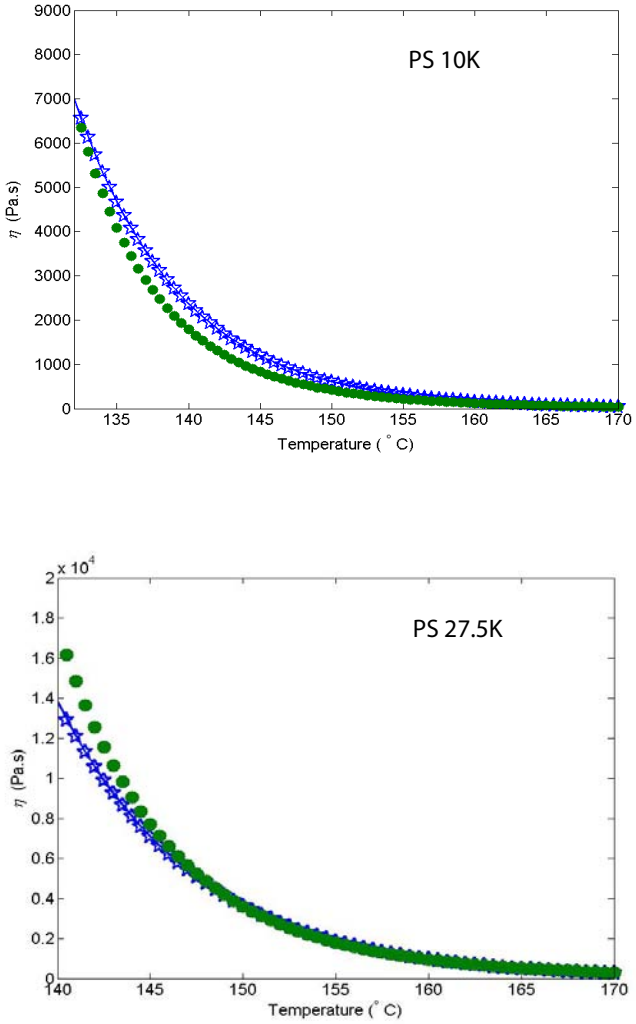

Figure 7.3: Viscosity of bulk PS measured with a parallel plate rheometer. The stars represent the viscosity measured with a plate rheometer in this study. The dots are viscosity from reference [97, 98] that were measured using a capillary rheometer.

an effective viscosity reduction by nearly four orders of magnitude. Since the measured bulk viscosity agrees with the literature values for PS, the only likely explanation for the mobility reduction in Fig. 7.4 arises from non-equilibrium effects caused by the film deposition procedure. To test this hypothesis, films cast from $PS_{27.5}$ and PS_{113} were heated at $T > T_g$ for times between 22 h and 145 h (Table 7.2). The comparison of destabilisation experiments in Fig. 7.4 b, with the prediction of equation 7.1 confirms that the bulk viscosity in the films is recovered after annealing. The good agreement of experiments and prediction validates our experimental approach. It also indicates that the polymer chains of sufficiently high molecular weights in spin cast film have a quenched structure that gives rise to a significantly lowered effective viscosity. The annealing of the film for sufficiently long times removes this non-equilibrium effect. The destabilization of PS_{10} films which have a M_w below the entanglement molecular weight M_e of PS in Fig. 7.4 f does not show this effect: the data for as-cast and annealed films are both described by the bulk viscosity.

7.5 Non-Equilibrium Chain Conformations

7.5.1 The Spin-Coating Process

The sketch in Fig. 7.5 illustrates a possible mechanism that is able to account for the non-equilibrium behaviour in spin-cast films. In the initial phase of spin-coating the polymer forms a semi-dilute solution in a good solvent. During spinning, the solvent rapidly evaporates, increasing the polymer concentration in the film (see Section 4.2.3). In thermal equilibrium, the number of entanglements per chain with surrounding chains increases with polymer concentration. This leads to an increasingly entangled semi-dilute solution with decreasing solvent

concentration. Since this increase in entanglements can only occur by chain reptation, the mobility of the chains must be high enough for the entanglement density to increase further. With increasing polymer concentration this process is progressively slowed down and comes to a stop when the glass transition of the coils is reached. At this point, the film still contains $10 - 20\%_{\mathrm{vol}}$ solvent, which mostly evaporates during the late stage of spin-coating [99]. The slow-down of chain mobility and chain collapse is therefore likely to give rise to an entanglement density per chain which is lower compared to the melt-equilibrium. Since the melt viscosity of polymers arises from the entangled nature of the chains, this qualitatively explains the lowered effective viscosity of the as-cast films. Annealing the film at $T > T_{\mathrm{g}}$ for times exceeding the reptation time equilibrates the chains to their fully entangled nature which is characteristic for the equilibrated melt. This is in good agreement with other studies which showed that the chain conformation in thin films were the same as in the bulk [84], and that the viscosity of thin films was also similar to the bulk [100] for samples annealed for long times well above T_{g}.

7.5.2 Non-Newtonian Rheology of Spin-Cast Films

The results in Fig. 7.4 indicate that the times required to destabilise the films were below the relaxation times of the chains. Careful examination of the data in Fig. 7.4 a,c shows that the data for large values of λ (low applied electric fields) lie above the curve fitted to the data with small λ. This is probably due to chain relaxation during the destabilization experiment. This effect is better seen when plotting the two PS_{113} data sets in terms of the stress-strain relation in Fig. 7.6a for the onset of the instability. The lateral stress arises from the difference in pressure between adjacent undulation maxima and minima imposed by the

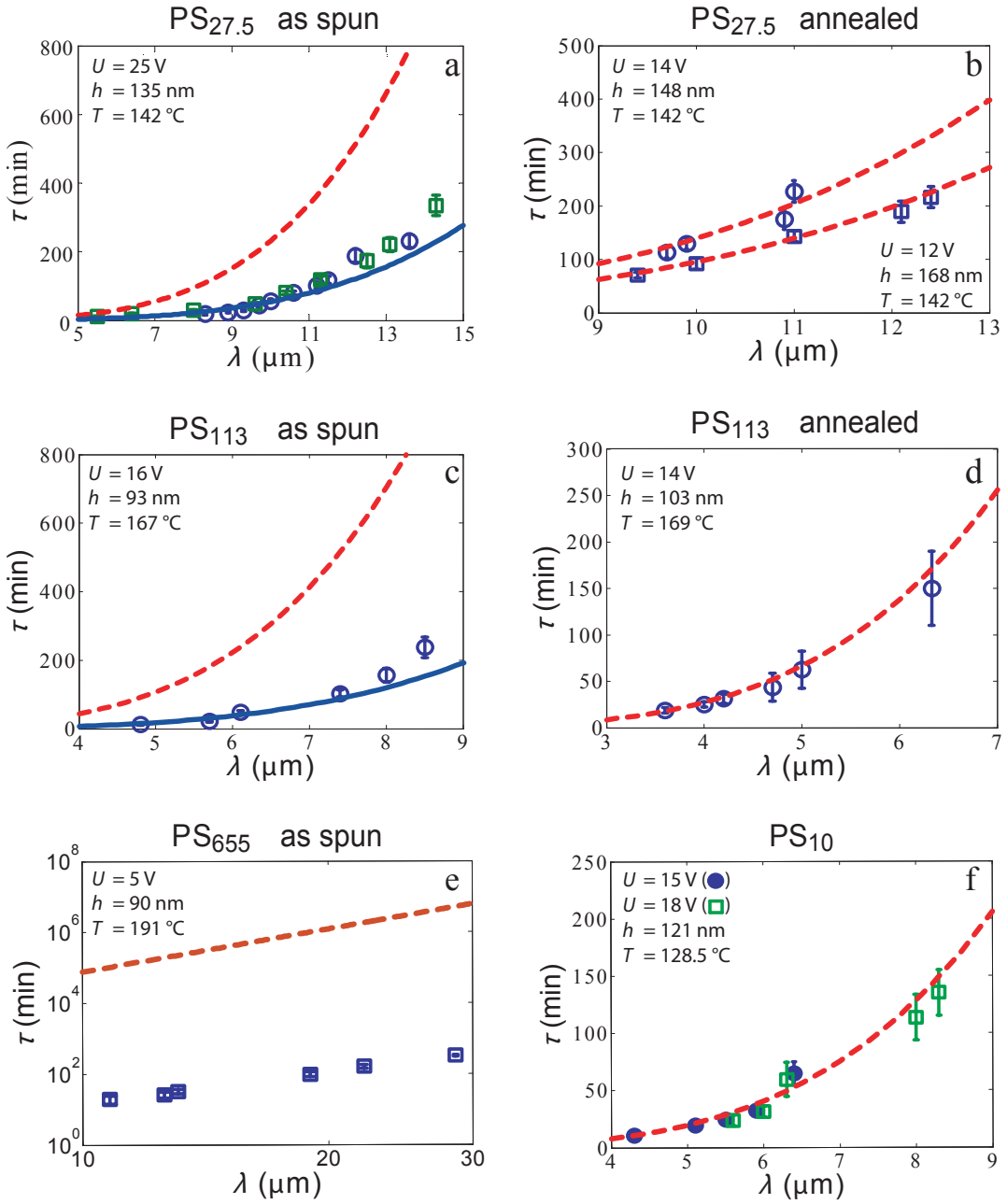

Figure 7.4: Characteristic destabilization time τ as a function of instability wavelength λ for 4 polymer molecular weights. **a**, **c** and **b**, **d** compare films before and after annealing for $PS_{27.5}$ and PS_{113}, respectively. The circles and squares in **a** correspond to films on bare silicon wafers and surfaces covered by a self-assmbeled monolayer, respectively. The squares and circles in **b** correspond to two samples of different thicknesses. The squares and circles in **f** correspond to annealed and as-cast samples, respectively. The dashed lines are predictions of equation 7.1 using the bulk viscosity, the solid lines are fits of equation 7.1 to the data by variation of η (Table 7.2). The error of measurement of λ is $\sim$10% (not shown on the graphs)

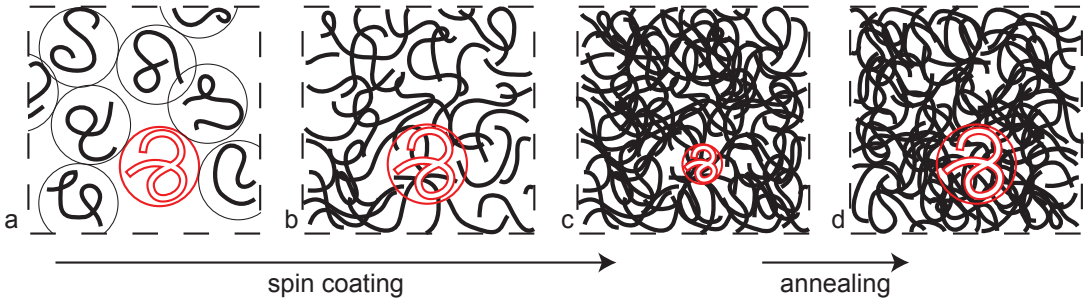

Figure 7.5: Model for the reduction in effective viscosity in spin-cast films. (a) Starting from a semi-dilute solution, (b) the chains start to entangle as the concentration increases. (c) The slow-down and collapse of the chains for high polymer concentrations prevents the full equilibration of the chains. Thermal annealing for times longer than the reptation time equilibrates the chains, restoring the melt entanglement density and viscosity (d).

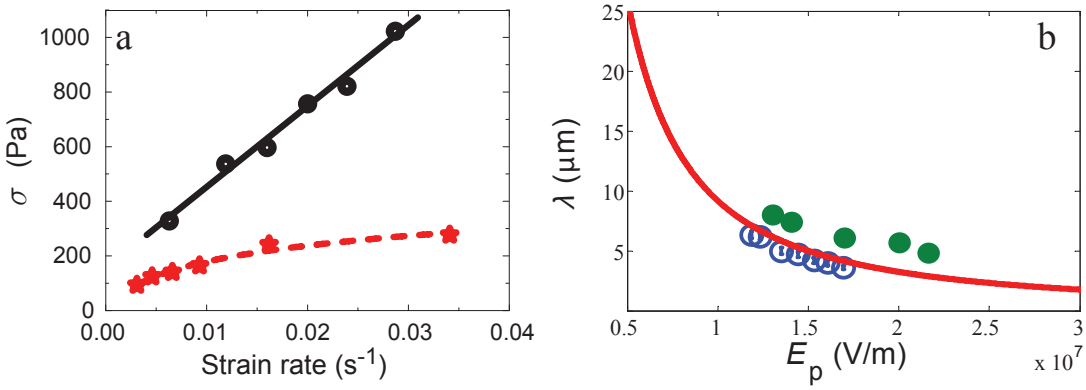

Figure 7.6: Strain rate and EHD wavelength. (a) Strain rate in as-cast(stars, dashed line) and annealed (circles, full line) PS_{113} films as a function of shear stress induced by the film destabilization (see text). (b) Characteristic wavelength as a function of the electric field strength in the film, E_p, for PS_{113}. The full and open circles correspond to the as-cast and annealed films, respectively.

electric field and the Laplace pressure, with $p(h) = -0.5\varepsilon_0\varepsilon_p(\varepsilon_p - 1)(E_p)^2$.[2] The relative thickness change due to this pressure difference is $2\Delta h = h_{max} - h_{min}$ over a lateral distance $\lambda/2$, where h_{max} and h_{min} are the height of the maxima and minima. The time it takes for the undulation to reach this change in thickness defines the strain rate in the early stages of the destabilization process. The linear stress-strain relation extracted from the data in Fig. 7.4 d for the annealed PS_{113} films is characteristic for a Newtonian liquid with a viscosity of $\eta = 29$ kPa s, in good agreement with the literature value (Table 7.2). The data of Fig. 7.4c, for the as-cast film, on the other hand, shows a non-linear stress-strain variation with a much smaller slope. In this representation, high shear rates correspond to small values of τ, while long destabilisation times give rise to low shear rates. The lowest value of the slope at high shear rates correspond to the much lowered effective viscosity of the data in Fig. 7.4c for small values of τ (high destabilizing fields). The increase in slope (i.e. increase in viscosity) with decreasing shear rate (i.e. low fields and high values of τ) is indicative of an increase in relaxation of the quenched polymer chains, giving rise to increasing values of the effective viscosity. The two curves approach each other in the limit of very low strain rates (i.e. sufficiently large values of τ).

7.5.3 Reduction in Entanglement Density

The connection between the reduction in entanglement density of the chains in the as-cast films and their lowered viscosity can be quantified in terms of the reptation model [101], $\eta = \eta_0(M_w/M_e)^\nu$ with the intrinsic viscosity of the unentangled melt η_0. Comparing two polymer melts with the same chain length but different degrees of entanglement, M_e and M_e', can therefore be described

[2] $E_p = \varepsilon_i U/[(1-\varepsilon_i)\varepsilon_p h_i + \varepsilon_p\varepsilon_i d - (\varepsilon_p - 1)\varepsilon_i h]$, where ε_i and h_i are, respectively, the dielectric constant and the thickness of the insulating layer on the semi-transparent electrode.

by the relation $M_e'/M_e = (\eta'/\eta)^{-k}$, with $k = 1/(\nu - 1)$. Using the commonly accepted values of $\nu = 3.4$ and $M_e \approx 17\,\mathrm{kg/mol}$ for PS, an increase in M_e' to $\approx 29\,\mathrm{kg/mol}$ and $\approx 36\,\mathrm{kg/mol}$ account for the effective viscosity decrease in the $PS_{27.5}$ and PS_{113} films, respectively.

While the viscosity reduction in our experiments are likely to arise from a reduced entanglement density, annealing times significantly exceeding the reptation time were needed to recover bulk rheology in the thin films. In particular, destabilisation time of PS_{655} films were significantly below the predictions of equation 7.1, assuming bulk viscosity. This indicates that the thermal equilibration of very high M_w films by thermal annealing cannot be achieved in technologically practical times. Despite the high film thickness, the quenched polymer chains seem to equilibrate substantially more slowly than predicted by the reptation model. A very slow relaxation process in relatively thick films has also been observed by Bodiguel *et al.* [95] and Kanaya *et al.* [102], requiring annealing times significantly exceeding the reptation time to recover equilibrium bulk rheology, but remain unexplained. This surprising behaviour was also reported for the relaxation of sheared semi-dilute polybutadiene solutions [103] and the equilibration of PS latex spheres in a PS melt [104].

Results indicate that the spin-cast chains have quenched conformations that cannot be equilibrated by a standard reptation process. The Edwards reptation time is the characteristic time for tube renewal of a Gaussian coil in an equilibrated melt. Quenched chains may, however, be far from this equilibrium conformation, and their equilibration may be kinetically hindered. In particular, chains that have internal entanglements (knots) may have relaxation times much above the Edwards reptation time [105]. While the detailed entanglement dynamic of chains during spin-coating is presently unknown, our experiments indicate that coil structures far from equilibrium are formed, which equilibrate

much slower than predicted by the reptation theory.

7.5.4 In-Plane Stresses

A further aspect of non-equilibrium chain formation are frozen-in in-plane stresses. Such stresses were found in much thicker films [99] and in dewetting experiments [106]. A recent theoretical study predicts that in-plane stresses in thin films can drive a film instability on a slippery substrate [107]. In our experiments the presence of in-plane stored tensile stresses in the as-cast films are therefore expected to act as an additional driving force. Compared to the annealed, stress-free films this should result in a film instability with smaller values of λ in the as-cast film. Figure 7.6 b compares the experimentally determined instability wavelength of as-cast and annealed films as a function of the electric field in the polymer E_{p}. While the data for the annealed films is well described by the prediction of the linear stability analysis (line), the values of λ are systematically *larger* in the as-cast film. This is indicative of a stabilizing pressure acting on the as cast films, ruling out the effects of homogeneous in plane stresses predicted by Vilmin *et al* [107]. Since longer wavelengths also imply increased values of τ, the measured viscosity reduction can not arise from frozen-in in-plane stresses. The origin of this small stabilizing effect in as-cast films of Fig. 7.6 b remains unclear. The same stabilizing effect was also observed in experiments performed with $PS_{27.5}$. Possible explanations include frozen-in normal stresses arising either from strong solvent gradients during spin-coating which lead a variation of the entanglement density normal to the film surface, or from polymer adsorption at the substrate, giving rise to non-equilibrium chain conformations at that surface.

7.5.5 Conclusion

In conclusion, we have used an electric field technique to weakly perturb the surface of $\sim 100\,\mathrm{nm}$ thick PS films. We find that as-cast films of sufficiently high molecular weight exhibit a faster than expected mobility. Annealing the films for times much longer than the polymer reptation time reduces the film mobility to the value expected from the bulk rheology. The viscosity of annealed thin-film polystyrene melts was measured by two different methods using electric fields (measure of τ vs. λ, and measure of stress vs. strain rate) and was found to be in good agreement with the bulk value of polystyrene measured with a parallel plate rheometer. The mobility increase found in the as-cast films is explained in terms of non-equilibrium conformations of the chains caused by the rapid solvent evaporation during spin-coating. This process results in a lowered entanglement density and therefore in a reduced effective viscosity. The reentanglement of the chains by annealing was found to be substantially longer than the reptation time, indicating trapped chain conformations in relatively thick films. The experiments show no evidence of destabilising in-plane stresses. Rather, an unexpected weak stabilisation of the as-cast films was found, an effect which is currently under investigation. The substantial change in viscosity in polymer films compared to their bulk rheology is likely to significantly influence film processing, not only for spin-cast films but also for other film deposition techniques, which involve rapid solvent extraction.

	M_w (kg/mol)[1]	Fig. 7.4	η (kPa . s)[1]	T_{ann} (°C)	t_{ann} (h)
$PS_{27.5}$	27.5	a	2.2[2]	-	-
$PS_{27.5}$ annealed	27.5	b	10.6[3]	145	~ 22
PS_{113}	113	c	5.5[2]	-	-
PS_{113} annealed	113	d	32.3[4]	155	145
PS_{655}	655	e	0.2[2,5]	-	-
PS_{10}	10	f dots	13[3]	-	-
PS_{10} annealed	10	f squares	13[3]	120	40

Table 7.2: Experimental parameters of the data shown in Fig. 7.4. [1]At the temperature given in Fig. 7.4; [2]fit to data of Fig. 7.4; [3]measured; [4]from [97,98]; [5]bulk viscosity: 1.3 MPa s calculated from [97,98].

.

Chapter 8

Growth of EHD Instabilities

This Chapter introduces an experimental method to measure in real time the growth of micron-size instabilities in a film with a sub-nanometer resolution [108]. The growth rate of instabilities in the film gives a measure of the film's viscosity which confirms our previous results of an increased chain mobility in spin-cast films (see Chapter 7).

8.1 Multiple Beam Interferometry (MBI)

8.1.1 Interferences with Multiple Beams

In Chapter 5, we ignored multiple reflections inside the cavity, and approximated our interferometer to a three beams system. However, when the interfaces are highly reflective, a large number of mutually coherent beams can be produced, and much higher intensities can be achieved [109]. While the optical method described in Chapter 5 is well suited to the measurement of small amplitude fluctuations, it cannot be used to measure the growth of large instabilities due to the complex nature of the interference pattern resulting from three beams for large thickness variations. Instead, a multiple beam interferometric method was

used to measure growth rates with a high resolution.

The most common way to produce highly reflective surfaces is to evaporate a thin-film of reflective material (e.g. Ag) on top of a glass slide, or another transparent substrate, to create a semi-transparent mirror (see Chapter 6). In the case of two nearly parallel partially reflective surfaces (1 and 3 in Fig. 8.1), the incoming plane wave is split into two plane polarized beams at the first reflective interface: a reflected beam and a transmitted one. The transmitted beam is then once more split into a transmitted part, and a reflected part which eventually undergoes multiple reflections inside the cavity formed by the two reflecting surfaces. With sufficiently reflective surfaces, a large number of beams (>50) can be reflected inside the cavity and retransmitted through the first interface before they are collected by a lens or a microscope objective to recombine and form an interference pattern [109].

After one reflection off interface 3, beam 2 is out of phase compared to beam 1 by:

$$\delta = \frac{4\pi}{\lambda_0}\left((n_f h + (d-h))\cos\theta'\right) + \pi. \tag{8.1}$$

where n_f is the index of refraction of the film, λ_0 the wavelength of light in vacuum, and θ' the angle made by the first transmitted beam with respect to the normal of interface 1. Because of the geometry of our experiment, we can assume a normal angle of incidence, and $\cos\theta' = 1$. After p reflections off the first interface, the phase difference between the first and p^{th} beams can be approximated to $p \times \delta$. Since the plates are not perfectly parallel, the exact phase difference with the first beam after p reflections is $\delta_p = \frac{2p}{3}\frac{2\pi}{\lambda_0}\left(3 + (2p^2+1)\alpha^2\right)d$, where α is the wedge angle. For our system, small wedge angles of $\sim 10^{-4} - 5 \cdot 10^{-4}$ rad can be achieved, which for the larger wedge leads to a phase lag ($\frac{2p}{3}\frac{2\pi}{\lambda_0}\left(2p^2+1\right)\alpha^2 d$) of less than 8 % after 50 reflections (in the case of two

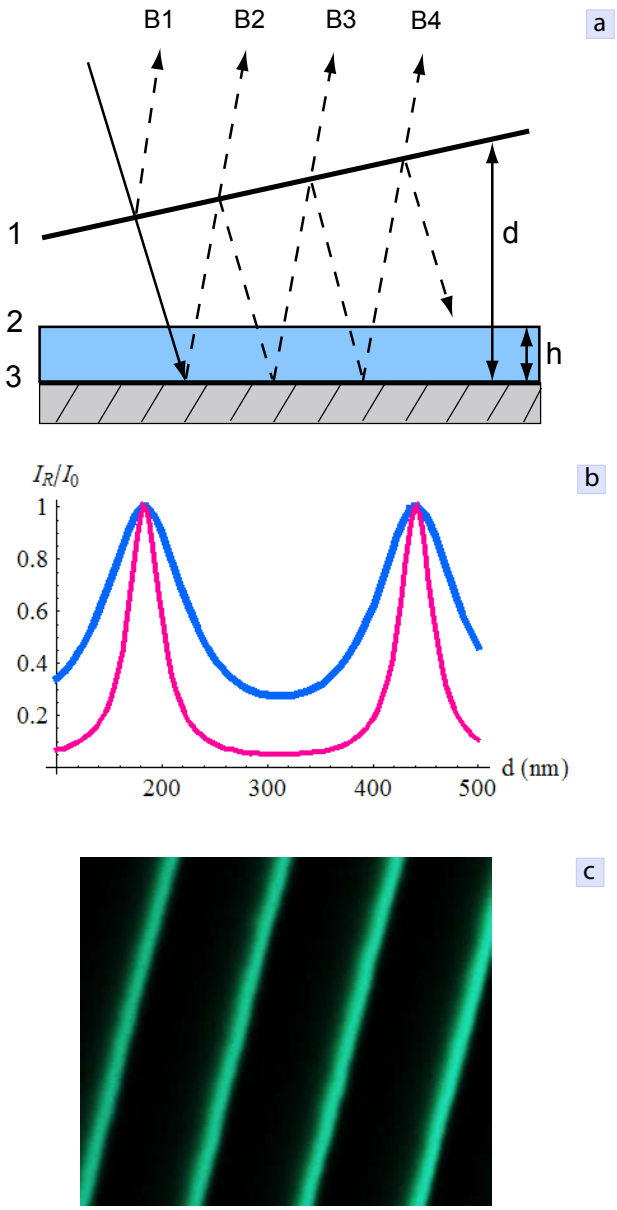

Figure 8.1: (a) Schematic of light interferometry with interfaces of high reflectivity. A large number of beams can be reflected off silvered surfaces. (b) Ratio of reflected to incident irradiance for multiply interfering beams as a function of the gap d. The modulation of the irradiance shows sharper fringes for two highly reflecting interfaces ($R = 0.9$, thin red curve) than for weakly reflecting ones ($R = 0.5$, thick blue curve). The contrast between bright and dark fringes is also better in the case of highly reflecting interfaces (Fig. 5.4). The calculation is done for $\lambda_0 = 515\,\text{nm}$. (c) Image of typical MBI fringes obtained with our setup (Fig. 8.3) and with monochromatic light (515 nm), showing high contrast and sharp fringes. Image width is $900\,\mu\text{m}$.

highly reflective interfaces with $R > 0.9$) compared to a geometry with parallel plates [109]. Because our first interface is only semi-reflective (see Chapter 6), the number of reflected beams will be lower and the phase change even smaller. If we assume that $p = 20$ beams are reflected inside the cavity, the phase lag would reduce to a negligeable 0.5%. We can also calculate the thickness d needed to produce destructive interferences and decrease the sharpness of the fringes in the interferometer. This condition is given by: $\frac{2p}{3}\left(2p^2+1\right)\alpha^2 d = \frac{\lambda_0}{2}$. A distance $d > 6\,\mu$m would be needed between the electrodes to produce destructive interferences with highly reflective interfaces ($p = 50$) and a typical wedge angle of $5{\cdot}10^{-4}$ rad. With less reflective interfaces, the maximum value of d rapidly increases ($\propto p^{-3}$), and for $p = 20$ we have $d \sim 100\,\mu$m. Since the gaps we use are at least two orders of magnitude less than that, the intensity summation of a large number of reflected beams is not affected in our configuration. The sum of the amplitudes resulting from the interference of the multiply reflected beams is therefore given by:

$$\begin{aligned} E_r \;=\; & E_0(r_1 \\ & + r_3{}'(t_1 \cdot t_1{}') \cdot (t_2 \cdot t_2{}')e^{i\delta} \\ & + r_1{}' \cdot (r_3{}' \cdot (t_2 \cdot t_2{}'))^2 \cdot t_1 \cdot t_1{}' \cdot e^{2i\delta} \\ & + (r_1{}')^2 \cdot (r_3{}' \cdot (t_2 \cdot t_2{}'))^3 \cdot t_1 \cdot t_1{}' \cdot e^{3i\delta} + \ldots)) \end{aligned} \tag{8.2}$$

where r_1 and r_3 are the Fresnel reflection coefficients at the outer interface (medium 1/Ag) of surface 1, and at the inner interface 3 (film/Ag) respectively. Similarly, t_1 and t_1' are the transmission coefficients at the first interface, and t_2 and t_2' at the second (film/air) interface. The same applies to the reflection coefficients r_1 and r_1', and, if we assume no absorption, we have the following relations between t_i, t_i', r_i and r_i':

$$r_i = -{r_i}'$$

$${r_i}^2 = {r_i}'^2 = R_i$$

$$t_i \cdot {t_i}' = T_i$$

with R and T being the reflectivity and transmissivity, respectively.

The total reflected amplitude can be rewritten as:

$$\begin{aligned} E_r &= E_0 \left(r_1 + r_3' \cdot T_1 \cdot T_2 \cdot e^{i\delta} \left(1 + r_1' \cdot r_3' \cdot T_2 \cdot e^{i\delta} + \left(r_1' \cdot r_3' \cdot T_2 \right)^2 \cdot e^{2i\delta} + \ldots \right) \right) \\ &= E_0 \left(r_1 + r_3' \cdot T_1 \cdot T_2 \cdot e^{i\delta} \left(\sum_{n=0}^{\infty} \left(r_1' \cdot r_3' \cdot T_2 \right)^n \cdot e^{ni\delta} \right) \right) \end{aligned} \tag{8.3}$$

where the geometric sum $\sum_{n=0}^{\infty} \left(r_1' \cdot r_3' \cdot T_2 \right)^n \cdot e^{ni\delta}$ can be simplified as:

$$\sum_{n=0}^{\infty} \left(r_1' \cdot r_3' \cdot T_2 \right)^n e^{ni\delta} = \frac{1 - \left(r_1' \cdot r_3' \cdot T_2 \right)^n \cdot e^{ni\delta}}{1 - \left(r_1' \cdot r_3' \cdot T_2 \right) \cdot e^{i\delta}}. \tag{8.4}$$

In the limit of an infinite number of beams, the term $\left(r_1' \cdot r_3' \cdot T_2 \right)^n e^{ni\delta}$ vanishes, and the amplitude of the reflected beams becomes:

$$\begin{aligned} E_r &= E_0 \left(r_1 + r_3' \cdot t_1 \cdot t_1' \frac{1}{1 - \left(r_1' \cdot r_3' \cdot T_2 \right) e^{i\delta}} \right) \\ &= E_0 \left(\frac{r_1 + r_3' \cdot T_2 \cdot e^{i\delta} \left(R_1 + T_1 \right)}{1 - r_1' \cdot r_3' \cdot T_2 \cdot e^{i\delta}} \right) \\ &= E_0 \left(\frac{r_1 + r_3' \cdot T_2 \cdot e^{i\delta}}{1 + r_1' \cdot r_3 \cdot T_2 \cdot e^{i\delta}} \right). \end{aligned} \tag{8.5}$$

The last step in expression 8.5 was done by writing $\left(R_1 + T_1 \right) = 1$. The intensity of the reflected light is the product of the reflected amplitude E_r and its conjugate E_r^*[1]:

[1]The intensity of the reflected light is also often referred to as the reflectivity R, and it can simply be written as the square of the absolute value of the complex wave E_r: $I_r = R = |E_r|^2$.

$$I_r = E_r \cdot E_r^*. \tag{8.6}$$

We see from Fig. 8.1 b and 8.1 c that the interference of multiple beams gives rise to sharp fringes and relatively high intensities with monochromatic light. This provides good sensitivity to small surface details, and images with a high contrast.

8.1.2 Measurement of Thickness Variations with MBI

The measurement of surface instabilities can also be performed with surfaces coated with Ag to increase the number of reflected beams. In this case precautions should be taken to avoid tarnishing or degradation of the silver layer during the EHD experiments. Ideally, a thin layer of silicon oxide was e-beam evaporated onto the Ag surface to protect it. The deposition was performed in a ultra-high vacuum chamber at $\sim 10^{-8}$ Torr and at very low deposition rates ($\sim 0.2\,\mathrm{nm\ s^{-1}}$). Analysis of the surface by AFM before and after an experiment showed that the roughness was similar, and visual observation confirmed that the surface reflectivity was still very high. By contrast, if no protective layer was used, the Ag would quickly degrade when heated at temperatures above 100 °C and lose its reflectivity. An alternative method was also used when deposition of silicon oxide was not possible, which consisted of a thin layer of SU-8 spin-coated onto the semi-transparent silvered electrode.

Typically, multiple beam interferometry is used to measure surface irregularities between two highly reflecting surfaces. Usually, the lateral size of these irregularities is larger than the actual width of the fringes, and determination of thickness variations is done by measuring the lateral shift of a complete fringe Δx (see Fig. 8.2). In our case, the surface instabilities created by the electric

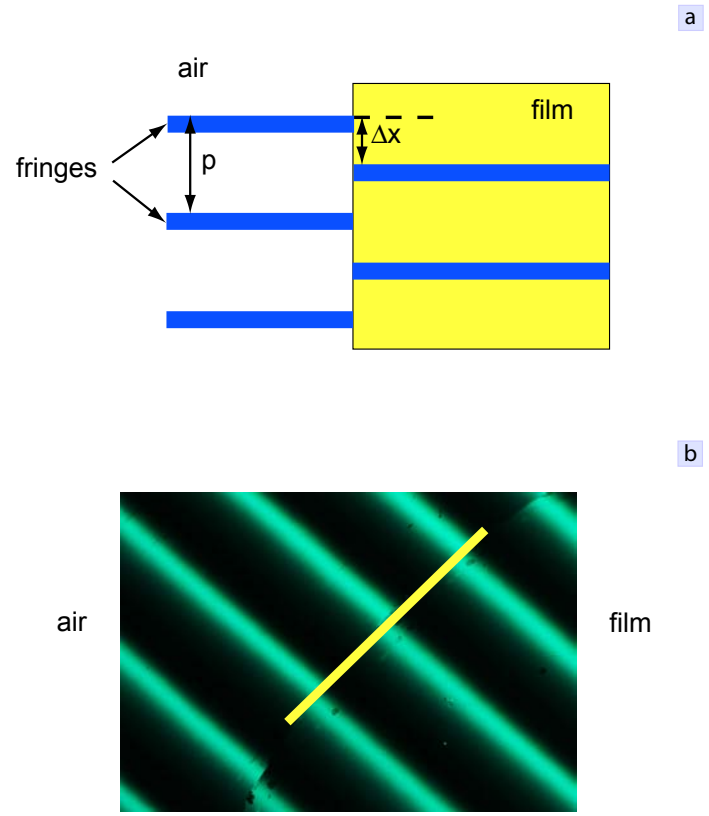

Figure 8.2: Principle of a thickness measurement by MBI. Figure (a) shows the fringe displacement Δx occurring inside the cavity when the fringes pass on a film of thickness h. (b) is an image of the fringes shift between a silvered surface (left) and area covered by a thin polystyrene film (right). The straight line delineates the edge of the film. Image taken at $\lambda_0 = 515\,\mathrm{nm}$.

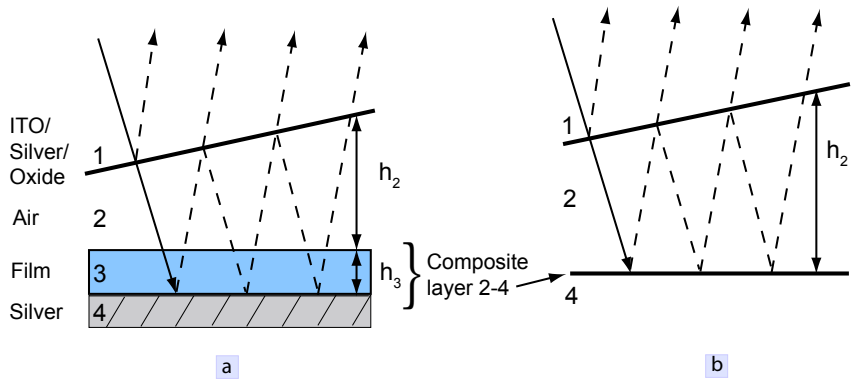

Figure 8.3: Schematic of the optical cavity with a partially silvered interface (1) and a fully reflecting silver layer (4). (a) shows the various layers composing the interferometer, whereas (b) is a reduced system showing the composite layer (2-4) with the reflectivity r_{24} used in the calculations.

field are smaller than the fringe width, and this method cannot be used. Instead, we measured the local shift in intensity when an instability developed, and calculated the corresponding phase shift to determine the thickness change. We also experimentally verified that the intensity profile and the period of the fringes stay the same when the thickness of the film is changed by measuring the fringe profile of PS films of various thicknesses. This means that a change in film thickness can be measured from the corresponding shift in the intensity profile of the fringe.

Following an analysis by Gottling to measure double layer thickness variations [110], Figure 8.3 shows the reduced schematic of our interferometric system with the various layers considered. The relationship between the phase shift in the film and its thickness is done by writing the composite reflection coefficient r_{24} (derived from Eq. 8.5 with $T_2 = 1$, and the phase change inside the dielectric film 3 is $\Phi_3 = \frac{4\pi}{\lambda_0}(n_3 h_3)$ for the layered system (air/film/Ag, or 2/3/4), and the

phase shift upon reflection at the Ag layer is Φ_{34} [110, 111]:

$$r_{24} = \frac{r_{23} + r_{34}e^{i(\Phi_{34}+\Phi_3)}}{1 + r_{23} \cdot r_{34}e^{i(\Phi_{34}+\Phi_3)}}, \tag{8.7}$$

where r_{23} and r_{34} are the Fresnel reflection coefficients at interfaces 2/3 and 3/4 respectively [2].

The phase shifts $\Delta\Phi_3$ and $\Delta\Phi_2$ corresponding respectively to a change in the film thickness δh_3 and a change in the air gap δh_2 are expressed by:

$$\Delta\Phi_3 = \frac{4\pi}{\lambda_0}(n_3\Delta h_3) \tag{8.9}$$

$$\Delta\Phi_2 = \frac{4\pi}{\lambda_0}(\Delta h_2)\,. \tag{8.10}$$

Since we are only concerned with relative phase changes that originate from a film thickness variation inside the composite layer air/film/Ag, the details of the reflection at the first semi-transparent electrode (interface 1 in Fig. 8.3) need not be known accurately.

The phase shift occurring upon multiple reflections inside the composite layer 2-4 is related to the film thickness h_3 through the argument of the complex coefficient r_{24}. To maintain a constant order of interference, the phase shift in the air layer $\Delta\Phi_2$ must be equal to the change in argument of r_{24} ($\Delta\mathrm{Arg}(r_{24}) = \arctan r_{24}$) which occurs inside the composite film layer. The total phase change in the air layer must then equal the local phase shift $\Delta\phi_{\mathrm{shift}}$ which is measured

[2]The reflection coefficient r_{23} is real, whereas r_{34} is a complex number:

$$r_{34} = \frac{n_3 - (n_4 + ik_4)}{n_3 + (n_4 + ik_4)} = \rho_{34}e^{i\Phi_{34}} \tag{8.8}$$

where n_3 and n_4 is the real parts of the index of refraction of materials 3 and 4 respectively, and ik_4 is the imaginary part of material 4 (see Table 5.1). Because the Ag layer is highly reflective, the coefficient $\rho_{34} \sim 1$ and the reflection coefficient at the film/Ag interface can be written: $r_{34} = e^{i\Phi_{34}}$

from the change in intensity of the fringe pattern when the thickness of the film varies. This condition is written:

$$\Delta \mathrm{Arg}(r_{24}) + \frac{\Delta \Phi_3}{n_3} = \Delta \phi_{\mathrm{shift}}. \tag{8.11}$$

Fig. 8.5 illustrates the principle of the measure of $\Delta\phi_{\mathrm{shift}}$. A change in film thickness Δh_3 shifts the phase of the interference pattern to a value which corresponds to the phase of the unperturbed film a distance Δx away from point A. Because the intensity profiles of the fringes as a function of d or as a function of Δh_3 follow the same pattern and go through the same values of maxima and minima (see Fig. 8.4), the distance Δx between the local instability of intensity I and the corresponding point of same intensity in the fringe pattern can be used to measure the phase shift $\Delta\phi_{\mathrm{shift}}$:

$$\Delta \phi_{\mathrm{shift}} = \frac{2\pi \Delta x}{p}, \tag{8.12}$$

where p is the period between fringes. The change in thickness of the air layer is:

$$-\Delta h_2 - \Delta h_3 = \left(\frac{\Delta x}{p}\right)\left(\frac{\lambda_0}{2}\right). \tag{8.13}$$

Equation 8.11 can therefore be rewritten:

$$-\Delta \mathrm{Arg}(r_{24}) - \frac{4\pi}{\lambda_0}\left(\Delta h_3\right) = \frac{2\pi \Delta x}{p}. \tag{8.14}$$

By convention Δx should be positive when it is in the direction of increasing gap. Since $(-\Delta h_2 - \Delta h_3)$ is negative when the film thickness increases, Δx is also negative. This corresponds to a decrease in the total gap thickness in order to maintain a constant order of interference.

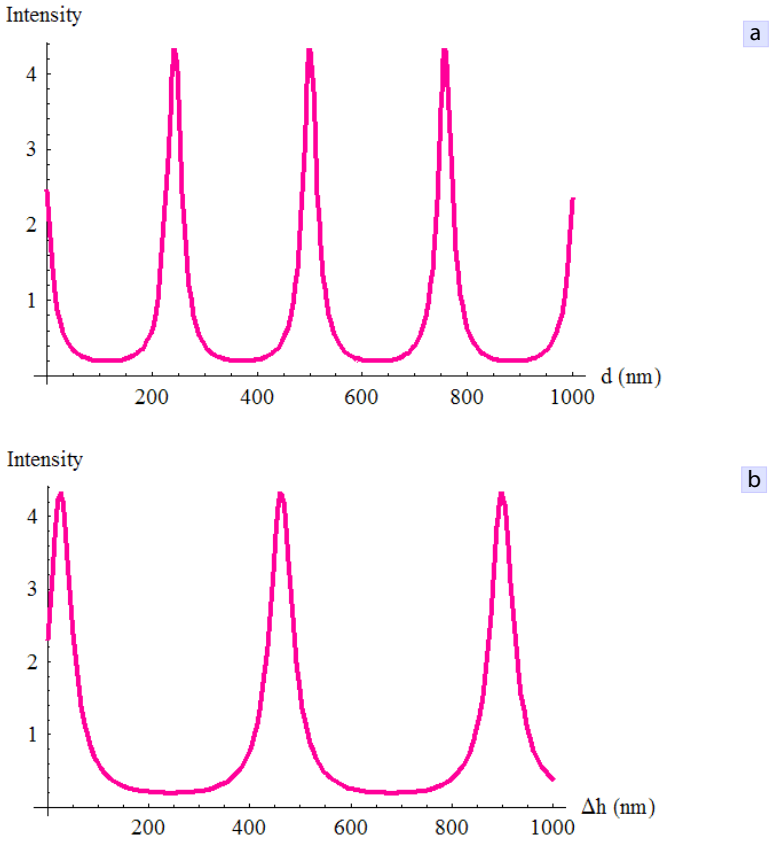

Figure 8.4: Calculation of the intensity variation due to the change in optical thickness inside the interferometer for the system of interfaces used in our experiments (see Fig. 5.4). (a) Intensity variation as a function of the gap d for a fixed film thickness. (b) Intensity variation as a function of the film thickness Δh_3 for a fixed gad d of 500 nm. The calculation is done for $\lambda_0 = 515\,\text{nm}$.

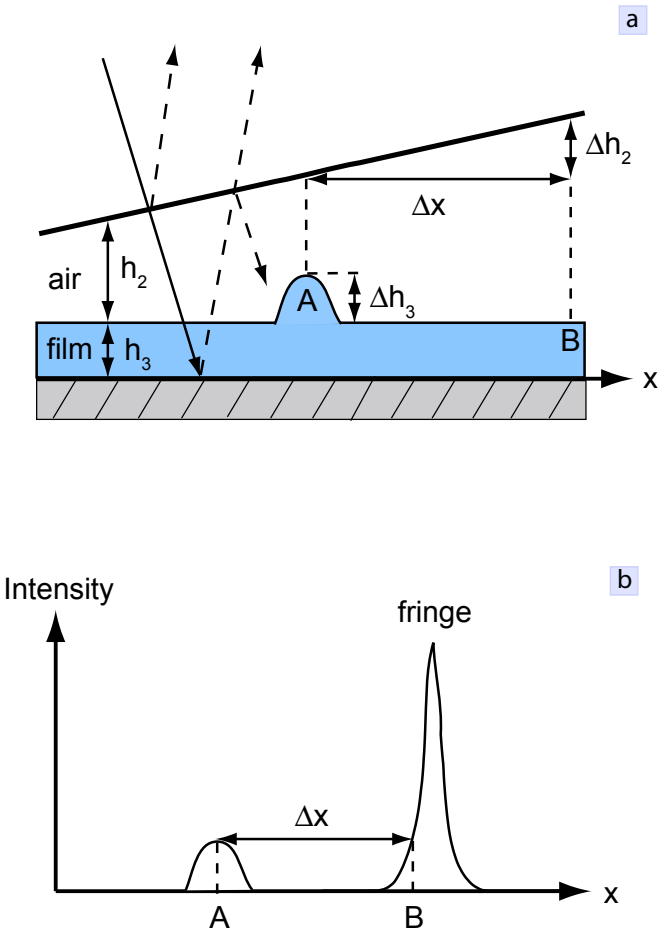

Figure 8.5: Measure of the phase shift due to a local change in thickness in the thin film. (a) Schematic of the interferometer showing the distance Δx by which the intensity of the interference pattern is shifted when an instability of height Δh_3 grows in the film. For clarity, the recessed rim around the instability is not shown in the figure. (b) Intensity variation along the film in the direction x of increasing air gap. The local change in thickness at A shifts the intensity to the same value as in B. The lateral shift in the fringe pattern which occurs at A is measured by matching the intensity of the fringe in B to that of A.

8.2 Results

8.2.1 Thickness of Thin Polystyrene Films by MBI

We tested this method on thin PS films of various thicknesses deposited on a highly reflective electrode (Si/Ag), and measured the fringe shift with the bare substrate to determine the film thickness (see Fig. 8.2). We also measured the maxima and minima of the reflected intensity as a function of the film thickness of polystyrene samples from fits to the raw intensity data on silvered silicon substrates, and found little change (<5%) (Fig. 8.7), therefore confirming the result of the reflected intensity calculation in the interferometer (Fig. 8.4). The results of thickness measurements done on polystyrene films using the phase shift method (Fig. 8.8) show the good agreement between the thicknesses measured by MBI and by AFM, and therefore validate our approach.[3]

8.2.2 Growth Rate of EHD Instabilities in Thin PS Films

Figure 8.9 shows the growth of EHD instabilities at the surface of a thin polystyrene film. The bright dots, which represent the instabilities, vary in intensity as the film thickness changes with time. Equations 7.3 and 7.4 were used to measure τ from the growth of micron-size instabilities at the surface of a PS liquid film which were triggered by an electric field. The set-up used was the same as in Chapter 7 with the difference that the inner surface of each electrode was covered with a thin layer of Ag to increase their reflectivity. Using the method described in section 8.1.2, we measured the time evolution of the film thickness due to the growth of the instability (Fig. 8.10).

[3]The measure of thickness variations by the phase shift method described here cannot be applied if the surfaces 1 and 3 have low reflectivities. When the reflectivity of the film is comparable to that of these surfaces, the reflected intensity does not follow the typical squared sinusoidal variation with thickness, but becomes more complex because of the interference of

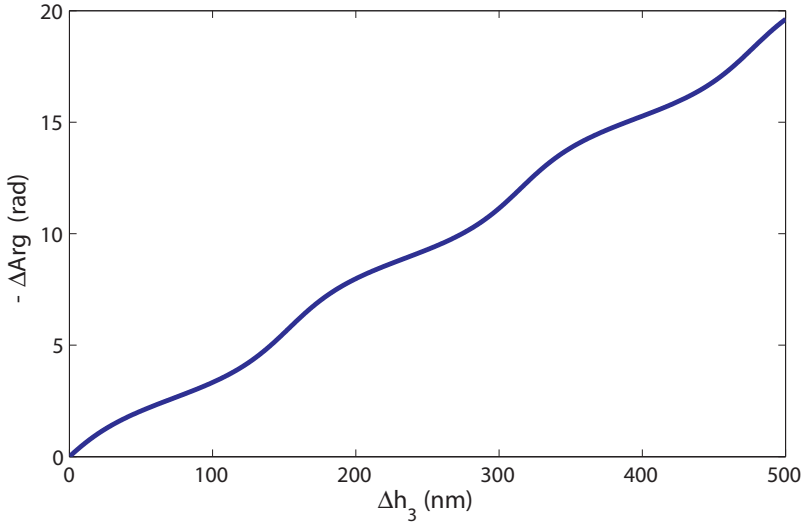

Figure 8.6: Change of phase occurring in the multilayer Ag/PS/air (see Eq. 8.11) as a function of the thickness of the PS film with a monochromatic light of $\lambda_0 = 515\,\mathrm{nm}$.

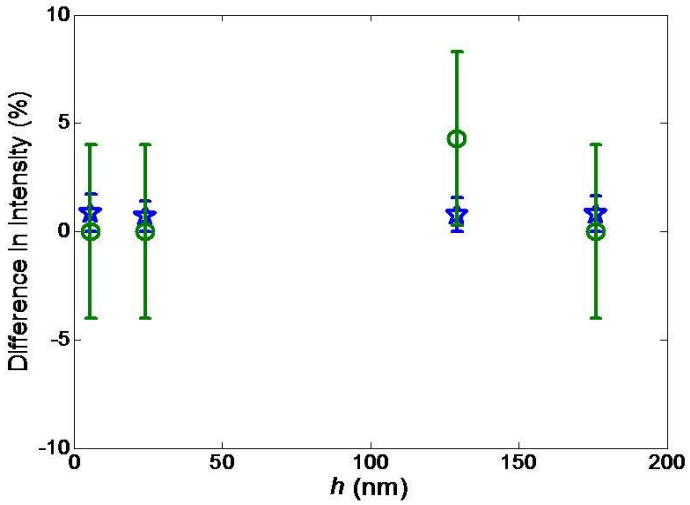

Figure 8.7: Maxima (stars) and minima (circles) in the reflected intensity of the fringes due to MBI as a function of the thickness of a polystyrene film deposited on a silvered silicon surface. The vertical axis shows the the difference in intensity between fringes on an uncoated silvered surface and fringes with a polystyrene film. $\lambda_0 = 515\,\mathrm{nm}$.

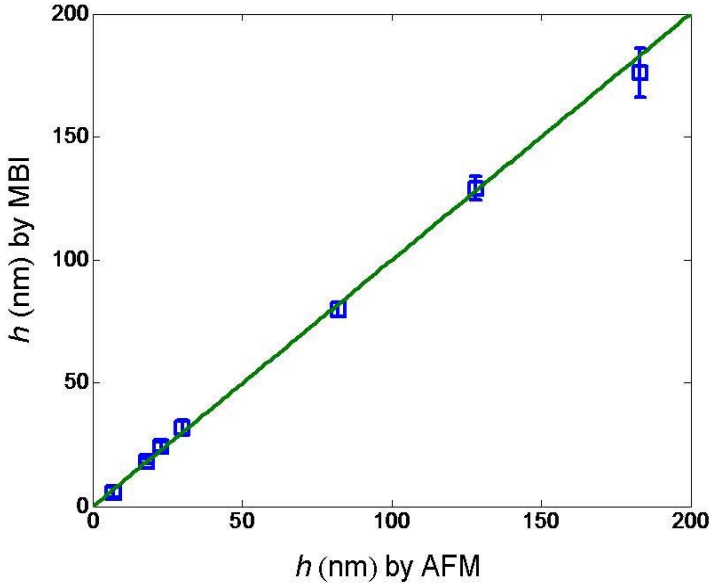

Figure 8.8: Measure of thickness variations in polystyrene thin films between ∼5 nm and 180 nm. The horizontal axis shows the height measurement performed by AFM, whereas the vertical axis is the measure done by MBI at $\lambda_0 = 515$ nm.

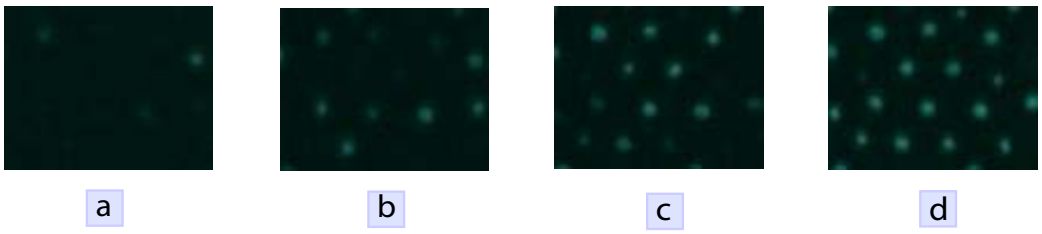

Figure 8.9: Growth of EHD instabilities on the surface of a thin polystyrene film viewed with multiple beam interference microscopy in reflection with an optical wavelength of 515 nm. Pictures (a) through (d) show the local variation in intensity as the instabilities grow with time. Images are 40 μm wide.

A Matlab program was written to perform these measurements. The program measures the intensity of an instability as a function of time, and the corresponding lateral displacement Δx from the nearest fringe to determine the phase shift (see Fig. 8.5). The change in thickness is determined using Eq. 8.14 with the measured phase shift. The growth in amplitude of the surface wave was measured as a function of time as shown in Fig. 8.10 for two PS films with different substrate/film interfacial energies. In the early stages of destabilization, the amplitude of the instability grows exponentially according to the linear stability analysis valid in the long wavelength approximation. In the linear regime, the growth rate $\beta = 1/\tau$ is therefore directly obtained from the slope of $\log(h)$ *vs.* time (see Fig. 8.10 b,d).

The results show that the thickness of the instability increases exponentially with time, and follows the prediction of the linear stability applied to shallow fluctuations (Eq. 7.3) for the early stages of destabilization. Table 8.1 shows the measurements of the growth rates of thin PS films spin-coated on two different substrates (one unmodified SiO surface, and one modified with HMDS; see Chapter 7.2.1). The early stages of the growth of the fluctuation amplitude on the unmodified substrate follow the exponential growth predicted by Eq. 7.3 up to at least $\sim$80 nm. On the HMDS modified substrate, however, the growth rate followed the linearized model up to an amplitude of $\sim$25 nm. For larger amplitudes, the growth rate increased by $\sim$50% compared to the early stages of the growth. The reason for this divergence from the model is not entirely clear, but a likely explanation is that the hydrodynamics of the liquid film are modified when the amplitude of the surface fluctuation becomes large enough to induce slip in the thin-film. One word of caution is necessary here: while the experiments on the unmodified SiO surface were repeated a number of times,

the third beam (reflected from the film surface) with the two external surfaces.

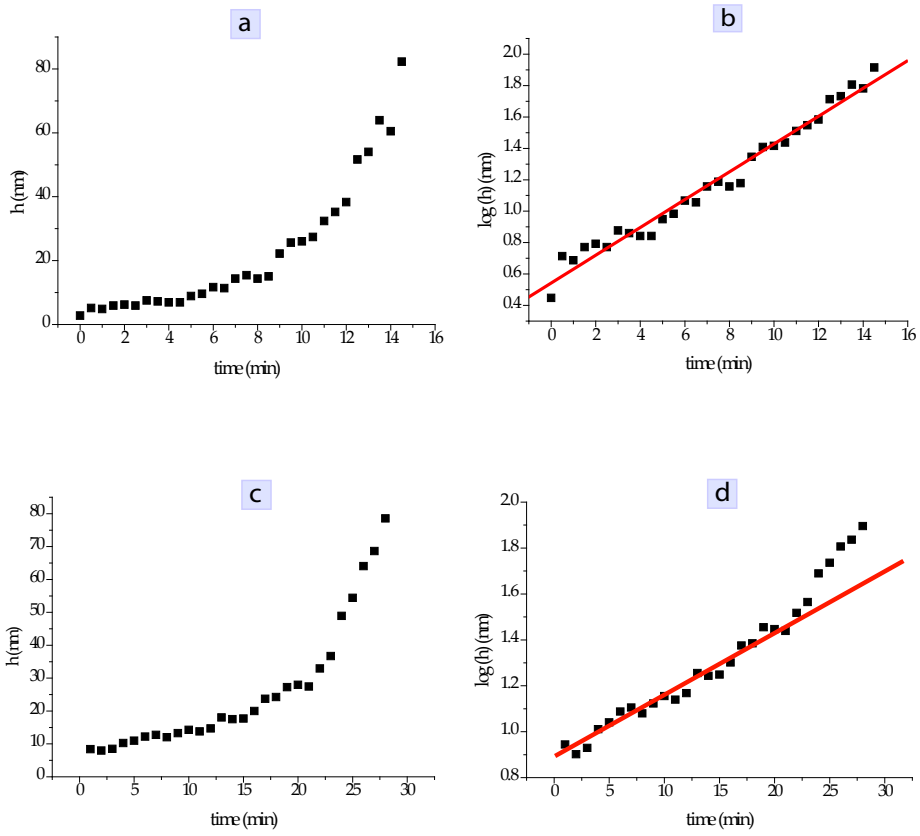

Figure 8.10: Growth rates of EHD instabilities in thin $PS_{27.5}$ films on two different substrates at 142 °C. The time $t = 0$ indicates the start of the height measurement at $t > \tau$. (a,b) Growth of EHD instability on substrate B measured by MBI. (c,d) Growth of EHD instability on substrate A measured by MBI. The log plot (d) shows the non-linear growth when the amplitude of the instability reaches ∼25 nm. The parameters of the experiment are indicated in Table 8.1.

and always showed an exponential growth like the one shown in Fig. 8.10 a,b, the experiments of the HMDS modified substrate were done on one sample only. These experiments could not be performed on more samples because of recurring technical problems with the deposition of the thin protective layer of SiO by e-beam evaporation, which prevented the following-up of these experiments. The difference in behaviour between samples A and B is however likely due to the difference in surface energy between the two substrates. Since the HMDS/PS interface has a much lower interfacial energy than the unmodified SiO/PS interface, the friction exerted by the flow of the PS melt on this surface is expected to be lower than on the unmodified surface of similar roughness (see Table 7.1). Because slip is shear-rate dependant, an increase in shear stress in the liquid layer is more likely to induce slip on the substrate with the lower surface energy (the one covered with HMDS). In the early stages of destabilization the lateral stress induced by the electric field between adjacent maxima and minima in the amplitude of the fluctuation, ΔP_{total} (see Section 7.5.2), is too low to cause slip (see Fig. 8.11).

However, when the stress (and hence the shear-rate) becomes larger with the height of the increasing instability amplitude, slip could be induced on a low energy surface. The calculation of the stress induced in the film as a function of the amplitude of the fluctuation Δh (see Fig. 8.10 c,d and Fig. 8.11 b) during the growth of the instability in sample A shows that the stress increases by more than an order of magnitude when Δh increases from $\sim$1.4 nm (corresponding to the characteristic time τ) to $\sim$25 nm (amplitude at which a non-linear behaviour is observed in sample A). This large increase in stress could possibly induce slip in the film deposited on the surface modified by HMDS (sample A). Another possible explanation concerns non-linear effects which are negligible at the early stages of the growth (when the wavelength of the instability is much larger than

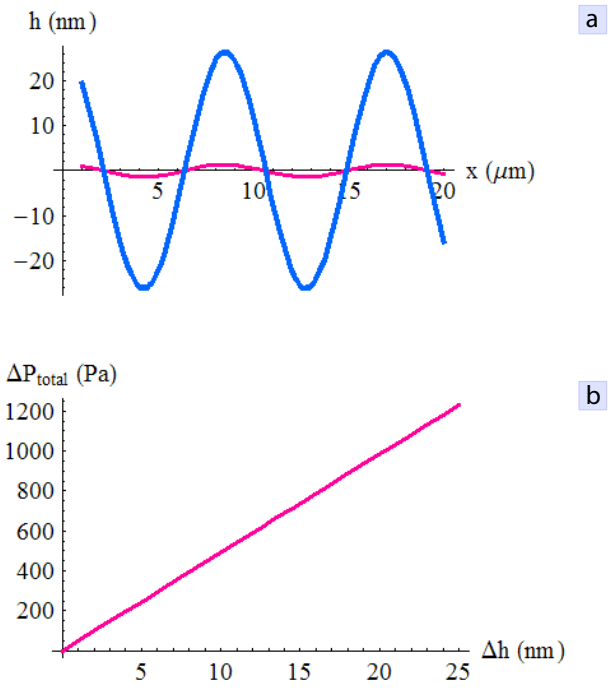

Figure 8.11: (a) Calculation of the lateral height variation in a thin film with parameters identical to that of sample A. The small amplitude fluctuation corresponds to the early stages of destabilization, whereas the large amplitude fluctuation ($\sim$25 nm) corresponds to a later time when the lateral stress ΔP_{total} has increased in the film. (b) Variation of the lateral stress induced by the sum of the electrostatic and Laplace pressures in the film as a function of the amplitude Δh of the surface fluctuation. The parameters are the same as for sample A.

Parameters	A	B
substrate	SiO/HMDS	bare SiO
h_0 (nm)	120	140
U (V)	26	24.5
λ (μm)	8.5	7.3
β	0.027	0.088
τ (min)	15.7	4.9

Table 8.1: Measurements of β and τ for EHD instabilities in thin $PS_{27.5}$ films A and B. The temperature of the experiments is 142 °C.

its amplitude), but which will contribute to the growth rate for instabilities with large enough amplitudes. However, non-linear effects seem unlikely for such shallow surface fluctuations since they are not observed on the PS-wetting SiO substrate (sample B). Moreover, it was reported that the growth of EHD instabilities in thin poly-dimethylsiloxane films followed the exponential growth predicted by the linear theory for fluctuations whose ratio of surface amplitude to characteristic wavelength ($\Delta h/\lambda$) was up to ∼1-2% [112]. From the data shown in Fig. 8.10 c and d, and from Table 8.1, a fluctuation amplitude of 25 nm for a wavelength of 8.5 μm gives a ratio ($\Delta h/\lambda$) ∼0.29%, which is much below the 1-2% measured by Leach *et al.* [112]. Therefore, the growth curves shown in Fig. 8.10 should be well within the linear model of the long wavelength approximation. We therefore believe that the increased growth rate measured on the HMDS-modified substrate is most likely due to slip at the liquid/solid interface.

The two samples were spin-coated in the same conditions, and because they have the same M_w, we can assume they have the same viscosity at the temperature of the experiment (142 °C). The results shown in Table 8.1 are for two

samples of different thicknesses h_a and h_b. The growth rate was measured for an instability of wavelength λ_a on sample A, and of wavelength λ_b on sample B. From Eq. 8.15, we see that the time constant has a strong dependance on the wavelength and the film thickness:

$$\tau = \frac{3\eta}{\gamma h_o^2 (h_o + 3b)} \left(\frac{\lambda}{2\pi}\right)^4 . \tag{8.15}$$

In the absence of slip b, the following relation gives the ratio r_τ of characteristic times τ_a and τ_b for the films A and B respectively:

$$\begin{aligned} r_\tau &= \frac{\tau_b}{\tau_a} \\ &= \left(\frac{\lambda_b}{\lambda_a}\right)^4 \left(\frac{h_a}{h_b}\right)^3 . \end{aligned} \tag{8.16}$$

The ratio r_τ shows the dependance of τ with the film thickness and the wavelength of the instability. From the data of Table 8.1, we find r_τ=0.33. Since $\beta = 1/\tau$, the ratio of the measured growth rates $r_\beta = \beta_a/\beta_b$ should be equal to r_τ. We find $r_\beta = 0.31$, which is in very good agreement with our calculation of r_τ. We also compared the values of τ measured from the growth of the instability to the values measured on $PS_{27.5}$ at 142 °C in Chapter 7 (Fig. 7.4 a). If the growth rates from Table 8.1 are corrected to the same film thickness as in Fig. 7.4 a using Eq. 8.15, we can compare the values of τ measured from Table 8.1 and from Fig. 7.4 a for the same λ. The values of the measured τ and λ are reported in Table 8.2 which shows similar time constants within the experimental error of the measurement. Therefore, we can conclude that samples A and B have a similar viscosity to the reduced viscosity measured in the spin-cast $PS_{27.5}$ films in Chapter 7 at the same temperature. This confirms the results shown in Fig. 7.4, which indicate that the viscosity of the spin-coated $PS_{27.5}$ thin films is lower

Parameters	A	B
substrate	SiO/HMDS	bare SiO
λ (μm)	8.5	7.3
τ_{MBI} (min)	10	5.5
τ_{3beams} (min)	15 $\pm$5	7 $\pm$2

Table 8.2: Comparison of measurements of τ from Table 8.2 from the growth rate of an EHD instability (τ_{MBI}), and from experiments performed in Chapter 7 (see Fig. 7.4) for $PS_{27.5}$ and $h_0 = 135\,\mathrm{nm}$ at $142\,^{\circ}\mathrm{C}$ (τ_{3beams}).

than their bulk value.

Chapter 9

Novel Robust and Flexible Molds for Nanoimprint Lithography

The motivation behind this work was to find an economical solution to the expensive, and brittle inorganic molds (or stamps) usually used in nanoimprint lithography (NIL). One challenge was to use materials which combine a number of properties desirable for stamps: flexibility and rigidity, high temperature and pressure resistance, and low-adhesive properties [8, 113]. To make these molds useful, one has to prove that they can be used for patterning on different length scales (including $\leq$100 nm). At the end of the chapter we show applications where the unique properties of these molds were used advantageously. The first application was for the manufacture of transparent patterned surfaces on thin and fragile glass slides to study insect adhesion (work in collaboration with C. Clemente and W. Federle in the Zoology department) [114]. In another application these molds were used to build an all organic stretchable laser (work in collaboration with the B. Wenger and R. Friend of the Optoelectronics group in the Cavendish) [115].

9.1 Novel Molds for NIL: Motivation

9.1.1 Nanoimprint Lithography

Nanoimprint lithography, or hot-embossing, is a method by which micro and nanostructures are reproduced into a plastic material by heating the polymer above its glass transition temperature (T_g) and applying a force to imprint, or emboss, patterns from a structured mold (Fig. 9.1). After a certain time (usually minutes), the polymer is cooled down below T_g, the applied force is released and the mold is separated from the plastic material to reveal the imprinted patterns in the polymer substrate. Relatively large areas can be imprinted (patterning of 6 in. wafers have been demonstrated previously) and features from several hundreds of μm down to less than 10 nm have been reproduced by this technique [116–118]. Nanoimprint lithography is a successful alternative to traditional optical and electron beam lithographies, and it can potentially be used for any application requiring patterning of fine structures on a surface. It has been successfully applied to build photodetectors, compact disks, magnetic disk and microfluidic channels [119–124].

9.1.2 Molds Used for NIL

The mold, or mask, in NIL is used as the tool that transfers the patterns into the embossed material. The accuracy of replication depends largely on the properties of the mold (or stamp) which needs to be mechanically, chemically, and thermally stable to resist pressures of several tens of bar at temperatures above 170 °C. Molds are often produced from silicon, fused silica (quartz) or nickel, materials in which small features can be obtained by well-established methods such as optical and e-beam lithographies, etching and electrodeposition.

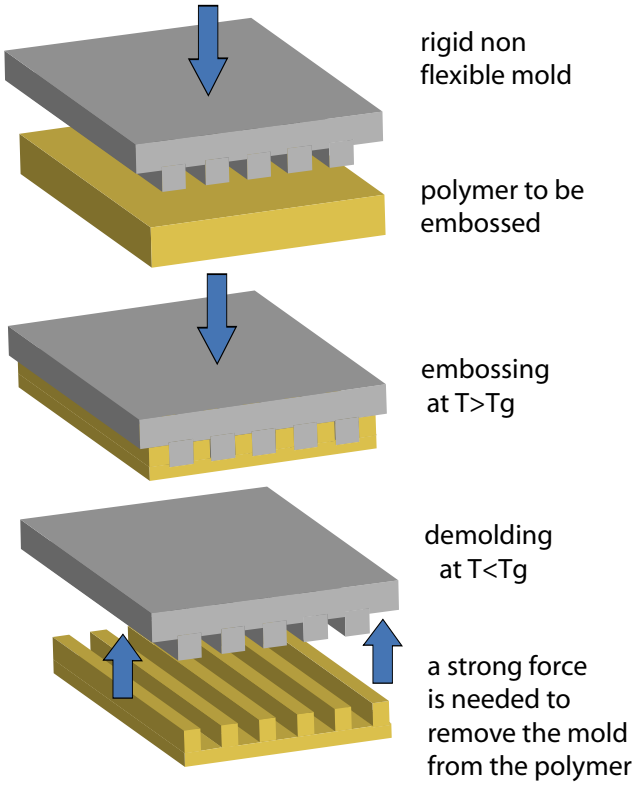

Figure 9.1: Schematic diagram of embossing using a rigid mold. The polymer and the structured rigid mold are heated above T_g while a pressure is applied to ensure flow of the polymer and to fill the cavities of the mold. Upon cooling below T_g, the entire surface of the mold in contact with the polymer must be separated at once. The relatively strong force required to remove the mold often leads to breakage of the stiff mold.

However, the manufacture of inorganic stamps requires large infrastructures and remains expensive. The need for an economical and reliable replication method is an incentive to find a replacement for silicon and other inorganic materials. Moreover, several technological applications demand ever smaller structures with a size approaching 10 nm. The mold therefore needs to provide a high accuracy of reproduction. While inorganic molds possess the mechanical stability necessary to imprint small patterns down to ∼10 nm [124] they also present a number of problems inherent to their physical properties, which limit their efficiency.

Problems with Inorganic Molds

First, because of their stiffness inorganic molds can break when a pressure is inhomogeneously applied, or due to friction when the mask is separated from the polymer. Second, relatively large pressures are usually applied to ensure conformal contact with the polymer and ensure full pattern transfer. If the mold was more flexible, a lower pressure would be sufficient to obtain conformal contact [125]. Additionally, the large difference in thermal expansion between the hard mold and the polymer can be a cause of deformation and fracture of the embossed structures during cooling and demolding, especially for large aspect ratios. Finally, an antiadhesive treatment performed onto the mold's surface is usually necessary to lower its surface energy and decrease adhesion and friction forces during demolding. However, the durability of these coatings is one factor that limits their efficiency. A fluorinated silicone coating deposited on quartz was shown to loose its anti-adhesive properties after several embossing steps as measured by the decrease in its water contact angle [126]. Both plasma deposited and ion sputtered Teflon layers have been shown to degrade during NIL [127]. Coatings obtained by silanization in the liquid or vapour phase also become less effective after a few imprints, which leads to adhesion of the polymer

to the mold. X-ray Photoelectron Spectroscopy (XPS) measurements showed a 10 at% decrease in the fluorine concentration of silanized silicon stamps (with 1H,1H,2H,2H-perfluorodecyltrichlorosilane in vapor phase) after embossing once into nylon 6,6 at 160 °C [127]. The same result was found after embossing once at 170 °C into Poly(ethylene theraphthalate) (PET). Approximately 2 at% of fluorine were detected on both PET and nylon 6,6 after embossing, whereas no fluorine was detected before embossing [128].

9.2 Flexible Molds for NIL

To reduce the problems of adhesion between the polymer and the mask, and to avoid fracture of the mask when the force is applied during imprinting, we developed a novel type of mask which is flexible and low-adhesion, and which can resist high temperatures and pressures without deforming. Stemming from an original idea of the author [129], this work was started at the Swiss Federal Institute of Technology in Lausanne (EPFL), and was continued in Cambridge. While the work in Lausanne dealt with the development of the technique to pattern micro-features with various shapes (lines, pillars, holes), the work in Cambridge focused on showing the reproducibility for patterning multiple times and in different polymers, as well as the feasibility of reproducing fine nanopatterns into a polymer substrate. The nanostructured silicon masters were made by Dr. Saifullah (who was then part of the Nanoscience center in Cambridge).

A mold made from a polymeric material that is flexible and which has a low surface energy would reduce the high production cost of inorganic stamps and solve the problems of adhesion and fracture. Because it is less rigid, a flexible mold provides a better conformal contact with the substrate during imprinting. Moreover, once cooled down, it can be released more easily than a rigid stamp

because it can be bent and gradually pealed-off from the substrate.

9.2.1 Previous Attempts to Make Flexible Molds

A mold made from a polymeric material that is flexible and which has a low surface energy would reduce the high production cost of inorganic stamps and solve the problems of adhesion and fracture. Because it is less rigid, a flexible mold provides a better conformal contact with the substrate during imprinting. Moreover, once cooled down, it can be released more easily than a rigid stamp because it can be bent and gradually separated from the substrate. To date a large number of soft and flexible molds have been used in imprinting techniques. However, their use is usually limited to imprint low viscosity polymers at room temperature and at low pressures. A slight increase in pressure results in the distortion of the mold and in the deformation of the patterns on its surface. For this reason, soft stamps suffer from a much lower resolution than that achieved by inorganic stamps in pressure assisted imprinting. Examples of materials used to make soft molds include a range of elastomeric materials such as poly(dimethylsiloxane) PDMS [130–134], an ester type UV-curable prepolymer [135], a fluorinated organic-inorganic hybrid solgel resin [136], a photocurable perfluoropolyether (PFPE) [137], and the amorphous fluoropolymer Teflon AF [138, 139]. Elastomers have a low elastic modulus ($\sim$2 to 4 MPa for PDMS) which causes them to deform when a pressure is applied. This limits the resolution of the replication process to $\sim$100 nm. Low aspect ratios (< 0.3), shallow structures and dense patterns are not stable and tend to collapse [134, 137, 140–142]. Stiffer polymers with superior mechanical properties are therefore required for a higher fidelity of pattern reproduction [143, 144]. While low viscosity UV curing polymers can be imprinted at room temperature

and at low pressure, patterning of higher viscosity thermoplastics often requires elevated temperatures and higher pressures. This is due to the fact that the resistance to flow increases with the viscosity of the polymer, and high temperature embossing provides a way to lower the viscosity. Moreover, it has been shown that the filling of the mold cavities is slowed down for high aspect ratio structures, as well as for small cavities where free flow is restricted [145]. Therefore, increasing the pressure facilitates filling of the mold cavities during NIL, and helps ensure full patterning.

9.2.2 Fluorinated Polymer Molds

Due to their high stiffness, high temperature resistance and unique anti-adhesive properties, fluorinated polymers are an obvious choice as a replacement for soft plastic molds and brittle inorganic materials. Until today, molds made of a fluoropolymer have been used only for low pressure imprinting of low viscosity photocurable polymers, and polymers mixed in a solvent at room temperature [137, 138]. Khang et al. used a highly porous Teflon AF mold to reproduce ∼80 nm patterns from a liquid solution at room temperature and at low pressure [138]. The high porosity of the mold is however not desirable for fine nanopatterning and tends to lower the mechanical stability and strength of the mold. One attempt to imprint a polystyrene (PS) film at a higher temperature was performed with a solvent cast Teflon AF mold by a low pressure NIL process [139]. This approach also showed limitations due to the fragility of the mold, with stamps less than ∼50 μm thick being prone to breakage during mold release. The mechanical properties of the mold were found to be dependent on its thickness, and imprinting with the Teflon AF mold was done only at low pressures (∼2–3 bar) with a resolution limited to ∼100 nm. In order to provide

a viable alternative to inorganic materials and to achieve high-resolution NIL with replication sizes close to 10 nm, the polymer mold needs to have a high mechanical stability and a high enough stiffness to prevent the pattern deformation or collapse encountered with soft elastomers. Good conformal contact with the surface of the substrate is also necessary to obtain a uniform and well-defined reproduction of small patterns. Sufficient pressure is therefore required to oppose the rigidity of the mold and to ensure an intimate contact with the substrate. However, increasing the pressure often leads to distortion and fracture of the stamp. This can be remedied using a tough material to prevent brittle failure. Therefore, a balance between stiffness, flexibility, and toughness is essential to allow a reproducible conformal contact, and to prevent deformation of the mold for high resolution patterning of small nanostructures [146].

9.3 Novel Robust and Flexible Plastic Molds

In order to solve the problem of the low mechanical resistance often encountered with plastic stamps, I used nanoimprinting to fabricate robust and non-adhesive molds made of a fluorinated polymer. During the course of this work, I used different fluorinated thermoplastics, among which the fully fluorinated polytetrafluoroethylene (PTFE), a fluorinated ethylene propylene (FEP), ethylene(tetrafluoroethylene) ETFE, and a perfluoroalkoxy copolymer (PFA). Each material shares the usual benefits of fluorinated polymers (low surface energy, high temperature resistance), however they also differ in a number of ways which limits their suitability as a mold's material (see Table 9.1).

The main drawbacks of PTFE are its relative softness compared to the other polymers used in this study, and its high melt viscosity, requiring high processing temperatures, which makes it difficult to shape into a master containing small

Fluoropolymer	Melting temp. (°C)	Elastic modulus (GPa)	Transmittance (%)
ETFE	255-280	1.0–1.2	93–95
FEP	250-280	0.48	96
PFA	300-310	0.48	>90
PTFE	327-330	0.40	N/A

Table 9.1: Properties of several fluoropolymers selected as possible candidates for molds. All values are given at room temperature unless specified otherwise. The transmittance is given in the range 350–800 nm for a 25 μm thick sheet. Data from [147].

nanofeatures. It is also subject to cold flow, and it is not tranparent, which makes UV curing embossing impossible. FEP is less temperature resistant than the other mentionned polymers, and its elastic modulus is also smaller than PFA and ETFE, which makes it easier to deform under pressure. PFA is transparent, it has a high melting point and a good rigidity (modulus $\sim 0.5\,\mathrm{GPa}$), however it tends to strongly bond to metals when molten which makes it difficult to process (the imprinting tools used are usually metallic). ETFE has a high melting point and a relatively high rigidity (modulus>1 GPa) [147]. It also has the advantage that it is flexible, tough, and can be processed at around 200 °C.

Experiments performed with ETFE showed the best combination of mechanical properties and thermal stability for imprinting at elevated temperatures and at high pressures. We therefore used ETFE molds, also called fluoromolds, to imprint a variety of polymers with a large range of features sizes and shapes. These molds are mechanically resistant and can withstand large pressures without deformation. Unlike previous studies which used a spin-casting process of fluorinated solutions such as Teflon AF [138, 139], we have used an embossing process that allows the production of thicker molds with an improved mechanical stability which is necessary for fine patterning of nanostructures. The present molds were produced by embossing 100–200 μm thick ETFE sheets into a patterned silicon master. The high melting point of ETFE confers the mold a high thermal stability. The masters were processed by traditional lithography and etching, which yielded a high definition of structures on the surface of the mold. The patterned ETFE sheet was then used as the mold to imprint another polymer substrate (either a thin polymer film deposited onto a rigid substrate, or a thicker free standing polymer sheet). Schematic drawings of the embossing process using the ETFE mold are shown in Fig. 9.2.

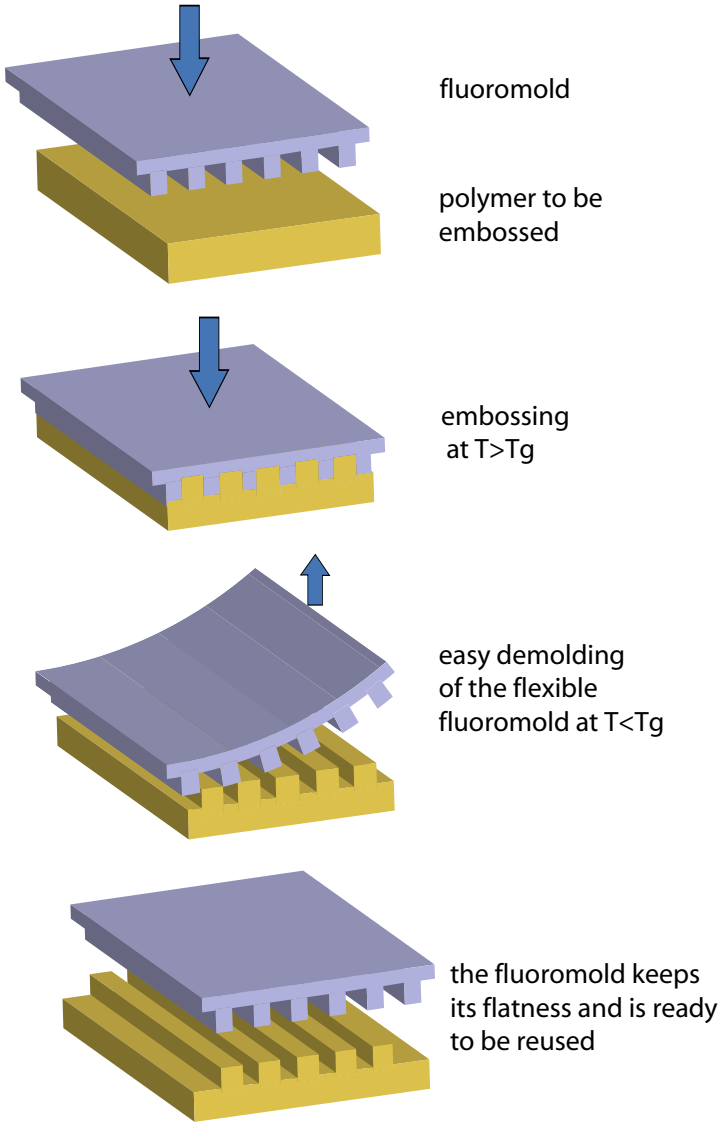

Figure 9.2: Schematic diagram of embossing with a flexible fluoromold. During cooling and demolding, the fluoromold is bent and gradually separated from the substrate using only a low force since it doesn't adhere to the polymer. The fluoromold does not break nor deform, and can therefore be reused several times.

9.3.1 Reproduction of Sub-20 nm Features

Figure 9.3 shows the reproduction of dots and lines with feature sizes less than 20 nm into a ∼100 nm thick polystyrene film of molecular weight ∼70,000 g/mol. The film was spin-coated onto a silicon substrate, heated to 170 °C, and embossed with an ETFE stamp for 200 seconds. The pressure was supplied from a compressed air system (Obducat, Sweden) which uniformly applies an hydrostatic pressure on the back side of the stamp. The reported pressures are the effective pressures at the beginning of embossing, calculated from the actual surface of the stamp in contact with the substrate. The effective pressure is highest at the beginning of imprinting, decreasing to its lowest value when the entire surface of the mold is in contact with the embossed polymer. Due to the difference in area coverage of the various structures shown in Fig. 9.3, the effective pressure were ∼12.5 bar for the 70 nm dots, 24 bar for the ∼45—50 nm dots and ∼32.5 bar for the lines with lateral feature sizes of ∼14 nm. Once the patterns were fully formed, the pressure decreased to 6.5 bar for the lines and the ∼70 nm dots, and to 15.5 bar for the ∼45–50 nm dots. The size of the structures was similar to those on the original silicon master as measured by SEM (see Fig. 9.3 c and d which show the structures imprinted into PMMA and the original structures on the silicon master). The ∼70 nm dots which form a very dense array with a period of ∼90 nm (Fig. 9.3 b) were also well defined. Remarkably, the walls of the ETFE mold which are as thin as ∼12–18 nm, are strong enough to resist the applied pressure at high temperatures, forcing the polymer material to flow into the mold structures. No sticking of the polymer to the stamp was found and demolding of the structures was very easy and clean because of the flexibility of ETFE.

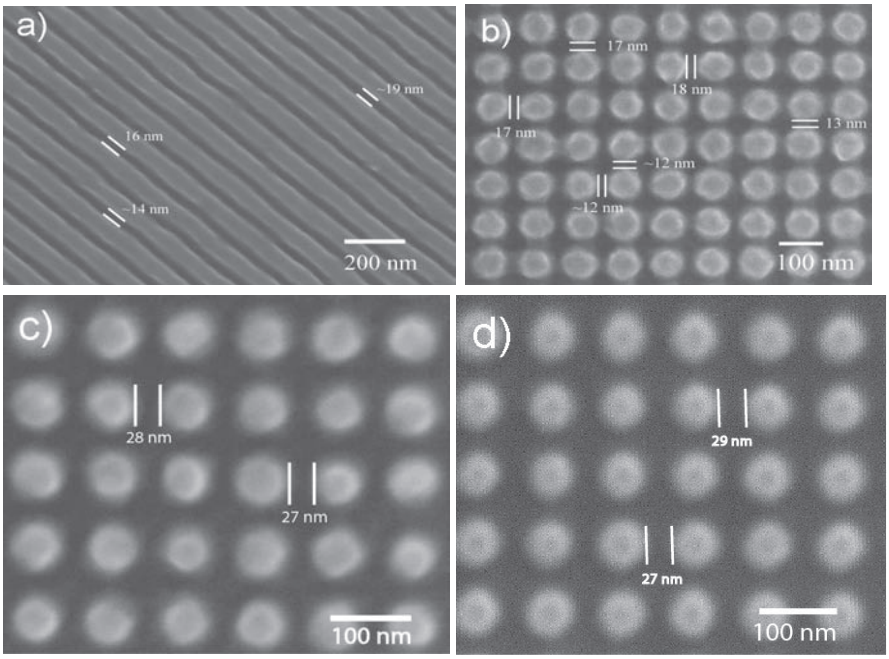

Figure 9.3: Scanning electron microscopy images of fine structures embossed from an ETFE fluoromold. a) Channels as small as ∼14 nm imprinted into PS at a pressure of 32.5 bar; b) densely packed ∼70 nm pillars with a period of ∼90 nm imprinted into PS at a pressure of 12.5 bar, showing a ∼12 nm inter-pillar spacing. c) ∼45–50 nm dots with a spacing of ∼25 nm imprinted into PS at 24 bar; d) array of ∼45–50 nm dots on the silicon master used to produce the ETFE mold that served to imprint the dots shown in (c).

9.3.2 Effect of the Imprinting Pressure

Low Pressure Imprinting

Structures with various shapes and sizes were imprinted into commercially available ∼2 mm thick sheets of poly(methylmetacrylate) PMMA in the temperature range 135–160 °C at various pressures. Because we wanted to investigate the effect of imprinting at low pressures, a sample was heated on a heating plate and a low pressure of ∼1 bar was applied from a small home-made mechanical press. Figure 9.4 a and b show an example of 700 nm wide lines (with a 2 μm period and a height of 160 nm) imprinted into PMMA at 160 °C and 1 bar. The size of the structures was identical to that of the original master, as verified by SEM and AFM. Pillars imprinted at a pressure of 2.2 bar also showed excellent pattern definition, and the structures were undistinguishable from the ones imprinted at higher pressure (see Fig. 9.4 c).

High Pressure Imprinting

Further experiments were performed with a higher pressure, which was applied from an hydrostatic heated press (Obducat AB). The mechanical stability of the ETFE mold was tested by embossing PMMA with a fluoromold at 145 °C with a wide range of pressures (Table 9.2). The pressure was maintained at the embossing temperature for 2 minutes. The lateral dimensions of the resulting structures were then measured using a SEM and compared to the original dimensions of the mold. Table 9.2 and Figure 9.5 a show that perfect replication without deformation was obtained with the fluoromold with effective pressures ranging from ∼2.2 to 55 bar. Embossing at higher pressures was not attempted, but this result suggests that the ETFE mold could withstand pressures greater than 55 bar. The same experiment was repeated with a PDMS stamp which was

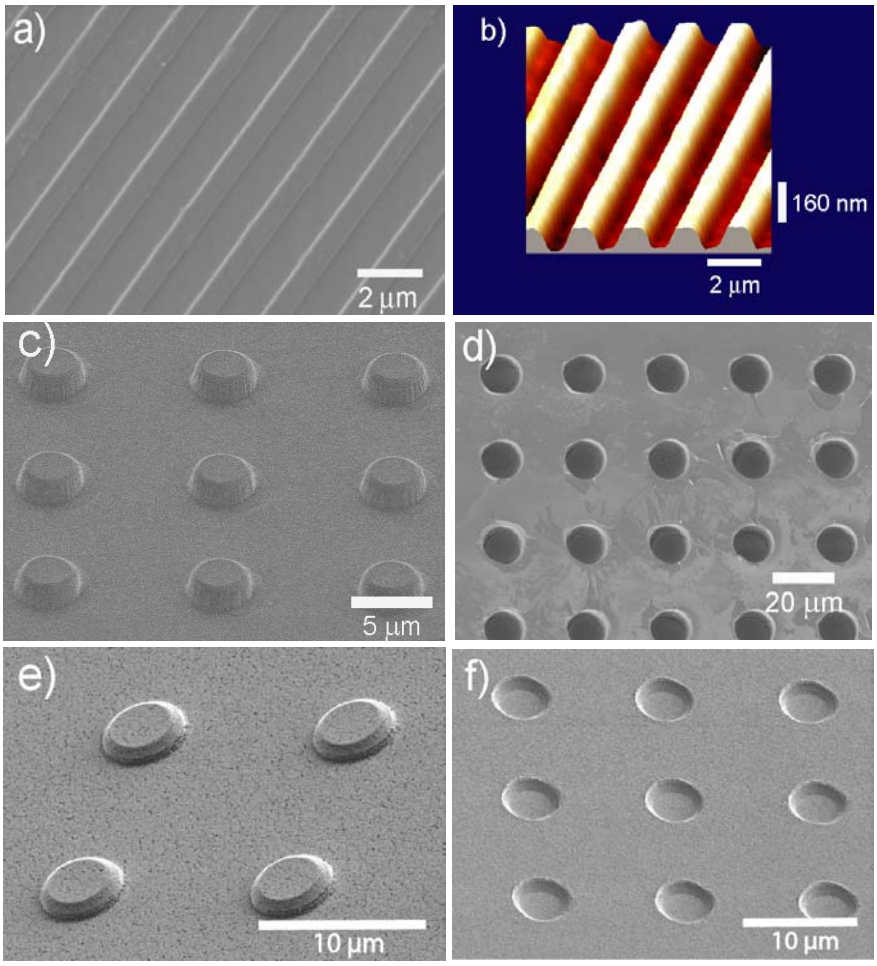

Figure 9.4: Scanning electron microscopy images showing various microstructures embossed from an ETFE fluoromold. a) Image of 700 nm wide lines with a 2 μm period imprinted into PMMA at 160 °C and a pressure of 1 bar; b) AFM image of the structures in (a) showing a height of 160 nm which is identical to that of the original silicon master used to produce the ETFE fluoromold that served to emboss the lines. c) Example of $\sim$4 μm pillars in PMMA that were embossed at 145 °C and 44 bar for 2 minutes with an ETFE fluoromold which was previously used 5 consecutive times. d) 11 μm wide and 11.5 μm deep holes embossed into PMMA at 135 °C, and 4.7 bar for 5 min. e) $\sim$4 μm pillars in Teflon AF 1600 at $\sim$175 °C, and $\sim$17 bar. The graininess of the picture is due to the porosity on the surface of the Teflon AF. f) ETFE stamp after imprinting the structures shown in (e).

Sample	Diameter (μm)	Ratio to mold	Period (μm)	Ratio to mold
ETFE mold	4.37		11.80	
PMMA 2.2 bar	4.35	1.00	11.50	0.97
PMMA 16.5 bar	4.40	1.01	12.06	1.02
PMMA 22 bar	4.39	1.00	11.91	1.01
PMMA 33 bar	4.40	1.01	11.85	1.00
PMMA 55 bar	4.38	1.00	11.92	1.01

Table 9.2: Embossing of PMMA with an ETFE fluoromold at 145 °C, for 2 min at various pressures. The values are the averages of several measurements.

patterned by deposition of the liquid PDMS onto a structured silicon master and by curing for 24 h at 170 °C. These conditions provide an elastic modulus of ∼4 MPa. As can be seen in Table 9.3 and Figure 9.5 b, the structures embossed with the PDMS stamp were strongly deformed even at low pressures, resulting in elongated and distorted patterns. This result shows that the fluoromolds can be used for nanoimprinting at the higher pressures usually used with stiffer inorganic molds and that no deformation or loss of resolution is observed. Combined with the advantage of their low adhesion and flexibility, ETFE fluoromolds can therefore be used to replace brittle and expensive inorganic materials, as well as deformable elastomers and other plastic molds which lack strength when pressure is applied. The strength and robustness of ETFE stamps is essential for embossing large microstructures as well as small nanostructures with lateral dimensions approaching 10 nm.

9.3.3 Imprinting of Temperature Resistant Polymers

Imprinting with the ETFE fluoromold was also performed at a pressure of ∼17 bar into a ∼1 mm thick carbon reinforced high density polyethylene (CRHDPE)

Sample	Diameter (μm)	Ratio to mold	Period (μm)	Ratio to mold
PDMS mold	4.42		11.82	
PMMA 2.2 bar	6.32	1.43	13.81	1.17
PMMA 33 bar	7.88	1.78	15.48	1.31

Table 9.3: Embossing of PMMA with a PDMS mold at 145 °C, for 2 min at various pressures. The values are the averages of several measurements.

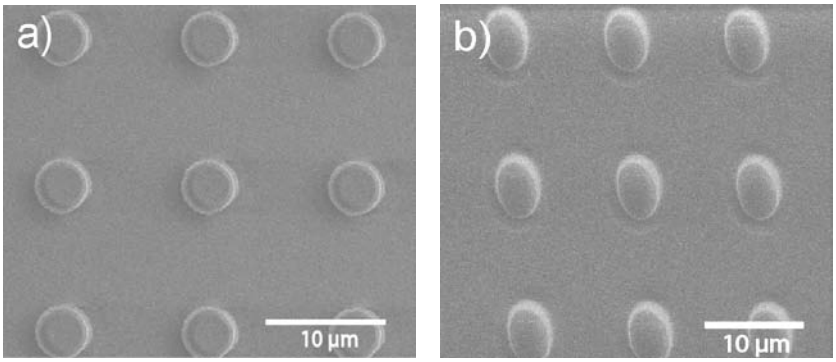

Figure 9.5: Scanning electron microscopy images showing the effect of pressure on the reproduction of the embossed patterns with a fluoromold and with a PDMS stamp. a) 4 μm pillars in PMMA that were embossed at 145 °C and $\sim$55 bar for 2 min with an ETFE fluoromold. b) Deformed pillars embossed in PMMA with a PDMS stamp at 145 °C and $\sim$33 bar for 2 min.

sheet at 140 °C, and into a ∼3 μm thick film of Teflon AF 1600 spin-coated onto a silicon substrate at ∼175 °C. In both cases, the structures were very well defined and identical to that of the stamp. The embossed structures in Teflon AF are shown in Figure 9.4e, and the ETFE mold used to imprint the structures is shown in Figure 9.4f. The ETFE mold showed no deformation after embossing, which suggests that ETFE has superior mechanical properties compared to Teflon AF in pressure assisted imprinting at high temperatures. The reverse experiment was also performed, where a structured Teflon AF mold was used to imprint a sheet of ETFE in the same conditions as above. Inspection of the mold after demolding showed that the structures on the surface of the Teflon AF layer were largely gone, and the ETFE sheet showed no sign of imprinting. Clearly, the ETFE fluoromold retains enough strength and stiffness for embossing of a large range of polymers, including Teflon AF, at temperatures up to at least 175 °C.

9.3.4 Imprinting of Larger Microstructures

Finally, to further test the versatility of ETFE molds for NIL, we imprinted 11 μm wide pillars into PMMA at 135 °C and 4.7 bar for 5 minutes. Figure 3d shows the resulting holes. The structures were very well defined on the entire embossed area, including near the edges of the sample. Imprinting large micron-scale features is often challenging because a large amount of material has to be displaced over a relatively large distance. Therefore, the mold has to resist distortion and deformation during the replication process. After imprinting, the pillars on the mold were intact and no deformation of the mold was observed. The depth of the holes, measured by a scanning electron microscope cross-section, was identical to the height of the pillars on the surface of the mold

($\sim$11.5 μm).

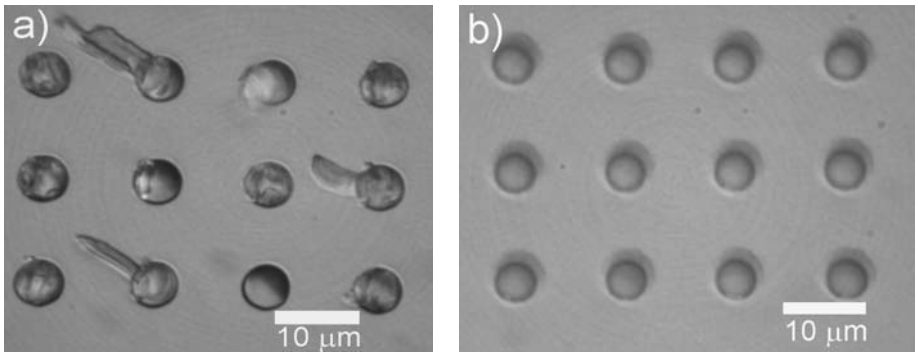

Figure 9.6: Optical microscopy images of the surface of a) a silanized silicon mold after 3 consecutive embossings, and b) an ETFE mold after 6 consecutive embossings. The experiments were performed at 145–160 °C, 7 bar and for 3.5 min. a) The embossed PMMA adheres to the inside of the holes on the silicon mold after 3 imprints, whereas the holes of the ETFE fluoromold (b) show no sign of adhered polymer after 6 imprints.

9.3.5 Multiple Embossing and Large Area Imprinting

Demolding structures from a stiff inorganic stamp often results in fracture of both the embossed structures and the stamp itself because of adhesion between the stamp and the substrate. Moreover, when using a rigid mold the entire embossed surface must be separated at the same time, requiring a large force which contributes to the mold fracture. In the set of experiments shown in Figure 9.6, we compare the surface of a silanized silicon mold with a fluoromold after 6 consecutive embossings into PMMA at 145–160 °C, at a pressure of 7 bar for 3.5 minutes. No cleaning of the molds was performed between the different imprints. The silicon mold was silanized with 1H,1H,2H,2H-perfluorodecyltrichlorosilane diluted in purified benzene. The solution was inserted with the masters into a sealed glass container, and was allowed to slowly evaporate at room temperature

and overnight to cover the surface of the silicon substrate with an anti-adhesive layer. The resulting advancing water contact angle was 115 ° on a smooth surface, confirming the change in surface chemistry. In comparison, the advancing water contact angle on a smooth ETFE surface with a similar roughness as that of the silicon master was 104 °. Figure 9.6 a shows PMMA adhering to the silicon mold after only 3 embossings, making it unusable for further imprints. On the other hand, the ETFE mold was still clean after 6 embossings, and showed no trace of polymer adhering to its surface (Fig. 9.6 b). The structures embossed by the fluoromold were still very well defined after the sixth imprint, suggesting that these stamps could be used many more times without being damaged. Figure 3c shows pillars that were obtained at 44 bar with a mold that was previously used 5 times. Again the replication is identical to the structures of the original master, and the tops of the pillars are flat which shows full polymer filling of the mold's cavities during embossing. Multiple embossing of 700 nm lines was also performed at pressures as low as ∼1 bar. After six embossings with the same mold at a temperature of 135–140 °C, no degradation of the mold or of the embossed patterns was observed. Varying the embossing temperature between 115 and 160 °C also yielded similar results. The lateral dimensions and height of the embossed structures were identical to those of the original master as confirmed by both SEM and AFM. Furthermore, embossing of large areas was performed into CRHDPE sheets at 140 °C with a ∼50 mm × 40 mm ETFE mold which consisted of several regularly spaced regions of 8 mm × 8 mm with structures similar to the ones shown in Figure 9.4 f. The total area covered by these 8 mm × 8 mm squares was approximately 20% of the entire surface of the mold. The fluoromold showed no adhesion to the polymer substrate during embossing, and it was easily removed by sequential demolding thanks to the flexibility and low-adhesion of the stamp. The replication of the patterns occurred throughout

the area of the mold which was covered by the structures, and the quality of the replicated patterns was the same as that shown in Figure 9.4.

9.3.6 A Stretchable Organic Laser

The idea of this collaboration with the Optoelectronics group at the Cavendish Laboratory was to pattern an elastic material with regular nano-grooves to produce a flexible optical grating. The active F8BT (poly(9,9-dioctylfluorene-co-benzothiadiazole)) layer was patterned by NIL from an ETFE mold which had nano-grooves on its surface. The F8BT was patterned on a thin (50 nm) sacrifical layer of polystyrene sulfonic acid (PSS, Aldrich) spin-coated on a solid substrate. The F8BT layer was then covered with a PDMS film and cured at room temperature to cross-link it. The PSS film was dissolved in water to transfer the F8BT grating unto a PDMS matrix. The periodicity of the grating (353 nm) can be easily varied by mechanical stress. This change in the period of the grating produces lasing at different frequencies when excited by a short pulse laser (150 fs) at 480 nm. The typical bandwidth of emission was ∼1 nm. All the experiments were carried out by B. Wenger, and I helped him mainly with the patterning and encapsulating of the F8BT layer into the PDMS matrix. The use of the PDMS matrix ensures a good mechanical resistance against delamination of the active layer during stretching. The range of wavelengths for emission extends over ∼20 nm from the lower emission at ∼567 nm when the laser is stretched from 0 to ∼7% [115].

9.4 Transparent Microstructured Substrates for Studying Insect Adhesion

This work was performed in collaboration with the group of Dr. Federle at the Department of Zoology at the University of Cambridge. The idea was to use an innovative approach to study insect adhesion by using controlled structured surfaces instead of the traditional flat glass slide.

9.4.1 The Reasons for Studying Insect Adhesion

Many insects have the exceptional ability to climb up or down almost any type of surface. Understanding the science of insect adhesion is an interesting and challenging task which can also potentially have a strong technological impact. The development of biomimetic adhesives for instance has been a field of intense activity in the past decade. The promise of better, stronger adhesives which can be reused many types on any type of surface has been a strong driving force for the development of biomimetic adhesives. Manipulation of micro and nano-objects is also an area which could benefit from a better understanding of insect adhesion. The operation of micro- and nano-electromechanical systems (MEMS and NEMS) is often impeded by the phenomenon of stiction (strong adhesion of two parts when they come into contact and difficulty to separate them) [148]. A large number of micro- and nano-processes are also limited by an incomplete understanding of adhesion on the micro- and nano-scale, and it has become clear that there is a strong need to develop technologies that can control adhesion effectively [149, 150]. Bottom-up processes and nano-manipulation, which represent a large and promising area of research for manufacturing novel and smart nano-objects often require transporting nanoscopic parts by adhesion

and release using Van der Waals forces [151]. A better understanding of adhesion between micro- and nano-structures and better adhesive designs are therefore required for a large number of technological applications.

Animal adhesive organs are able to attach strongly to almost any surface, but also to detach easily for fast climbing. They can go through millions of attachment/detachment cycles without wear nor contamination [152]. Another important and less studied property of insect adhesives is that they can conform and retain strong adhesion on rough surfaces, which are often encountered in their natural habitat [153, 154].

9.4.2 Study of Cockroach Adhesion on Rough Surfaces

In this study we used microstructured substrates with a well defined roughness to perform quantitative measurements of cockroach (*Nauphoeta cinerea*) adhesion and friction. The friction and adhesion measurements were performed by C. Clemente and the group of W. Federle in Zoology, who used interference microscopy to monitor the contact area between the pad and the micro-structures (see Fig. 9.7).

Preparation of the Microstructured Transparent Surfaces

The microstructures were made by imprinting a polymethylmethacrylate (PMMA) film deposited on a thin glass slide with an ETFE mold. PMMA was chosen for its high transparency, resistance to mechanical abrasion, and because its index of refraction nearly matches that of glass ($\sim$1.46 vs. $\sim$1.50). Pillar structures of $\sim 4\,\mu$m in diameter were produced on top of a 0.1 mm thin transparent glass slide (Fig. 9.7). The periodicity between the pillars was $12\,\mu$m. The height of the pillars was varied between 1 and $4\,\mu$m. Smooth PMMA surfaces were produced

by imprinting the PMMA film with the smooth part of the ETFE molds.

The detailed preparation is as follows. The polymer solution was prepared by dissolving a PMMA powder (M_{m}= 330,000 g/mol, Polymer Labs) in toluene (∼8-10% wt.). A film of PMMA was prepared by spin-coating the solution onto a glass slide ($12 \times 12 \times 0.1\,\mathrm{mm}^3$) which had previously been cleaned in acetone (and in isopropanol) for 30 min at 40 °C in an ultrasonicator, followed by blow drying in a nitrogen atmosphere. The glass slide was next cleaned with carbon dioxide snowjet to remove any dust and small particles that could have adhered onto the surface of the glass slide. The PMMA film was formed by spin-coating the solution onto the clean glass slide. Imprinting of the film was performed by placing the film and the ETFE mold in contact (without any additional applied pressure) and heating to 150 °C. Once a constant temperature was reached, a pressure of 20 bar was applied by a mechanical press (Obducat AB, Sweden) for several minutes to ensure complete filling of the mold by the PMMA melt. The assembly was then cooled down to 40 °C by an air cooling system mounted onto the press. The pressure was released, and the glass/PMMA substrate was separated from the ETFE mold. This procedure yielded a well defined $4 \times 4\,\mathrm{mm}^2$ microstructured array of ∼4 μm diameter flat-topped pillars, with near vertical walls. Figure 9.8 shows 1 μm high pillars used in the analysis.

Results and Advantage of Using Flexible Molds for this Study

Previous adhesion/friction experiments performed on smooth glass slides had shown that cockroaches use two different types of organs for locomotion [155]. The arolium serves the function of an adhesive organ, whereas the euplantula is used as a friction pad. In this project, both adhesion and friction of cockroach pads was studied on smooth and rough surfaces of the same material (PMMA) [114]. The results show that on smooth surfaces and substrates with

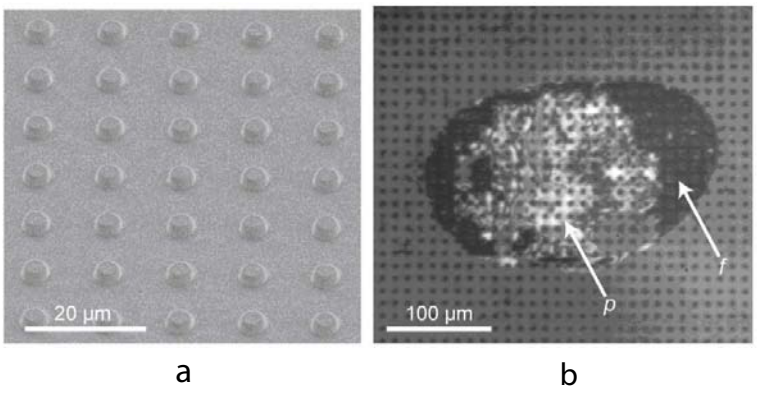

Figure 9.7: a) Transparent surface with 1 μm high pillars; b) Cockroach adhesive pad in contact with the micro-structured surface (p: contact only with the tops of the pillars, f: full contact); picture (b) courtesy of W. Federle.

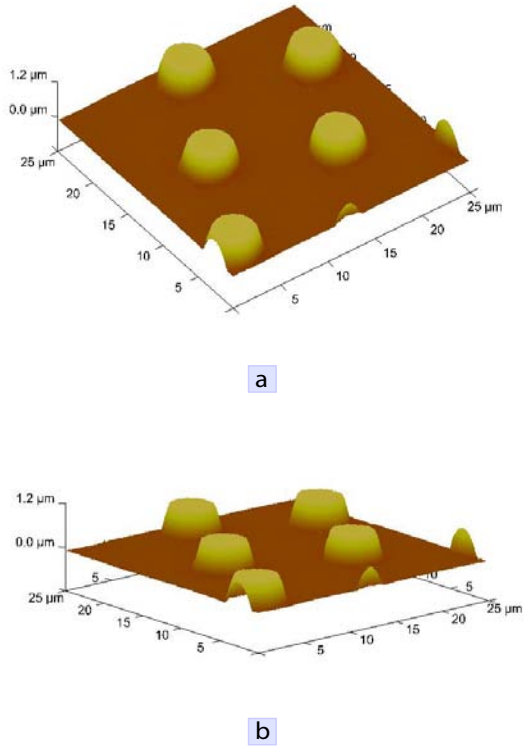

Figure 9.8: AFM pictures of 1 μm high pillars imprinted in PMMA. The pillars are shown from the top (a) and in cross section (b), showing their near vertical walls and their flat tops.

shallow structures (1 μm high pillars), adhesion dominates over friction. However, on rougher surfaces (4 μm high pillars) the adhesive strength is reduced and friction forces become stronger. This result is explained by the fact that on shallow structures, the pads make complete contact with the surface, which increases adhesion and thereby also increases friction. However, on the rougher surfaces, the pad makes contact only with the top of the structures. This reduces adhesion, and makes friction forces become more important by interlocking of the euplantulae nanometric ridges with the microstructures (Fig. 9.9).

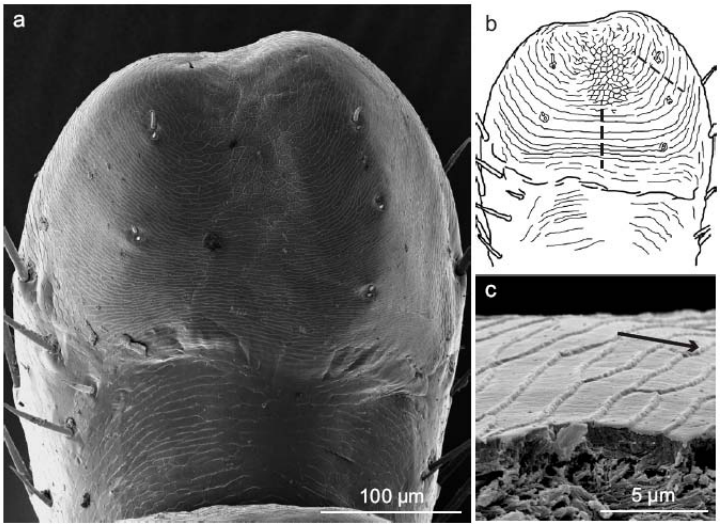

Figure 9.9: Pictures of the euplantulae of a cockroach (courtesy of C. Clemente). (a) SEM picture of the pad, (b) drawing showing the structured surface of the pad, (c) SEM close view of the asymmetric nanometer ridges at the surface of the euplantulae.

The use of transparent surfaces with a well controlled roughness therefore allowed for the first time the study of the mechanisms of adhesion and friction of cockroaches on rough surfaces. The advantage of using ETFE stamps lies in the fact that their low adhesion and flexibility reduces detachment forces during demolding, and reduces the risk of breaking the thin and fragile glass

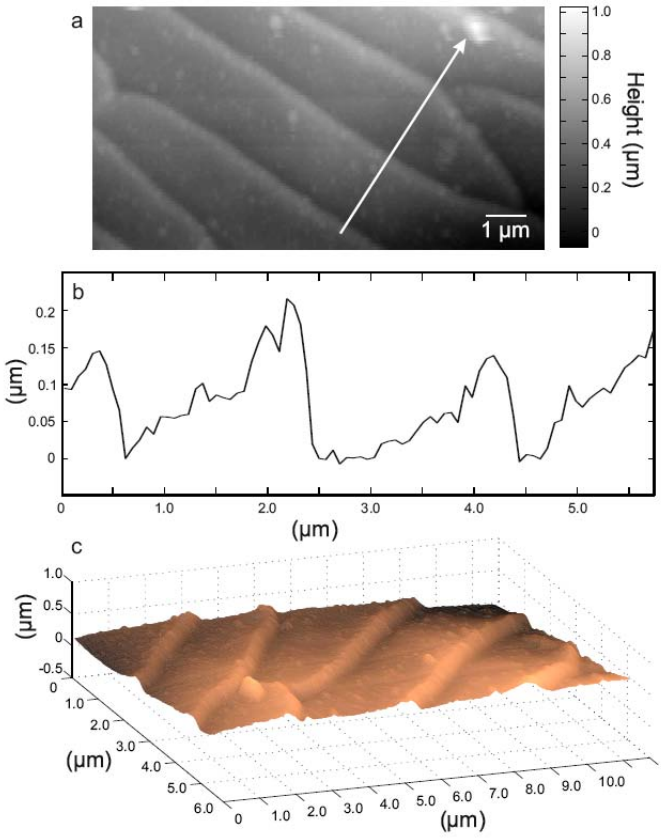

Figure 9.10: AFM pictures of the surface of the euplantulae of a cockroach (courtesy of C. Clemente). (a) 2D view of ridges on the surface of the pad, (b) surface profile showing ∼200 nm high ridges, (c) 3D view where the asymmetry of the ridges, which is responsible for directional friction, is clearly visible.

slides. Another advantage is the possibility to create rough surfaces with tailored chemical properties. A large variety of materials with different properties (e.g. hydrophilic or hydrophobic, soft or stiff) can be patterned with ETFE molds.

Chapter 10

Conclusion and Outlook

This thesis has spanned a large range of methods for micro- and nano-structuring polymer surfaces. Self-assembly of thin liquid polymer films using electric fields constituted one large part on the thesis, while the second part dealt with nanoimprinting.

10.1 Rheology of Thin Liquid Films

The rheology of thin polymer melts was studied by probing the free surface of the film with electric fields (Chapters 7 and 8). It was shown that the characteristic time τ of destabilization is directly proportional to the film viscosity. A new experimental set-up was built to measure τ and the corresponding wavelength λ. We also designed a new interferometric method to measure the thickness of micron-wide fluctuations in thin dielectric films with a sub-nm resolution. Comparison of the experimental τ with the predictions from the linear stability analysis of the film showed that the measured τ were much smaller than the calculated one for large chains (above the entanglement length). We showed that this discrepancy is due to non-equilibrium effects caused by the spin-coating of a dilute solution of polymers onto a substrate to form a thin film. Chains far from

equilibrium have an increased mobility compared to chains in equilibrium. The films can be re-equilibrated by annealing them for long times at temperatures well above T_g. This abnormally slow re-equilibration process is not explained, but it has been experimentally observed by several other authors. We proposed a model to explain the increased mobility of the as-cast films. The model proposes that the fast evaporation of solvent from the films during spin-coating creates a lower entanglement density in the film compared to the bulk of the same material. Annealing allows the chains to re-entangle, which increases the viscosity of the film to the bulk value. Surprisingly, slip was not observed during at the very early stages of the film destabilization process. Experiments on surfaces with two different interfacial energies between the solid and the liquid showed no measurable difference in τ. We propose that slip cannot be observed at the very early stages of destabilization when the amplitude of the EHD surface fluctuation is very small (a few nanometers) because the stress induced by the electric field is too weak. Slip may be observable at later stages when the fluctuation grows above a certain height because larger pressures are generated in the film. Measurements of the growth rates of the instability seem to indicate an increased growth above $\sim$25 nm in the PS films of initial thickness $\sim$120–140 nm. It was found that the instability grows exponentially in time, confirming the capillary approximation of the surface amplitude which is valid in the linear regime. Another interesting result was that we did not observe destabilizing built-in in-plane stresses in the thin PS films that we studied. Instead, slightly stabilizing stresses were measured in the films. Interesting experiments could be performed to shed some light on the effect of stresses on the stability of thin films. For example, similar experiments to the ones performed in Chapters 7 and 8 could be performed by varying the size of the chains, the film thickness and the spin-coating conditions in a systematic way. Also, annealing experiments where

a thin film is spin-coated on a substrate which already has undulations on its surface would be interesting to perform. The thin film could be transferred to a smooth and flat surface, and annealed. One could determine whether stored-in stresses contribute to the growth of the surface undulations or if the undulations simply decay when annealed without electric field.

10.2 Novel Flexible Molds for Nanoimprinting

Chapter 9 introduced the development of a new type of flexible and anti-adhesive plastic molds for imprinting. These molds made of ETFE, do not deform under pressures conventionally used in imprinting techniques, and they are also highly resistant to chemicals and temperature. One main advantage of ETFE molds compared to traditional inorganic molds is that they are flexible, and can be peeled off the imprinted polymer without breaking. They can also be reused multiple times and they are well suited for imprinting large areas because of their flexibility and anti-adhesive properties. Imprinting of a wide range of polymers is demonstrated , including Teflon AF which has a T_g of 160 °C. ETFE molds were used to reproduce pillars, holes and lines ranging from $\sim$10 μm to $\sim$10 nm. These new molds should find many applications where silicon molds are either too brittle or too expensive to produce in large quantities (e.g. when imprinting nanostructures). Finally, we showed the application of these molds to study insect adhesion on transparent, microstructured surfaces. A new friction mechanism of interlocking was found by measuring friction forces of cockroach pads on micron-sized pillars. Looking forward, this last project has also lead to the writing of a grant proposal to continue the study of insect adhesion on rough surfaces, and to make novel biomimetic adhesives with improved properties compared to traditional pressure sensitive adhesives. Some of the desirable

properties of biological adhesive organs are strong adhesion and easy release on almost any surface, self-cleaning and resistance to wear. Only time will tell if man can come closer to reproducing natural systems with as much success as nature itself...

Bibliography

[1] E. Schaffer, T. Thurn-Albrecht, T. P. Russell, and U. Steiner. Electrically induced structure formation and pattern transfer. *Nature*, 403:874–877, 2000.

[2] N. E. Voicu, S. Harkema, and U. Steiner. Electric-field-induced pattern morphologies in thin liquid films. *Advanced Functional Materials*, 16:926–934, 2006.

[3] E. Schaffer, T. Thurn-Albrecht, T. P. Russell, and U. Steiner. Electrohydrodynamic instabilities in polymer films. *Europhys. Lett.*, 53 (4):518–524, 2001.

[4] Z. Lin, T. Kerle, S. M. Baker, D. A. Hoagland, E. Schaffer, U. Steiner, and T. P. Russell. Electric field induced instabilities at liquid/liquid interfaces. *J. Chem. Phys.*, 114 (5):2377–2381, 2001.

[5] Z. Lin, T. Kerle, T. P. Russell, E. Schäffer, and U. Steiner. Structure formation at the liquid/liquid bilayer in electric fields. *Macromolecules*, 35:3971–3976, 2002.

[6] S. Y. Chou, P. R. Krauss, and P. J. Renstrom. Imprint of sub-25 nm vias and trenches in polymers. *Appl. Phys. Lett.*, 67:3114–3116, 1995.

[7] S. Y. Chou, P. R. Krauss, W. Zhang, L. Guo, and L. Zhuang. Sub-10 nm imprint lithography and applications. *J. Vac. Sci. Technol. B*, 15(6):2897–2904, 1997.

[8] D. R. Barbero, M. S. M. Saifullah, P. Hoffmann, H. J. Mathieu, D. Anderson, G. A. C. Jones, M. E. Welland, and U. Steiner. High resolution

nanoimprinting with a robust and reusable polymer mold. *Advanced Functional Materials*, 17:2419, 2007.

[9] E. Shaffer. *Instabilities in thin polymer films: structure formation and pattern transfer*. PhD thesis, University of Konstanz, 2001.

[10] R. P. Feynman, R. B. Leighton, and M. Sands. *The Feynman Lectures on Physics*. Addison-Wesley (New York), 1963.

[11] E. Schnell. Slippage of water over nonwettable surfaces. *J. Appl. Phys.*, 27:1149, 1956.

[12] K. B. Migler, H. Hervet, and L. Léger. Slip transition of a polymer melt under shear stress. *Phys. Rev. Lett.*, 70(3):287, 1993.

[13] S. Granick, Y. Zhu, and H. Lee. Slippery questions about complex fluids flowing past solids. *Nature Mat.*, 2:221, 2003.

[14] Y. Zhu and S. Granick. Limits of the hydrodynamic no-slip bc. *Phys. Rev. Lett.*, 88 (10):106102, 2002.

[15] T. Schmatko, H. Hervet, and L. Léger. Friction and slip at simple fluid-solid interfaces: the roles of the molecular shape and the solid-liquid interaction. *Phys. Rev. Lett.*, 94(24):244501, 2005.

[16] C. Neto, D. R. Evans, E. Bonaccurso, H-J. Butt, and V. S. J. Craig. Boundary slip in newtonian liquids: a review of experimental studies. *Rep. Prog. Phys.*, 68:2859, 2005.

[17] P. G. de Gennes. G. wetting: statics and dynamics. *Rev. Mod. Phys.*, 57:827, 1985.

[18] A. R. P. Rau. Biological scaling and physics. *J. Biosci.*, 27:475–8, 2002.

[19] T. D. Blake. Slip between a liquid and a solid—tolstoi d m (1952) theory reconsidered. *Colloids Surf.*, 47:135–145, 1990.

[20] Westin J. A. Choi C-H. and Breuer K. S. Apparent slip flows in hydrophilic and hydrophobic microchannels. *Phys. Fluids*, 15:2897–2902, 2003.

[21] R. Pit, H. Hervet, and L. Léger. Direct experimental evidence of slip in hexadecane: Solid interfaces. *Phys. Rev. Lett.*, 85(5):980–983, 2000.

[22] E. Bonaccurso, H-J. Butt, and V. S. J. Craig. Surface roughness and hydrodynamic boundary slip of a newtonian fluid in a completely wetting system. *Phys. Rev. Lett.*, 90:144501, 2003.

[23] J-H. J. Cho, Law B. M., and Rieutord F. Dipole-dependent slip of newtonian liquids at smooth solid hydrophobic surfaces. *Phys. Rev. Lett.*, 92:166102, 2004.

[24] J.S. Ellis and M. Thompson. Slip and coupling phenomena at the liquid–solid interface. *Phys. Chem. Chem. Phys.*, 6:4928 – 4938, 2004.

[25] P. A. Thompson and S. M. Troian. A general boundary condition for liquid flow at solid surfaces. *Nature*, 389:360–362, 1997.

[26] J. Sanchez-Reyes and L.A. Archer. Interfacial slip violations in polymer solutions: role of microscale surface roughness. *Langmuir*, 19:3304–3312, 2003.

[27] S. Richardson. On the no-slip boundary condition. *J. Fluid Mech.*, 59:707–719, 1973.

[28] L. Bocquet and J-L. Barrat. Hydrodynamic boundary conditions and correlation functions of confined fluids. *Phys. Rev. Lett.*, 70:2726–2729, 1993.

[29] K. Watanabe, Y. Udagawa, and H. Udagawa. Drag reduction of a newtonian fluid in a circular pipe with a highly water-repellent wall. *J. Fluid Mech.*, 381:225–238, 1999.

[30] C. Cottin-Bizonne, J-L. Barrat, L. Bocquet, and E. Charlaix. Low-friction flow of liquid at nanopatterned interfaces. *Nat. Mater.*, 2:237–240, 2003.

[31] T. M. Galea and P. Attard. Molecular dynamics study of the effect of solid roughness on the slip length at the fluid-solid boundary during shear flow. *Langmuir*, 20:3477–82, 2004.

[32] F. Brochart and P. G. de Gennes. Shear-dependant slippage at a polymer/solid interface. *Langmuir*, 8 (12),:292, 1992.

[33] L. Léger, H. Hervet, and L. Bureau. Friction mechanisms at polymer-solid interfaces. *Comptes Rendus Chimie*, 9:80, 2006.

[34] L. Léger, H. Hervert, G. Massey, and E Durliat. Wall slip in polymer melts. *J. Phys.: Condens. Matter*, 9:7719–7740, 1997.

[35] J. Yang, J. Duan, D. Fornasiero, and J. Ralston. Very small bubble formation at the solid-water interface. *J. Phys. Chem. B*, 107:6139–47, 2003.

[36] X. H. Zhang, X. D. Zhang, S. T. Lou, Z. X. Zhang, J. L. Sun, and J. Hu. Degassing and temperature effects on the formation of nanobubbles at the mica/water interface. *Langmuir*, 20:3813–3815, 2004.

[37] P. G. de Gennes. On fluid / wall slippage. *Langmuir*, 18(9):3413–3414, 2002.

[38] J. Israelachvili. *Intermolecular and Surface Forces*. Elsevier (2nd edition), 1991.

[39] J. Cahn. Phase separation by spinodal decomposition in isotropic systems. *J. Chem. Phys.*, 42:93, 1965.

[40] G. Reiter. Dewetting of thin polymer films. *Phys. Rev. Lett.*, 68(1):75–79, 1992.

[41] R. Seemann, S. Herminghaus, and K. Jacobs. Dewetting patterns and molecular forces: A reconciliation. *Phys. Rev. Lett.*, 86 (24):5534–5537, 2001.

[42] C. Bolline, S. Cuenot, B. Nystem, and A. M. Jonas. Spinodal-like dewetting of thermodynamically-stable thin polymer films. *Eur. Phys. J. E.*, 12:389, 2003.

[43] R. Seemann, S. Herminghaus, C. Neto, S. Schlagowski, D. Podzimek, R. Konrad, H. Mantz, and K. Jacobs. Dynamics and structure formation in thin polymer films. *J. Phys. Condens Matter.*, 17:S267, 2005.

[44] J. W. Swan. Stress and other effects produced in resin and in a viscid compound of resin and oil by electrification. *Proc. R. Soc. (London)*, 62:38–46, 1897.

[45] L. Tonks. A theory of liquid surface rupture by a uniform electric field. *Phys. Rev.*, 48:562–568, 1935.

[46] J. R. Melcher. Electrohydrodynamic and magnetohydrodynamic surface waves and instabilities. *Phys. Fluids*, 4:1348–1354, 1961.

[47] J. R. Melcher and C. V. Smith. Electrohydrodynamic charge relaxation and interfacial perpendicular-field instability. *Phys. Fluids*, 8:1193, 1969.

[48] E. Schaeffer, T. Thurn-Albrecht, T. P. Russell, and U. Steiner. Electrically induced structure formation and pattern transfer. *Nature*, 403:874–877, 2000.

[49] S. Chou and L. Zhuang. Lithographically induced self-assembly of periodic polymer micropillar arrays. *J. Vac. Technol. B*, 17:3197–3202, 1999.

[50] S. Chou, L. Zhuang, and L Guo. Lithographically induced self-construction of polymer microstructures for resistless patterning. *Appl. Phys. Lett.*, 75:1004–1006, 1999.

[51] Z. Lin, T. Kerle, T.P. Russell, E. Schäffer, and U. Steiner. Structure formation at the liquid/liquid bilayer in electric fields. *Macromolecules*, 35:3971–3976, 2002.

[52] M. D. Morariu, N. E. Voicu, E. Schäffer, Z. Lin, T. P. Russell, and U. Steiner. Hierarchical structure formation and pattern replication induced by an electric field. *Nature Materials*, 2:48–52, 2003.

[53] III L. F. Pease and W. B. Russel. Electrostatically induced submicron patterning of thin perfect and leaky dielectric films: A generalized linear stability analysis. *J. Chem. Phys.*, 118 (8):3790–3803, 2003.

[54] N. Wu, Pease L. F., and W. B. Russel. Electric-field-induced patterns in thin polymer films: weakly nonlinear and fully nonlinear evolution. *Langmuir*, 21:12290–12302, 2005.

[55] R. Verma, A. Sharma, K. Kargupta, and J. Bhaumik. Electric field induced instability and pattern formation in thin liquid films. *Langmuir*, 21:3710–3721, 2005.

[56] N. E. Voicu, S. Harkema, and U. Steiner. Electric-field-induced pattern morphologies in thin liquid films. *Advanced Functional Materials*, 16:926–934, 2006.

[57] E. Schaffer, T. Thurn-Albrecht, T. P. Russell, and U. Steiner. Electrohydrodynamic instabilities in polymer films. *Europhys. Lett.*, 53 (4):518–524, 2001.

[58] L. D. Landau and E. M. Lifshitz. *Electrodynamics of continuous media.* Pergamon Press, 1984.

[59] Prof. Sinclair. Lecture notes on electron-matter interactions. Technical report, Materials Science & Engineering department, Stanford University, USA, 2000.

[60] G. Binnig, C. F. Quate, and C. Gerber. Atomic force microscope. *Phys. Rev. Lett.*, 56(9):930–933, 1986.

[61] C. Neinhuis and W. Barthlott. Purity of the sacred lotus, or escape from contamination in biological surfaces. *Planta*, 202:1–8, 1997.

[62] N. Takeshita, L. A. Paradis, D. Oner, T. J. McCarthy, and W. Chen. Simultaneous tailoring of surface topography and chemical structure for controlled wettability. *Langmuir*, 20 (19):8131, 2004.

[63] C. W. Extrand. Model for contact angles and hysteresis on rough and ultraphobic surfaces. *Langmuir*, 18 (21):7991, 2002.

[64] R. N. Wenzel. Resistance of solid surfaces to wetting by water. *Ind. Eng. Chem.*, 28:988, 1936.

[65] A. B. D. Cassie and S. Baxter. Wettability of porous surfaces. *Trans. Faraday Soc.*, 3:16, 1944.

[66] R. Parthasarathy and J. T. Groves. Optical techniques for imaging membrane topography. *Cell Biochemistry and Biophysics*, 41:391–414, 2004.

[67] R. Kohler, P. Lazar, and H. Riegler. Optical imaging of thin films with molecular depth resolution. *App. Phys. Lett.*, 89:241906, 2006.

[68] I. H. Malitson. Interspecimen comparison of the refractive index of fused silica. *J. Opt. Soc. Am.*, 55 (10):1205–1209, 1965.

[69] S. Adachi. Model dielectric constants of si and ge. *Phys. Rev. B*, 38 (18):12966–12976, 1988.

[70] S. Laux, N. Kaiser, A. Zoller, R. Gotzelmann, H. Lauth, and H. Bernitzki. Room-temperature deposition of indium tin oxide thin films with plasma ion-assisted evaporation. *Thin Solid Films*, 335:1–5, 1998.

[71] *Index of refraction, Duke Scientific, Technical Note 007B (1996).*

[72] X. Hu, K. Shin, M. Rafailovich, J. Sokolov, R. Stein, Y. Chan, K. Williams, W. L. Wu, and R. Kolb. Anomalies in the optical index of refraction of spun cast polystyrene thin films. *High Performance Polymers*, 12 (4):621–629, 2000.

[73] S. Jang, B. S. Kang, F. Ren, N. W. Emanetoglu, H. Shen, W. H. Chang, B. P. Gila, M. Hlad, and S. J. Pearton. Comparison of e beam and sputter deposited ito films for 1.55 micron metal semiconductor metal photodetector applications. *Journal of The Electrochemical Society*, 154 (5):H336 – H339, 2007.

[74] M. Bender, W. Seelig, C. Daube, H. Frankenberger, B. Ocker, and J. Stollenwerk. Dependence of oxygen flow on optical and electrical properties of dc-magnetron sputtered ito films. *Thin Solid Films*, 326 (1-2):72–77, 1998.

[75] P. Winsemius, F. F. van Kampen, H. P. Lengkeek, and C. G. van Went. Temperature dependence of the optical properties of au, ag and cu. *Journal of Physics F: Metal Physics*, 6 (8):1583–606, 1976.

[76] *SU-8 2000 Datasheet, Microchem.*

[77] R. Sherman, D. Hirt, and R. J. Vane. Surface cleaning with the carbon dioxide snow jet. *J. Vac. Sci. Technol.*, 12:1876, 1994.

[78] D. Parker, J. Bussink, H. T. van de Grampe, G. W. Wheatley, E-U. Dorf, E. Ostlinning, and K. Reinking. *High-Temperature Polymers.* Ullmann's Encyclopedia of Industrial Chemistry, 2002.

[79] H. R. Shanks, P. D. Maycock, P. H. Sidles, and G. C. Danielson. Thermal conductivity of silicon from 300 to 1400k. *Phys. Rev.*, 130 (5):1743–1748, 1963.

[80] C. J. Glassbrenner and G. A. Slack. Thermal conductivity of silicon and germanium from 3k to the melting point. *Phys. Rev.*, 134 (4A):A1058–1069, 1964.

[81] E. A. Algaer, M. Alaghemandi, M. C. Bohm, and F. Muller-Plathe. Thermal conductivity of amorphous polystyrene in supercritical carbon dioxide studied by reverse nonequilibrium molecular dynamics simulations. *J. Chem . Phys.*, In print, 2009.

[82] A. D. Pasquino and M. N. Pilswort. The thermal conductivity of polystyrene, oriented and unoriented, with measurements of the glass-transition temperature. *J. Polym. Sci., Part B: Polym. Lett.*, 2:253–255, 1964.

[83] D. R. Barbero and U. Steiner. Non-equilibrium polymer rheology in spin-cast films. *Physical Review Letters*, 102 (24):248303, 2009.

[84] R. L. Jones, S. K. Kumar, D. L. Ho, R. M. Briber, and T. P. Russell. Chain conformation in ultrathin polymer films. *Nature*, 400:146–149, 1999.

[85] L. Lurio, H. Kim, A. Ruhm, J. Basu, J. Lal, S. Sinha, and S. Mochrie. Surface tension and surface roughness of supported polystyrene films. *Macromolecules*, 36:5704–5709, 2003.

[86] R. Xie, A. Karim, J. F. Douglas, C. C. Han, and R. A. Weiss. Spinodal dewetting of thin polymer films. *Phys. Rev. Lett.*, 81 (6):1251–1254, 1998.

[87] E. Schaffer, T. Thurn-Albrecht, T. P. Russell, and U. Steiner. Electrohydrodynamic instabilities in polymer films. *Europhys. Lett.*, 53:518–524, 2001.

[88] L-H Lee. Correlation between lewis acid-base surface interaction components and linear solvation energy relationship solvatochromic alpha and beta parameters. *Langmuir*, 12:1681–1687, 1996.

[89] J. H. Park and E. Kim. Effect of electric-field-assisted thermal annealing of poly(4-vinylphenol) film on its dielectric constant. *App. Phys. Lett.*, 92:103311, 2008.

[90] M. Wulf, S. Michel, K. Grundke, O. I. del Rio, D. Y. Kwok, and A. W. Neumann. Simultaneous determination of surface tension and density of polymer melts using axisymmetric drop shape analysis. *J. Coll. & Int. Sci.*, 210:172–181, 1999.

[91] E. Buck and al. *Macrom.*, 37:8647, 2004.

[92] J. H. Teichroeb and J. A. Forrest. Direct imaging of nanoparticle embedding to probe viscoelasticity of polymersurfaces. *Phys. Rev. Lett.*, 91(1):016104, 2003.

[93] T. Kerle, Z. Lin, H.-C. Kim, and T. P. Russell. Mobility of polymers at the air/polymer interface. *Macromolecules*, 34(10):3484–3492, 2001.

[94] H. Kim, A. Ruhm, L. B. Lurio, J. K. Basu, J. Lal, D. Lumma, S.G. J. Mochrie, and S. K. Sinha. Surface dynamics of polymer films. *Phys. Rev. Lett.*, 90(6):068302, 2003.

[95] H. Bodiguel and C. Fretigny. Viscoelastic dewetting of a polymer film on a liquid substrate. *Eur. Phys. J. E*, 19:185–193, 2006.

[96] M. E. Mackay, Dao T. T., Tuteja A., Ho D. L., Van Horn B., Kim H. C., and Hawker C. J. Nanoscale effects leading to non-einstein-like decrease in viscosity. *Nature Materials*, 2:762–766, 2003.

[97] T. G. Fox and P. J. Flory. Second-order transition temperatures and related properties of polystyrene. 1. influence of molecular weight. *J. Appl. Phys.*, 21:581–591, 1950.

[98] T. G. Fox and P. J. Flory. Second-order transition temperatures and related properties of polystyrene. 1. influence of molecular weight. *J. Polym. Sci.*, 14 (75):315–319, 1954.

[99] S. G. Croll. The origin of residual internal stress in solvent-cast thermoplastic coatings. *J. Appl. Polym Sci.*, 23:847–858, 1979.

[100] H. Kim, A. Ruhm, L. B. Lurio, J. K. Basu, J. Lal, S. G. J. Mochrie, and S. K. Sinha. Synchrotron radiation studies of the dynamics of polymer films. *J. Phys.: Condens. Matter*, 16:S3491–S3497, 2004.

[101] M. Doi and S. F. Edwards. *The Theory of Polymer Dynamics*. Oxford University Press, 1986.

[102] T. Kanaya. Annealing effects on thickness of polystyrene thin films as studied by neutronreflectivity. *Polymer*, 44:3769–3773, 2003.

[103] C. G. Robertson, S. Warren, D. J. Plazek, and C. M. Roland. Reentanglement kinetics in sheared polybutadiene solutions. *Macromolecules*, 37 (26):10018–10022, 2004.

[104] *Mackay, M. E. , private communication.*

[105] S. R. Quake. Topological effects of knots in polymers. *Phys. Rev. Lett.*, 73:3317–3320, 1994.

[106] P. Damman, S. Gabriele, S. Coppee, S. Desprez, D. Villers, T. Vilmin, E. Raphael, M. Hamieh, S.Al Akhrass, and G. Reiter. Relaxation of residual stress and reentanglement of polymers in spin-coatedfilms. *Phys. Rev. Lett.*, 99:036101, 2007.

[107] T. Vilmin and E. Raphael. Dynamic instability of thin viscoelastic films under lateral stress. *Phys. Rev. Lett.*, 97:036105, 2006.

[108] D. R. Barbero, P. Andrew, and U. Steiner. A sensitive interferometric method to study the growth of thin film surface instabilities. *in preparation*, 2009.

[109] S. Tolansky. *An introduction to interferometry*. John Wiley, 1962.

[110] J. G. Gottling and W. S. Nicol. Double-layer interference in air-cds films. *J. Opt. Soc. Am.*, 56 (9):1227–1231, 1966.

[111] M. Born and E. Wolf. *Principles of optics*. Cambridge University Press, 1999.

[112] K. A. Leach, Y. Lin, and T. P. Russell. Early stages in the growth of electric field-induced surface fluctuations. *Macromolecules*, 38:4868–4873, 2005.

[113] D. R. Barbero, P. Hoffmann, and H. J. Mathieu. Moules en fluoropolymère pour micro et nano-structuration. *Le Dialogue Innovation*, 139:1 (Front cover), 2005.

[114] C. J. Clemente, J-H. Dirks, D. R. Barbero, U. Steiner, and W. Federle. Friction ridges in cockroach climbing pads: anisotropy of shear stress measured on transparent, microstructured substrates. *J. Comp. Physiol. A*, 195 (9):805, 2009.

[115] B. Wenger, D. R. Barbero, N. Tétreault, M. E. Welland, U. Steiner, and R. H. Friend. Mechanically tunable conjugated polymer distributed feedback lasers. *in final form (to be submitted)*, 2009.

[116] S. Y. Chou, P. R. Krauss, and P. J. Renstrom. Imprint of sub-25 nm vias and trenches in polymers. *Appl. Phys. Lett.*, 67:3114, 1995.

[117] M. Li, L. Chen, W. Zhang, and S. Y. Chou. Pattern transfer fidelity of nanoimprint lithography on six-inch wafers. *Nanotechnology*, 14:33–36, 2003.

[118] J. Seekamp, S. Zankovych, A. H. Helfer, P. Maury, C. M. Sotomayor Torres, G. Bottger, C. Liguda, B. Eich, B. Heidar, L. Montelius, and L. Ahopelto. Nanoimprinted passive optical devices. *Nanotechnology*, 13:581–586, 2002.

[119] S. D. Moon, N. S. Lee, and S. I. Kang. Fabrication of a microlens array using micro-compression molding with an electroformed mold insert. *J. Micromech. Microeng.*, 13:98–103, 2003.

[120] P. R. Krauss and S. Y. Chou. Nano-compact disks with 400 gbit/in2 storage density fabricated using nanoimprint lithography and read with proximal probe. *Appl. Phys. Lett.*, 71:3174–3176, 1997.

[121] Z. Yu, S. J. Schablitsky, and S. Y. Chou. Nanoscale gaas metal-semiconductor-metal photodetectors fabricated using nanoimprint lithography. *Appl. Phys. Lett.*, 74(16):2381–2383, 1999.

[122] H. Becker and C. Gartner. Polymer microfabrication methods for microfluidic analytical applications. *Electrophoresis*, 21:12–26, 2000.

[123] C. F. Chou L. J. Guo, X. Cheng. *Nano Lett.*, 4 (1), 2004.

[124] S. Y. Chou, P. R. Krauss, W. Zhang, L. Guo, and L. Zhuang. Sub-10 nm imprint lithography and applications. *J. Vac. Sci. Technol. B*, 15(6):2897–2904, 1997.

[125] L. J. Guo. *J. Phys. D*, 37:R123, 2004.

[126] M. Komuro, Y. Tokano, J. Taniguchi, T. Kawasaki, I. Miyamoto, and H. Hiroshima. Improvement of imprinted pattern uniformity using sapphire mold. *Jpn. J. Appl. Phys. Part 1*, 41 (6B):4182–4185, 2002.

[127] R. W. Jaszewski, H. Schift, B. Schnyder, A. Schneuwly, and P. Gröning. The deposition of anti-adhesive ultra-thin teflon-like films and their interaction with polymers during hot embossing. *Appl. Surf. Sci.*, 143:301–308, 1999.

[128] E. Riaplov, D. R. Barbero, L. Barbieri, P. Hoffmann, and H. J. Mathieu. Xps study of hot-embossed polymers. In *Surface Science Conf., Freiburg, Switzerland*, 2004.

[129] D. R. Barbero, P. Hoffmann, and H. J. Mathieu. Easy release fluoropolymer molds for micro- and nano-pattern replication. *European Patent*, 2006.

[130] X.-M. Zhao, Y. Xia, and G. M. Whitesides. Soft lithographic methods for nano-fabrication. *J. Mater. Chem.*, 7(7):1069–1074, 1997.

[131] Y. S. Kim, K. Y. Suh, and H. H. Lee. Fabrication of three-dimensional microstructures by soft molding. *Appl. Phys. Lett.*, 79 (14):2285–2287, 2001.

[132] J. Narasimhan and I. Papautsky. Polymer embossing tools for rapid prototyping of plastic microfluidic devices. *J. Micromech. Microeng.*, 14:96–103, 2004.

[133] H. Ge, W. Wu, Z. Li, G. Y. Jung, D. Olynick, Y. Chen, J. Alexander Liddle, S. Y. Wang, and R. S. Williams. *Nano Lett.*, 5(1):179, 2005.

[134] E. Delamarche, H. Schmid, B. Michel, and H. Biebuyck. Stability of molded polydimethylsiloxane microstructures. *Adv. Mater.*, 9:741–746, 1997.

[135] Y. S. Kim, N. Y. Lee, J. R. Lim, M. J. Lee, and S. Park. Nanofeature-patterned polymer mold fabrication toward precisely defined nanostructure replication. *Chem. Mater.*, 17:5867, 2005.

[136] D.-G. Choi, J.-H. Jeong, Y.-S. Sim, E.-S. Lee, W.-S. Kim, and B.-S. Bae. Fluorinated organic-inorganic hybrid mold as a new stamp for nanoimprint and soft lithography. *Langmuir*, 21:9390–9392, 2005.

[137] J. P. Rolland, E. C. Hagberg, G. M. Denison, K. R. Carter, and J. M. De Simone. High-resolution soft lithography: Enabling materials for nanotechnologies. *Angew. Chem. Int. Ed.*, 43(43):5796 – 5799, 2004.

[138] D.-Y. Khang and H. H. Lee. Sub-100 nm patterning with an amorphous fluoropolymer mold. *Langmuir*, 20:2445–2448, 2004.

[139] D.-Y. Khang, H. Kang, T.-I. Kim, and H. H. Lee. Low-pressure nanoimprint lithography. *Nano Lett.*, 4(4):633–637, 2004.

[140] A. Bietsch and B. Michel. *J. Appl. Phys.*, 88:4310, 2000.

[141] H. Schmid and B. Michel. *Macromolecules*, 33:3042, 2000.

[142] T. W. Odom, J. C. Love, D. B. Wolfe, K. E. Paul, and G. M. Whitesides. *Langmuir*, 18:5314, 2002.

[143] D. Trimbach, K. Feldman, N. D. Spencer, D. J. Broer, and C. W. M. Bastiaansen. *Langmuir*, 19:10957, 2003.

[144] Y. H. Yan, K. Feldman, M. B. Chan-Park, and C. Y. Yue. *Langmuir*, 21:8905, 2005.

[145] H. D. Rowland, A. C. Sun, P. R. Schunk, and W. P. King. *J. Micromech. Microeng.*, 15:2414, 2005.

[146] B. Michel, A. Bernard, A. Bietsch, E. Delamarche, M. Geissler, D. Juncker, H. Kind, J.-P. Renault, H. Rothuizen, H. Schmid, P. Schmidt-Winkel, R. Stutz, and H. Wolf. *IBM J. Res. Dev.*, 45:697, 2001.

[147] *Properties Handbook for DuPont Tefzel® ETFE, DuPont; Information sheet for properties of PTFE Lubriflon, Angst & Pfister.*

[148] K. Gjerde, J. K. Hansen, C.H. Clausen, K.B.K. Teo, and P. Bøggild. Carbon nanotube forests: a non-stick workbench for nanomanipulation. *Nanotechnology*, 17:4917–4922, 2006.

[149] A. Berman and J. Israelachvili. *Control and minimization of friction via surface modification*. Dordrecht; Boston: Kluwer Academic Publishers, 1997.

[150] W.Q. Ding. Micro/nano-particle manipulation and adhesion studies. *J. Adhes. Sci. Tech.*, 22 (5-6):457–480, 2008.

[151] Y. Peng, T. Cullis, and B. Inkson. Bottom-up nanoconstruction by the welding of individual metallic nanoobjects using nanoscale solder. *Nano Lett.*, 9 (1):91–96, 2009.

[152] W.R. Hansen and K. Autumn. Evidence for self-cleaning in gecko setae. *Proc. Natl. Acad. Sci.*, 102:385–389, 2005.

[153] J. Barnes, W. Federle, and P. Drechsler. Adhesion and friction forces generated by single toe pads of the tree frog litoria carerulea. *Comp. Biochem. Physiol. A*, 143:S94–S95, 2006.

[154] V.V. Dobrokhotov, M.M. Yazdanpanah, S. Pabba, A. Safir, and R.W. Cohn. Visual force sensing with flexible nanowire buckling springs. *Nanotechnology*, 19:035502, 2008.

[155] C.J. Clemente and W. Federle. Pushing versus pulling: division of labour between tarsal attachment pads in cockroaches. *Proc. R. Soc. B*, 275:1329–1336, 2008.